

# Hybrid Perovskites: Effective Crystal Growth for Optoelectronic Applications

Taewoo Jeon, Sung Jin Kim, Jisun Yoon, Jinwoo Byun, Hye Rim Hong, Tae-Woo Lee, Ji-Seon Kim, Byung-ha Shin, and Sang Ouk Kim\*

Outstanding material properties of organic-inorganic hybrid perovskites have triggered a new insight into the next-generation solar cells. Beyond solar cells, a wide range of controllable properties of hybrid perovskites, particularly depending on crystal growth conditions, enables versatile high-performance optoelectronic devices such as light-emitting diodes, photodetectors, and lasers. This article highlights recent progress in the crystallization strategies of organic-inorganic hybrid perovskites for use as effective light harvesters or light emitters. Fundamental background on perovskite crystalline structures and relevant optoelectronic properties such as optical band-gap, electron-hole behavior, and energy band alignment are given. A detailed overview of the effective crystallization methods for perovskites, including thermal treatment, additives, solvent mediator, laser irradiation, nanostructure, and crystal dimensionality is reported offering a comprehensive correlation among perovskite processing conditions, crystalline morphology, and relevant device performance. Finally, future research directions to overcome current practical bottlenecks and move towards reliable high performance perovskite optoelectronic applications are proposed.

## 1. Introduction

Organic-inorganic hybrid halide perovskites are now innovating in conventional optoelectronics research with the unprecedented collective advantages of wide tunability of the band gap from the near infrared to violet regime, low trap density, excellent charge carrier diffusion/transport, low temperature

solution processing, and so on.<sup>[1–6]</sup> Notably, incredible success of the perovskite solar cells in the past few years has triggered many research activities on the perovskite material synthesis, optoelectronic properties, crystallization methods, and device architectures.<sup>[7–12]</sup> Beyond applications in solar cells and more recently, hybrid perovskite materials are also showing great potential for light-emitting diodes (LEDs) and lasers.<sup>[13–18]</sup> Perovskite materials have a history longer than 170 years since their discovery. Although the first perovskite LED (PeLED) and solar cell were reported in the years of 1992 and 2009, both devices were out of practical consideration mainly due to the poor material stability under atmospheric conditions and the use of a liquid electrolyte.<sup>[19,20]</sup> Meanwhile, the first report of solid-state perovskite solar cells by Kim et al. in 2012, which dramatically improved the device stability and performance with the use of solid state transport materials, triggered enormous research effort worldwide.<sup>[21]</sup> Since then, hybrid perovskite materials have been gaining huge interest as promising optoelectronic materials.

Optoelectronic devices operate in different ways depending on whether they serve as a light harvester or a light emitter. The light harvesting devices such as solar cells and photodetectors convert incident photons into free charge carriers, whereas the light-emitting devices such as LEDs and lasers turn injected charge carriers into photons in heterojunction structures.<sup>[22,23]</sup>

For perovskite solar cells, power conversion efficiency (PCE) over 22% has already been attained by the development of materials, crystallization processes, and device architectures based on 3D perovskites. Now, it is well-recognized that a perovskite light harvester should have: i) a high absorption coefficient over a wide spectrum range, ii) a low exciton binding energy ( $E_b$ ) for efficient exciton dissociation, iii) a long charge carrier diffusion length and high mobility for efficient charge transport/collection, and iv) a low trap state to prevent charge carrier recombination.<sup>[24,25]</sup> In contrast to the striking device efficiency of perovskite solar cells, perovskite LEDs (PeLEDs) have suffered from device performance that is much poorer than conventional organic LEDs and quantum dot LEDs despite their excellent color purity, bright luminescence, and wide chromatic tunability.<sup>[23]</sup> Initial PeLED research adopting materials and processes used in solar cells showed poor external quantum efficiency (EQE) of <0.1%,

Dr. T. Jeon, S. J. Kim, Dr. J. Yoon, J. Byun, H. R. Hong, Prof. S. O. Kim  
National Creative Research Initiative Center  
for Multi-Dimensional Directed Nanoscale Assembly  
Department of Materials Science and Engineering  
KAIST

Daejeon 34141, Republic of Korea  
E-mail: sangouk.kim@kaist.ac.kr

Prof. T.-W. Lee  
Department of Materials Science and Engineering  
Seoul National University  
Gwanak-gu, Seoul 08826, Republic of Korea

Prof. J.-S. Kim  
Department of Physics and Centre for Plastic Electronics  
Imperial College London  
South Kensington Campus, London SW7 2AZ, UK

Prof. B. Shin  
Department of Materials Science and Engineering  
KAIST  
Daejeon 34141, Republic of Korea

DOI: 10.1002/aenm.201602596

while recent EQE of visible PeLEDs exceeds 10% by employing a new film formation process, new device architecture, and materials that avoid exciton quenching at the interface as well as in the bulk film.<sup>[26–28]</sup> This verifies that LEDs require material properties entirely different from solar cells. It is desirable for the perovskite materials for LEDs to have i) balanced charge transport property, ii) high  $E_b$  and short exciton diffusion length ( $L_d$ ) for efficient radiative recombination, and iii) low trap state to prevent charge trapping and non-radiative recombination. Taken together, solar cells and LEDs require different optoelectronic properties, which can be achieved by the manipulation of perovskite film structures, including crystal grain size, crystal dimension, film surface coverage, and morphology. From this perspective, comprehension of the correlation between crystallization, material properties, and relevant device performance is essential. Common and different requirements of perovskite materials for the applications as well as strategies for a light harvester and emitter are compared in Table 1.

To date, a number of crystallization strategies have been introduced for high-performance perovskite solar cells and PeLEDs.<sup>[29–31]</sup> Thermal treatment is the most widely used method to convert solution-processed precursor films into a perovskite crystalline phase while different processing parameters lead to the modification of surface coverages, crystal grain sizes, and relevant material properties. Here, fine control of the crystalline nucleation and growth via additives, vapor treatment, solvent annealing, and intermediate phase mediator is required to obtain high crystalline perovskite films. In general, full surface coverage and low defect states are desired for both solar cells and LEDs to minimize leakage current and non-radiative recombination. By contrast, grain size and nanostructured crystals involving variation of material properties, such as  $E_b$  and  $L_d$ , have to be judiciously controlled for each application. More specifically, light-harvesting devices prefer a low  $E_b$  and long  $L_d$ , whereas a high  $E_b$  and short  $L_d$  are possibly favored for LEDs.<sup>[4,14,23,24]</sup> Furthermore, the dimensionality of perovskite crystals becomes more and more significant due to its direct impact on  $E_b$ .<sup>[32–34]</sup> Overall, all these approaches are able to produce a wide variety of hybrid perovskite films and extend the potential of perovskite optoelectronic devices (Scheme 1).

Here we highlight recent progress in hybrid perovskite optoelectronics, particularly solar cells and LEDs. We focus on effective perovskite crystallization methods to secure the requisite optoelectronic properties, while considering the different working mechanisms between solar cells and LEDs. Optimal performance of perovskite optoelectronic devices requires an appropriate choice of materials and careful management of their crystallization behavior. The correlation among the material composition, crystallization method, morphology, and photophysical properties is reviewed. In the first part of this article, we offer the fundamental background for perovskite optoelectronic properties, including perovskite crystalline structures, electron–hole pair behavior, and energy band alignment for device configuration. Thereafter, a variety of crystallization methods, relevant material properties, and device performances are correlated for solar cells and LEDs, respectively. Extensive lists comparing  $E_b$  and device performance of solar cells/PeLEDs are summarized in –the tables. In the conclusion and outlook section, remaining technological bottlenecks are summarized with our suggestions for



**Taewoo Jeon** has worked as a postdoctoral fellow with Prof. Sang Ouk Kim since 2013. He received his Ph.D. degree from the Department of Physics, École Polytechnique, Palaiseau, France in 2013 under the supervision of Prof. Yvan Bonnassieux. His research interests include optoelectronics based on organic–inorganic materials and organic–inorganic hybrid perovskite materials.



**Sung Jin Kim** is a Ph.D. candidate in the Department of Materials Science and Engineering at KAIST under the supervision of Prof. Sang Ouk Kim. He is also a chief search engineer from LG Display Co., Ltd. His current research interest is device structure engineering in the field of light-emitting diode applications.



**Sang Ouk Kim** is the chaired professor in the Department of Materials Science and Engineering at KAIST and the director of the National Creative Research Initiative Center for Multi-Dimensional Directed Nanoscale Assembly, Daejeon, Korea. He received his Ph.D. from the Department of Chemical Engineering, KAIST in 2000 and carried out postdoctoral research in the Department of Chemical and Biological Engineering, University of Wisconsin-Madison. He has a broad research interest in the directed molecular assembly of soft nanomaterials, which includes block copolymer self-assembly; graphene-based materials assembly and chemical modification; and flexible and wearable energy devices.

future research directions emphasizing the significance of nanostructure formation and reliable large-area device processing.

## 2. Fundamental Background

### 2.1. Perovskite Structures

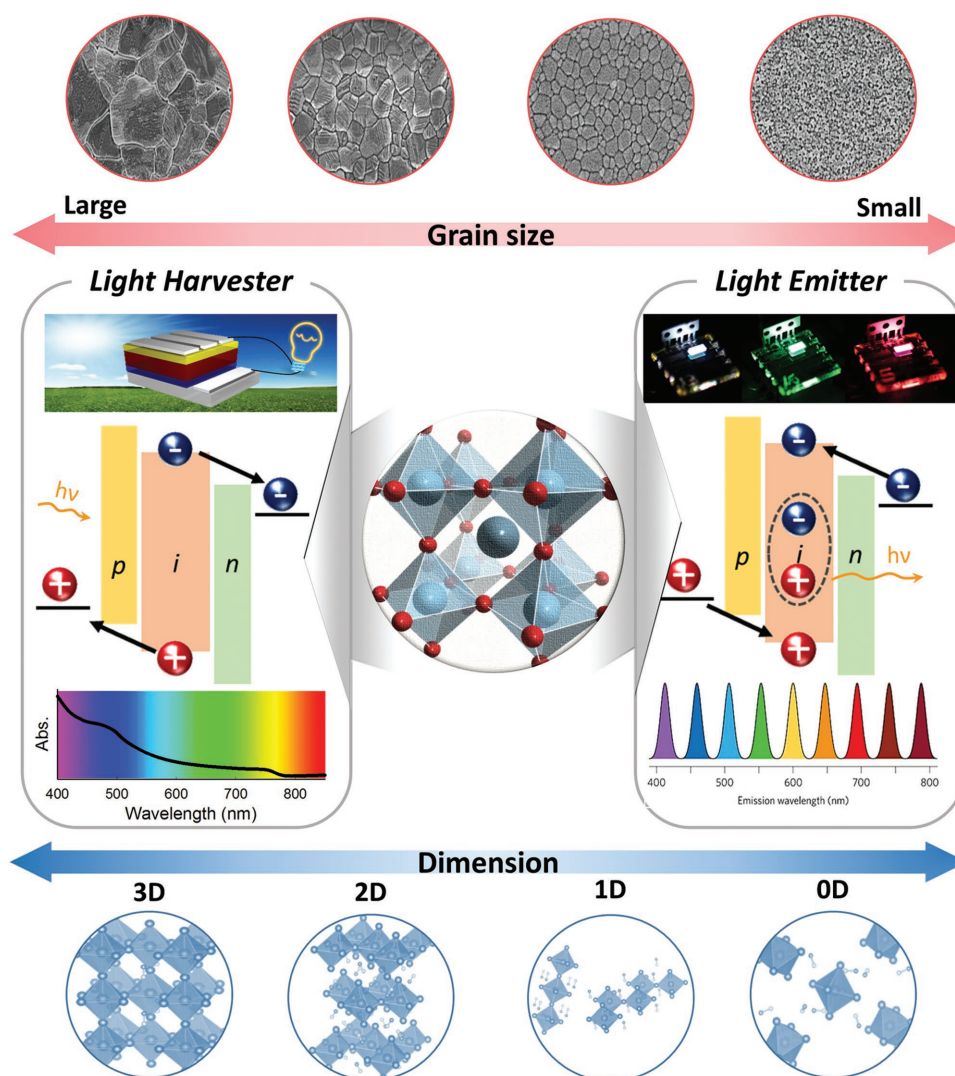
Perovskite is a general term to designate a family of materials with the common crystal structure of the mineral  $\text{CaTiO}_3$ . The

**Table 1.** Summary of common and different requirements for perovskite light harvesters and light emitters, and strategies for each application.

	Light harvester	Light Emitter
<b>Common Requirements</b>	<ul style="list-style-type: none"> <li>• Low density of trap-states</li> <li>• Balanced charge carriers transport</li> <li>• Formation of homogeneous and dense thin-film</li> <li>• Energy level alignment with transport materials</li> </ul>	
<b>Different Requirements</b>	<ul style="list-style-type: none"> <li>• Small exciton binding energy</li> <li>• Long charge carrier diffusion length</li> <li>• High absorption coefficient</li> </ul>	<ul style="list-style-type: none"> <li>• Large exciton binding energy</li> <li>• Short exciton diffusion length</li> <li>• Efficient radiative decay</li> </ul>
<b>Strategies</b>	<ul style="list-style-type: none"> <li>• Heat management</li> <li>• Delayed crystallization (additive, solvent, etc.)</li> <li>• Vapor annealing</li> <li>• Laser crystallization</li> </ul>	<ul style="list-style-type: none"> <li>• Thin-film engineering (ultrathin emission layer, polymer matrix)</li> <li>• Rapid crystallization</li> <li>• Nanostructuring</li> <li>• Low dimensional perovskites</li> </ul>

structure of recently emerging hybrid perovskites can also be described by a similar chemical formula  $ABX_3$ , where A is a small organic molecule occupying a corner of a unit cell with

12-fold coordination, B is a divalent transition metal in general sitting in a body-centered position with 6-fold coordination, and X is a halogen with face-centered positioning (**Figure 1**). The



**Scheme 1.** Schematic description of representative optoelectronic applications of hybrid perovskites WITH guide arrows for grain size and dimension control for target applications. Inset images for light emitter are reproduced with permission.<sup>[47,211]</sup> Copyright 2016, Nature Publishing Group. Crystal structures of perovskite are reproduced with permission.<sup>[212]</sup> Copyright 2015, American Chemical Society.



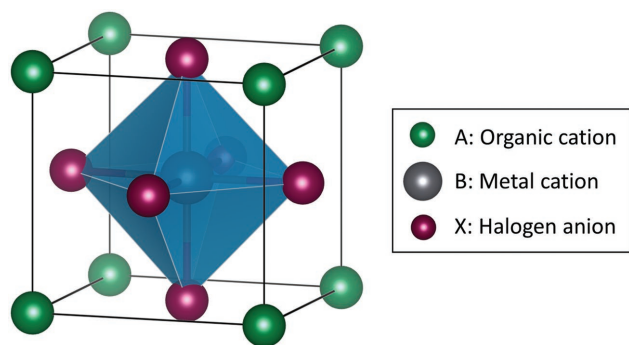


**Figure 1.** Unit cell structure of organic–inorganic hybrid perovskite  $ABX_3$  crystal.

perovskite crystal structure is very flexible in terms of composition, provided that the Goldschmidt's values of tolerance factor ( $t$ ) and the octahedral factor ( $\mu$ ) are within the known range. The  $t$  indicates the state of distortion and stability of perovskite crystal structures based on ionic radii ( $r$ ) of atoms at A, B, and X positions by  $t = (r_A + r_X)/\sqrt{2}(r_B + r_X)$ . The  $\mu$  is defined as the ratio  $r_B/r_X$ , which is directly correlated to formation of the  $BX_6$  octahedron.<sup>[25]</sup> Both parameters are used to predict the formability of the perovskite structure.<sup>[35]</sup> Typically, hybrid halide perovskites present  $0.81 < t < 1.11$  and  $0.44 < \mu < 0.90$ . Specifically,  $t$  ranging from 0.9 to 1.0 corresponds to a cubic structure of the perovskite and  $t$  in the range of 0.71–0.90 corresponds to a tetragonal or orthorhombic structure.<sup>[2]</sup> Given this range of  $t$ , the ionic radius of organic cation should be limited to 2.9 Å, considering the ionic radii of commonly used Pb (1.2 Å) and I (2.2 Å) in hybrid perovskite. This means that organic molecules with fewer than two or three C–C and C–N bonds can sustain 3D perovskite structures.<sup>[23]</sup> Otherwise, low-dimensional perovskites, indicating specific cuts or slices of the 3D perovskite, are obtained.<sup>[36]</sup>

Various material characteristics, including ferroelectricity, piezoelectricity, superconductivity, and magnetoresistance, are manifested depending on the types of elements in the perovskites. In principle, coupling of B–X is strongly covalent and it mainly contributes to the determination of dielectric, electrical, and electronic properties such as band structure. The valence band maximum of a hybrid perovskite is composed of antibonding state between B-s and X-p orbitals, while the conduction band minimum is determined by a non-bonding state between B-p and X-p orbitals, which defines the fundamental electronic structure of hybrid perovskites.<sup>[25,37]</sup> Furthermore, A–X bonding has a minimal effect on B–X coupling due to its strong ionic bonding character. The size of the A ion does not directly affect the overall electronic structure of the perovskite but it influences crystal symmetry by the distortion of  $BX_6$  octahedra.

It is well-known that a temperature-dependent phase transition of a well-known hybrid perovskite,  $MAPbI_3$ , involves cubic, tetragonal, and orthorhombic phases.<sup>[37,38]</sup> As temperature increases, the transition from the orthorhombic to tetragonal phase, and to the cubic phase is observed with symmetry improvement. For instance,  $MAPbBr_3$  ( $MA = CH_3NH_3^+$ , methylammonium) perovskite, which is used light-emitting applications, has a cubic phase at temperatures over 237 K, whereas it has a tetragonal phase at 150–237 K, and an

orthorhombic phase under 144.5 K.<sup>[14]</sup>  $MAPbI_3$  perovskites used in light-absorbing applications<sup>[39,40]</sup> have tetragonal phase at room temperature and pseudo-cubic phase with octahedral tilting and cation rotation at in the temperature range from 300 K to 400 K.<sup>[38,41]</sup> In contrast, formamidinium ( $FA = CH(NH_2)_2^+$ ) halide based perovskites demonstrate promising thermal stability compared to conventional  $MAPbI_3$  perovskites.<sup>[42]</sup> Therefore, careful selection of the perovskite material is crucial for the stable operation of practical devices at desired temperature conditions.

## 2.2. Optoelectronic Properties of Perovskites

Management of light, such as emission, absorption, modulation, and transmission, is the core of optoelectronic applications and is principally governed by the quantum mechanical properties of optoelectronic materials. In other words, the electronic structures of materials, including the optical band-gap and density of states, the characteristics of the exciton and carrier lifetimes, and mobility, are significant elements for optoelectronic materials. Along these lines, organic–inorganic hybrid perovskites generally show excellent material properties, including high absorption coefficients, tunable band-gaps, and long carrier diffusion lengths. As mentioned, a wide tunability of the electronic structures of perovskites enables various optoelectronic devices such as solar cells, light-emitting diodes, photodetectors, and lasers. In the following subsections, the basic optoelectronic properties of hybrid perovskite are discussed.

### 2.2.1. Energy Band-Gap

The band-gap of an organic–inorganic hybrid perovskite is in the visible regime of the light spectrum (1.2–3.0 eV), in contrast to the typical oxide-based perovskites (3.0–5.0 eV).<sup>[24,43]</sup> The strongest point of a hybrid perovskite is the simple to tune electronic structure, which enables facile modification of the energy band-gap depending on the target applications. Energy band-gaps of the mostly widely used perovskite light harvesters such as  $MAPbI_3$  (1.55 eV) and  $CH(NH_2)_2PbI_3$  ( $FAPbI_3$ ) (1.43–1.48 eV) are close to the desirable optimal value of 1.4 eV, as suggested by the Shockley–Queisser efficiency limit. Perovskite absorbers with band-gaps around 1.45 eV are employed in the 22% perovskite solar cells, i.e., the record efficiency devices reported thus far.<sup>[44–46]</sup> In contrast, light-emitting perovskites show a wide range of color spectrum with high color purity over the visible regime along with various atomic compositions and the modification of  $BX_6$  octahedral bonding and crystal phases.<sup>[47,48]</sup>

In 2014, Eperon et al. explored the effects of methylammonium cation replacement (A site) with cesium or formamidinium cations (**Figure 2a**).<sup>[7]</sup> An organic cation at A site shows negligible electron orbital overlap with the  $BX_6$  octahedral phase and thus has minor effects on the major electronic properties of the hybrid perovskite. However, the energy band-gap of 3D perovskite is varied by the size effect of organic or inorganic cations due to the different degree of distortion within the limit of tolerance factor ( $t$ ). As  $r_A$  increases,  $t$  also increases

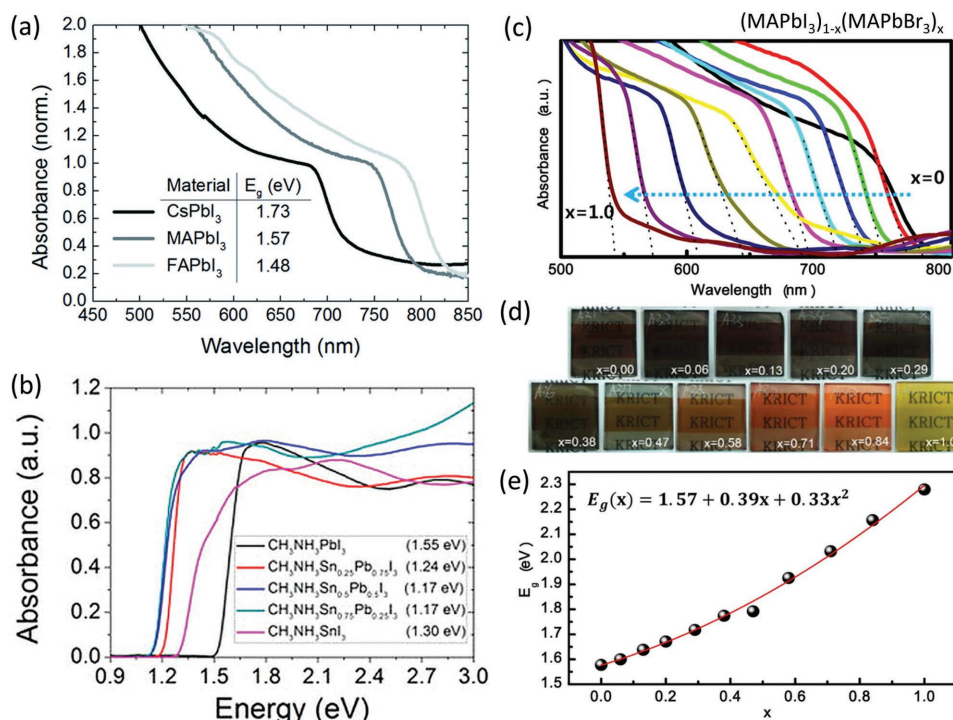


**Figure 2.** Absorbance of perovskite materials (ABX<sub>3</sub>) by changing ions positioning at A, B, and X site. Absorption spectra: a) with inorganic (Cs<sup>+</sup>) and organic cations (MA<sup>+</sup> and FA<sup>+</sup>) (A site). Reproduced with permission.<sup>[7]</sup> Copyright 2014, Royal Society of Chemistry, b) with Pb and Sn compositions (B site). Reproduced with permission.<sup>[51]</sup> Copyright 2014, American Chemical Society, c) with I and Br compositions (X site). d) Photograph of perovskite thin film and e) band-gap variation along with bromide contents. Panels (c–e) reproduced with permission.<sup>[3]</sup> Copyright 2013, American Chemical Society.

to have a high packing symmetry, resulting in a reduction of the band-gap and red-shift of the absorption edge. When the A cation is too large, a low-dimensional perovskite is formed, while if it is too small, lattice formation is disturbed due to a high lattice strain.<sup>[36]</sup>

A metal cation at the B site, typically a divalent oxidation state such as Pb<sup>2+</sup>, Sn<sup>2+</sup>, and Ge<sup>2+</sup>, is one of the fundamental elements that govern the principle electronic structures of perovskites. Currently Pb<sup>2+</sup> is dominant due to its superior optoelectronic properties and device performance but other metal elements are attracting increasing attention with the necessity of nontoxic lead-free and panchromatic perovskites.<sup>[49,50]</sup> Hao et al. investigated the band-gap of alloyed Pb- and Sn-based perovskites using compositional engineering (Figure 2b).<sup>[51]</sup> MASn<sub>1-x</sub>Pb<sub>x</sub>I<sub>3</sub> perovskite is easily synthesized by the stoichiometric mixing of two metals and shows an energy band-gap range of 1.17–1.55 eV; its absorption spectrum can be expanded up to 1060 nm in the near-infrared regime.<sup>[52–55]</sup> Interestingly, the energy band-gap does not lie between the two compositional extremes (1.35–1.55 eV), suggesting a substantial bowing parameter. It is well-recognized that the atomic orbital compositions of conduction and valence bands are associated with the anomalous band-gap variation trend. In terms of structure, both MAPbI<sub>3</sub> and MASnI<sub>3</sub> have tetragonal structure, but MAPbI<sub>3</sub> shows  $\beta$ -phase, whereas the highly symmetric  $\alpha$ -phase is observed for MASnI<sub>3</sub> at room temperature.<sup>[38]</sup>

The energy band-gap of a perovskite is also dramatically varied by the alteration of halide anions (I<sup>-</sup>, Br<sup>-</sup>, Cl<sup>-</sup>) at the X

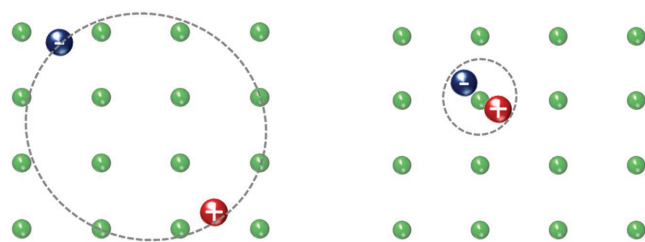
site. According to the MAPbX<sub>3</sub> composition, the band gap is widely controllable from 1.55 to 3.11 eV along with the halogen substitution direction from I to Cl, implying that absorption and emission spectra can be modulated over the entire visible range. The atomic size and electronegativity of halogen atom are responsible for the modification of the electronic structure. A high degree of crystal packing reduces the band-gap, as mentioned above. Additionally, a low electronegativity (Cl > Br > I) enhances covalent character of B–X bonding over the ionic character and induces a reduction in the energy band-gap. Chemical management of a mixed halide perovskite composed of I and Br was investigated by Noh et al. in 2013 (Figure 2c–e).<sup>[3]</sup> MAPbI<sub>3</sub> and MAPbBr<sub>3</sub> are known to have a great miscibility.<sup>[56,57]</sup> For MAPbI<sub>3-x</sub>Br<sub>x</sub> perovskites, the absorbance spectra tend to blue-shifted along with the bromide content. The film color changes from dark brown to yellow at two extremes of x = 0 and 1, respectively. Nonlinear variation of the band-gap is observed due to the anisotropic nature of binding and structural change of the crystal.<sup>[3,56]</sup> In contrast to the case of bromide, chloride inclusion in MAPbI<sub>3</sub> perovskite appears to be limited to a maximum of 3–4 at% Cl. This is attributed to the low miscibility of chloride with iodide, presumably arising from the large difference in their ionic radii.<sup>[58–60]</sup> Nevertheless, chloride implication results in longer diffusion length and carrier life time than pure iodide perovskite based devices.<sup>[4]</sup> Band-gap control by halide substitution has demonstrated red, green, and blue emission for I-, Br-, and Cl-based perovskites, respectively.<sup>[47,61]</sup> A wide band-gap also enables high voltage output

( $\approx 1.5$  eV) from single-layer solar cells devices, which is potentially useful for tandem devices, water-electrolysis, or photocatalytic water splitting systems.<sup>[62,63]</sup>

### 2.2.2. Photogenerated Carrier Behavior

An exciton is neutral quasi-particle composed of a bound electron-hole pair by electrostatic Coulombic attraction.<sup>[64,65]</sup> Representative types of excitons are schematically described, indicating Wannier-Mott type excitons ( $E_b < 0.1$  eV) and Frenkel type excitons ( $E_b > 0.1$  eV) (Figure 3).<sup>[66]</sup> Optoelectronic devices are based on the behavior of excitons generated by external stimulation of semiconducting materials such as light absorption and external bias, thus, the understanding of exciton behavior of a perovskite is crucial for the exploration hybrid perovskites as promising optoelectronic materials. When the hybrid perovskite was in the limelight, it was unclear whether absorption of photons existed as excitons or free electrons and holes for 3D perovskites such as MAPbI<sub>3</sub> and MAPbI<sub>3-x</sub>Cl<sub>x</sub>, although they showed excellent material properties such as long carrier diffusion length over the micrometer scale and high absorption coefficients. This was due to the low  $E_b$  at room temperature ranging from 2 to 50 meV compared with thermal energy of  $k_B T \approx 25$  meV.<sup>[67,68]</sup> It is now commonly accepted that perovskite solar energy harvesters spontaneously generate free electrons and holes, which greatly contribute to the impressive performance in photovoltaics.<sup>[69,70]</sup>

In addition to interest in perovskite solar cells based on light absorption, research interest in light emission from the hybrid perovskites is dramatically increasing. The reason why the hybrid perovskite is accepted for various optoelectronic applications is due to the widespread optoelectronic properties and minimal non-radiative recombination.<sup>[71]</sup> Depending on the target applications, suitable optoelectronic properties including  $E_b$ , diffusion length and lifetime, are required. For example, solar cells require low  $E_b$  for the efficient separation of excitons into free electron and holes, whereas LEDs need tightly bound excitons for efficient radiative decay. The management of hybrid perovskite materials, crystalline structure, and dimensionality enable a broad scope of exciton binding energies ranging from 2 to a few hundred meV. Table 2 summarizes  $E_b$  of various hybrid perovskite materials along with crystal structures and dimensions, which are measured by magneto-optical absorption, optical absorption, temperature-dependent photoluminescence, and ellipsometry.



Wannier-Mott exciton

Frenkel exciton

**Figure 3.** Schematic illustration of representative exciton (bound electron-hole pair) models.

Polycrystalline perovskites usually used as light harvesters, such as MAPbI<sub>3</sub>, MAPbI<sub>3-x</sub>Cl<sub>x</sub>, and FAPbI<sub>3</sub>, have  $E_b$  values less than 20 meV, which is lower than the thermal energy (25 meV). Their excitons are close to Wannier-Mott type and such low  $E_b$  is one of fundamental reasons for the outstanding photovoltaic device performance of the hybrid perovskites. In 2014, Qianqian et al. reported that  $E_b$  of MAPbI<sub>3</sub> is on the order of 2 meV due to highly static dielectric constant of 70. This clarifies that principal working mechanism of photovoltaic is non-excitonic at room temperature.<sup>[67]</sup> One year later, Atsuhiko et al. demonstrated the direct measurement of  $E_b$  of MAPbI<sub>3</sub> perovskite using very high magnetic field for accurate investigation.<sup>[70]</sup> Tetragonal phase of MAPbI<sub>3</sub> at room temperature shows  $E_b$  only a few meV and it has 16 meV with orthorhombic phase at low temperature, indicating that free electrons and holes are generated immediately following light absorption.

It has been recognized that perovskite light emitter, such as MAPbBr<sub>3</sub>, has more population of bounded excitons due to higher  $E_b$  (few tens of meV to few hundred meV) compared with other light harvesters. In 2015, Ye et al. carried out comparative study of  $E_b$  between polycrystalline MAPbI<sub>3</sub> and MAPbBr<sub>3</sub> using optical spectroscopy.<sup>[73]</sup>  $E_b$  values of lead-bromide and lead-iodide based perovskites were found to be 40 and 13 meV, respectively. Therefore, MAPbBr<sub>3</sub> shows 3–4 times slower charge carrier recombination rates than MAPbI<sub>3</sub>. In addition,  $E_b$  can be considerably increased depending on the crystal size and film morphology.<sup>[73]</sup> In 2015, Kaibo et al. revealed that excitons in 8 nm colloidal nanoparticles of MAPbBr<sub>3</sub> are much more tightly bound than micro-crystallite of MAPbBr<sub>3</sub>, with corresponding  $E_b$  of 320 and 84 meV, respectively.<sup>[75]</sup> This suggests that the probability for radiative recombination is significantly increased in MAPbBr<sub>3</sub> nanoparticles and explains the high fluorescence quantum efficiency of these nanoparticles.

Low-dimensional perovskite, composed of much large and complex organic cations ill-fitting to form a 3D perovskite structure, shows large  $E_b$  over 100 meV, which is closer to Frenkel excitons. The theoretical study by Koutselas et al. revealed that  $E_b$  and the energy band gap of hybrid perovskites increases along with the decreasing dimensionality of perovskite.<sup>[76]</sup> For 2D perovskites, the metal-halide frameworks and the large organic cations are alternated to induce well and barrier electronic structures with different dielectric constants (e.g., small dielectric constant for the organic cations). This smaller dielectric constant and dielectric confinement effect of low-dimensional perovskites by forming quantum wells sandwiched between organic barrier layers enhance the excitonic effect and, thereby, increase  $E_b$ .<sup>[77]</sup> Further decreases in dimensionality toward 1D and 0D perovskite demonstrate markedly high  $E_b$  due to the large on-site Coulomb energy in octahedrons.<sup>[79]</sup> Therefore, nanoscale 3D perovskite and low dimensional perovskite are considered as promising luminophores for LEDs and lasers.

### 2.2.3. Energy-Level Alignment

Perovskite optoelectronic devices, especially solar cells and LEDs, usually stand on the basis of the heterojunction between the perovskite and the electron/hole charge transport materials

**Table 2.** Exciton binding energies of various organic-inorganic hybrid perovskites.

Perovskite materials	Morphology	Dimension	$E_b^a$ [meV]	Measurement method	Ref.
$\text{CH}_3\text{NH}_3\text{PbI}_3$	Polycrystalline	3D	16	Magneto-optical absorption spectroscopy	[70]
	Polycrystalline	3D	22	Magneto-optical absorption spectroscopy	[72]
	Polycrystalline	3D	2	Spectroscopic ellipsometry	[67]
	Polycrystalline	3D	13	Optical absorption	[73]
	Polycrystalline	3D	7	Electroabsorption spectroscopy	[8]
	Polycrystalline	3D	12	Magneto-optical absorption spectroscopy	[74]
$\text{CH}_3\text{NH}_3\text{PbBr}_3$	Microcrystalline	3D	84	X-ray spectroscopy/Temperature dependent PL <sup>b)</sup>	[75]
	Nanoparticle	3D	320	X-ray spectroscopy	[75]
	Polycrystalline	3D	76	Magnetoabsorption	[72]
	Polycrystalline	3D	40	Optical absorption	[73]
$\text{CH}_3\text{NH}_3\text{PbI}_{3-x}\text{Cl}_x$	Polycrystalline	3D	55	Optical absorption	[68]
	Polycrystalline	3D	10	Magneto-optical absorption spectroscopy	[74]
$\text{CH}(\text{NH}_2)_2\text{PbI}_3$	Polycrystalline	3D	10	Magneto-optical absorption spectroscopy	[74]
$\text{CH}(\text{NH}_2)_2\text{PbBr}_3$	Polycrystalline	3D	24	Magneto-optical absorption spectroscopy	[74]
$(\text{C}_9\text{H}_{19}\text{NH}_3)_2\text{PbI}_4$	n/a	2D	>330	Temperature dependent PL	[76]
$(\text{C}_{10}\text{H}_{21}\text{NH}_3)_2\text{PbI}_4$	Single crystal	2D	370	Optical absorption	[77]
$(\text{C}_6\text{H}_5\text{C}_2\text{H}_4\text{NH}_3)_2\text{PbI}_4$	Polycrystalline	2D	350	Optical absorption	[78]
$(\text{NH}_2\text{C}(\text{I})=\text{NH}_2)_3\text{PbI}_5$	n/a	1D	>410	Optical absorption	[76]
$(\text{CH}_3\text{NH}_3)_4\text{PbI}_6 \cdot 2\text{H}_2\text{O}$	n/a	0D	545	Optical absorption	[76]

<sup>a)</sup>  $E_b$ : exciton binding energy, <sup>b)</sup> PL: photoluminescence.

that perform the diode function. Most of device architectures for perovskite solar cells and LEDs adopt n-i-p or p-i-n type heterojunction between substrate and top-electrode, where n, i, p mean electron transport materials (ETM), hybrid perovskites, and hole transport materials (HTM), respectively. Apart from the manipulation of perovskite electro-optical properties, the energy band alignment with ETM and HTM layers is also essential for an optimal device operation involving charge carrier injection, extraction, exciton confinement, and quenching. In general, interfacial layers require charge carrier selectivity (ability to block carriers of the opposite charge), optimized energy band offset to the active material, as well as sufficient electric conductivity, etc. Furthermore, easy solution processing at low temperature is desirable for the demands for flexible and wearable electronics.

To date, most of perovskite optoelectronic devices adopt the common interfacial layers already used in the related technologies such as dye-sensitized solar cells, organic solar cells, and organic light-emitting diodes. Various materials, including organic polymers, small molecules, metal oxide, and inorganic crystals, have been used as interfacial materials. The energy band diagrams of representative electron and hole transport materials and hybrid perovskites are summarized in **Figure 4**. Energy levels of perovskites show that the conduction band minimum (CBM) and valence band maximum (VBM) are distributed from 3.1–4.2 eV and 5.4–6.1 eV, respectively. For ETM, CBM ranges from 3.5–4.3 eV with deep VBM for efficient hole blocking. Currently, mesoporous titanium dioxide (mp-TiO<sub>2</sub>) is most widely used but high sintering temperature around 500 °C prohibits its use for flexible substrates. In this

respect, ZnO, SnO<sub>2</sub>, and organic small molecules are considered as alternatives.<sup>[5,80–82]</sup> For low-temperature processing and high-performance flexible solar cells, Zn<sub>2</sub>SnO<sub>4</sub> ETM performed well with the perovskite light harvester, demonstrating 15% efficiency with a low temperature process below 100 °C.<sup>[83]</sup> As particular cases, the CBM of the ETM and perovskite shows an energy level mismatch due to a wide range of CBM of the

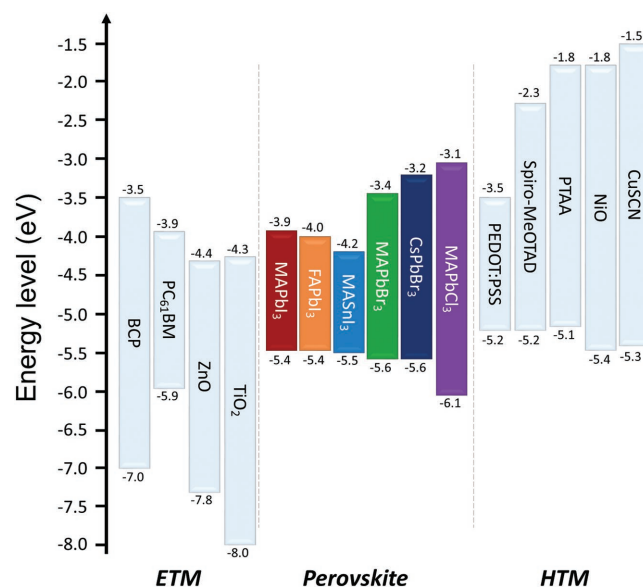


**Figure 4.** Schematic energy band diagram of various hybrid perovskites with electron- and hole-transport materials (ETM and HTM, respectively).



perovskite, resulting in a large barrier to electron injection and deteriorated open-circuit voltage for solar cells.<sup>[84]</sup> Appropriate energy level matching has been pursued by the modification of ETMs via doping, self-assembled monolayer treatment, and mixed ETMs.<sup>[85–88]</sup> In contrast, the VBM of the HTM, located around 5.1–5.4 eV, is relatively well-matched to the VBM of the perovskite. Spiro-MeOTAD and PTAA are widely used in n-i-p structures, while poly(3,4-ethylenedioxythiophene):poly-styrene sulfonate (PEDOT:PSS) or modified compositions (e.g., PEDOT:PSS/perfluorinated ionomer) are mostly adopted in p-i-n structures.<sup>[61,89,90]</sup> Similar to the ETM, the modification of HTMs by polymer mixture, lithium salt doping, and chemical modification enhances energy level matching and conductivity of materials.<sup>[91–94]</sup> Nonetheless, recent research is moving toward dopant-free HTMs, such as NiO, as the deliquescent nature of the dopant may readily aggravate device performance.<sup>[95–97]</sup>

### 2.3. Perovskite Film Deposition Methods

Hybrid crystalline structure composed of organic and inorganic components facilitates low-temperature solution processing of hybrid perovskite materials. Various deposition methods including conventional spin-coating with and without anti-solvent dripping, vacuum evaporation, sequential deposition (two-step process), slot-die coating, spray coating, doctor blading, etc. have been reported.<sup>[98–104]</sup> It is well-known that the optoelectronic characteristics of perovskite materials are directly connected to the film morphology and quality. Homogeneous and uniform film deposition is essential to obtain high-performance perovskite-based optoelectronic devices.

In the initial stage of hybrid perovskite research for optoelectronics, a single-step spin-coating method was used for crystalline perovskite particles<sup>[20,105]</sup> and thin films<sup>[21,106]</sup> on mp-TiO<sub>2</sub> commonly using a precursor solution of mixed MAI and PbI<sub>2</sub> based on polar solvents, such as dimethylformamide (DMF), dimethyl sulfoxide (DMSO), gamma-butyrolactone (GBL), etc. Although spin-coating is an apparently simple and low-cost deposition method, strong ionic interaction between metal cations and halogen anions commonly leads to the formation of inhomogeneous film morphology involved with poor surface coverage,<sup>[107]</sup> pillared structure,<sup>[106]</sup> and non-uniform film thickness.<sup>[100]</sup>

In 2014, anti-solvent dripping method was developed for highly uniform and homogeneous perovskite film formation (Figure 5a). Anti-solvents to perovskite such as toluene and chlorobenzene are dripped during the spinning of precursor solutions.<sup>[98,107]</sup> This simple approach results in homogeneous perovskite layers over large area. Anti-solvent dripping is known to induce rapid supersaturation of perovskite precursors film, thus promotes a fast nucleation and growth of perovskite films. In the case of precursor solutions containing DMSO, kinetically frozen uniform layer of MAI-PbI<sub>2</sub>-DMSO is formed as an intermediate phase. Solid-state conversion from the intermediate phase film to perovskite film by thermal annealing yields remarkably uniform and dense perovskite films via the delayed reaction between the organic and inorganic precursors. The type of anti-solvent, dripping timing, and spinning rate are

key factors influencing the final perovskite film morphology. Benzene derivatives, diethyl ether, and chloroform are reported to be effective anti-solvents for selective washing of DMF with high reproducibility.<sup>[14,39,108]</sup> Depending on the solvent used in the precursor solution, anti-solvent and dripping timing should be carefully controlled for highly efficient optoelectronic devices.

In contrast to the single-step spin-coating from premixed organic–inorganic precursor solution, perovskite can be synthesized by a sequential deposition of inorganic and organic components, called two-step process (Figure 5b).<sup>[109,110]</sup> The inorganic component is spin-coated prior to organic component deposition. Contact between the two components initiates the phase transition to the perovskite structure. Thermal annealing that follows completes perovskite crystal formation by the interdiffusion of two components. Solution and vapor deposition are available for organic components onto inorganic components.<sup>[109,111]</sup> It is reported that cuboidal structure of perovskite crystal<sup>[99]</sup> or conventional polycrystalline perovskite<sup>[112]</sup> is observed depending on the concentration of organic components.<sup>[110,112]</sup> Perovskite morphology can be controlled by the concentration of the organic component, inorganic component preparation, thermal annealing, and so on. Because the phase conversion propagates from the surface of inorganic halide to inner volume, this method is insufficient for creating high-quality perovskite layer over a thick layer and planar architecture due to an incomplete phase conversion. To improve the crystallization process, Yang et al. reported intramolecular exchange of the organic component and DMSO using PbI<sub>2</sub>-DMSO composites as the inorganic component.<sup>[44]</sup> Complete and fast conversion to perovskite was observed with preferred crystal orientation and excellent device performances.

Flat and uniform hybrid halide perovskite film is also obtainable by a vapor deposition method for planar architecture (Figure 5c).<sup>[100]</sup> Dual source evaporation of organic and inorganic components, a mature technique, enables formation of perovskite over large area with superior interface properties of multi-stacked layers. In the report by Liu et al., vapor evaporation of mixed halide perovskite showed more uniform film thickness and coverage than a conventional solution process.<sup>[100]</sup> The hybrid tandem structure and/or all-perovskite multi-junction can be easily realized because of the inherent advantages, including easy deposition of multi-layers, interface property between layers, and compatibility with conventional processing methods of thin-film solar cells.

As solution-processed perovskite solar cells showed a high performance over 20%, which is comparable to top quality single junction silicon solar cells that currently dominate the photovoltaic market, demand for scalable fast processing of perovskite materials is increasing. Slot-die coating, spray deposition and doctor blading of perovskite have been reported (Figure 5d–f) as alternatives to non-scalable conventional spin-coating.<sup>[101–104]</sup>

Hwang et al. demonstrated the fabrication of fully slot-die coated perovskite solar cells.<sup>[101]</sup> Major advantages of the slot-die coating method are the formation of uniform stripe with well-defined edges and minimized material loss. A pin-hole-free perovskite layer is well-coated by sequential slot-die coating method with nitrogen gas quenching. A cuboid perovskite



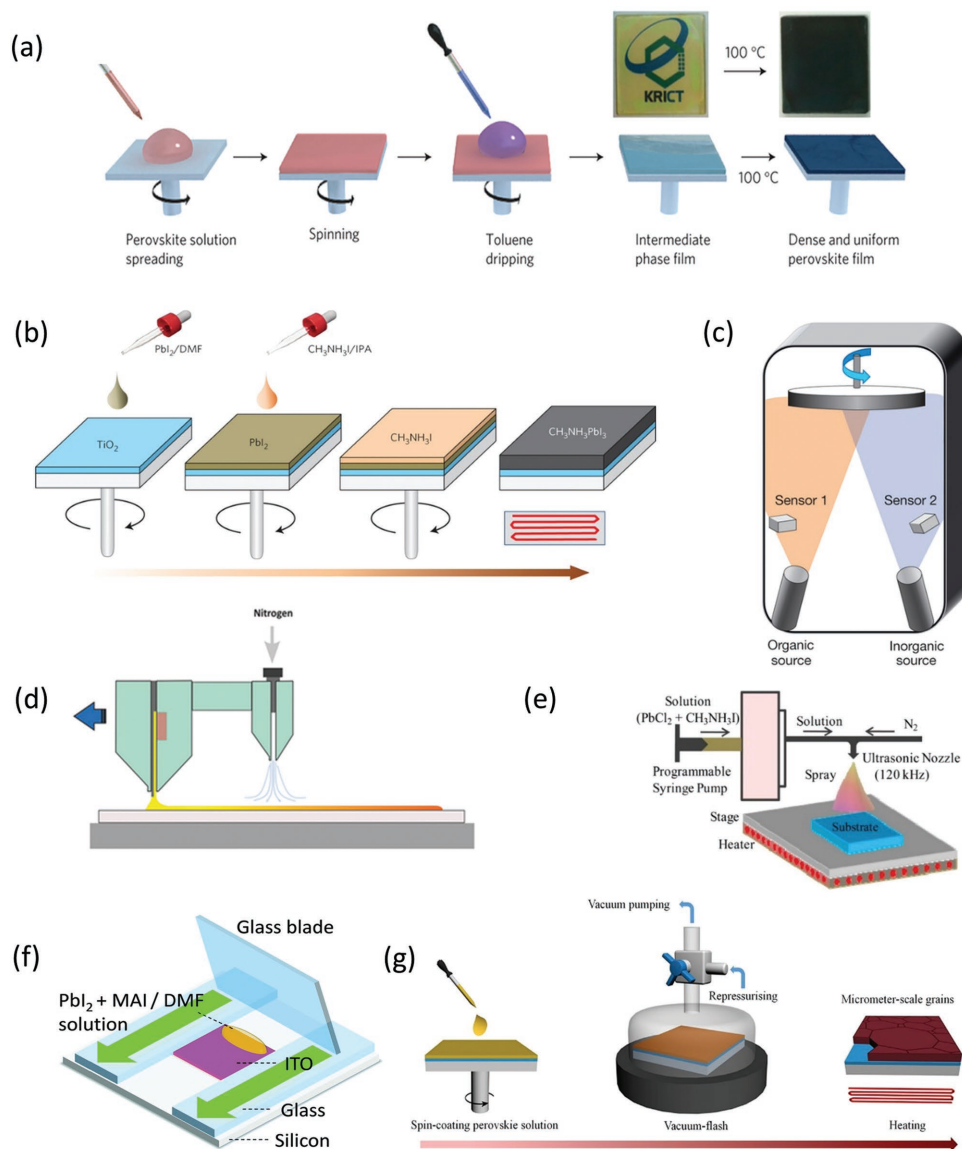


**Figure 5.** Various perovskite film deposition methods. a) Spin-coating with anti-solvent dripping during the spinning of precursor solution. Reproduced with permission.<sup>[98]</sup> Copyright 2014, Nature Publishing Group. b) Two-step sequential deposition by spin-coating. Reproduced with permission.<sup>[99]</sup> Copyright 2014, Nature Publishing Group. c) Vapor deposition (co-evaporation) method. Reproduced with permission.<sup>[100]</sup> Copyright 2013, Nature Publishing Group. d) Slot-die coating. Reproduced with permission.<sup>[101]</sup> Copyright 2015, Wiley. e) Spray-coating. Reproduced with permission.<sup>[103]</sup> Copyright 2015, American Chemical Society. f) Doctor blading. Reproduced with permission.<sup>[104]</sup> Copyright 2015, Royal Society of Chemistry. g) Vacuum flash-assisted solution process. Reproduced with permission.<sup>[113]</sup> Copyright 2016, The American Association for the Advancement of Science.

crystal with a promising device performance is obtained. Unfortunately, this process is limited in terms of using heated substrate and jet nozzle for efficient crystallization of sequentially deposited inorganic and organic precursors.

Spray-coating has also been explored for scalable deposition of mixed halide perovskite (Figure 5e).<sup>[102,103]</sup> This method has been successfully exploited for organic optoelectronics including solar cells, light-emitting diodes, and photodetectors. Precursor solution is ultrasonically spray-coated onto a pre-heated substrate under ambient condition using a 120 kHz nozzle and then thermally annealed. Film coverage and density showed a strong correlation with device performance. It is usually controllable by substrate temperature and volatility

of solvent. A low temperature process enables the efficient demonstration of mixed halide perovskite solar cells with an efficiency over 13 and 8% on glass and PET substrates, respectively. The necessity of thermal annealing slows down the overall processing speed despite the efficient deposition of perovskite layers.

Doctor-blade coating also offers many attractive features for large area deposition of hybrid perovskites, including scalability, low-temperature, simplicity, and compatibility with roll-to-roll fabrication (Figure 5f). In 2015, Dent et al. demonstrated a doctor-bladed  $\text{MAPbI}_3$  perovskite active layer for solar cells.<sup>[104]</sup> Perovskite precursor solution is swiped linearly by a glass blade with a speed of 27 m h<sup>-1</sup> with substrate heating.

Film thickness is controllable by the depth of blading channel and solution concentration. Perovskite solar cells with doctor-bladed perovskite show higher power conversion efficiency than that of spin-coated perovskite due to larger grain size by slower crystallization than conventional spin-coating. Nevertheless, the necessity for thermal annealing and further purification of materials is pointed out as a critical problem to address.

Recently, Li et al. reported a new perovskite deposition method called vacuum flash-assisted solution process for highly crystalline smooth perovskite films.<sup>[113]</sup> Previous deposition methods using anti-solvents have spatial inhomogeneity and are toxic for the environment when used in large-area solution processes.<sup>[39,98]</sup> These limitations are addressed by vacuum-flash treatment during the solution processing of perovskites, which promotes rapid crystallization of the perovskite intermediate phases. A few second storage of as-coated films in vacuum with 20 Pa allows excellent infiltration of perovskite into the mesoporous scaffold and continuous polycrystalline grains. Therefore, 20.5% of the maximum efficiency is observed with an active area exceeding 1 cm<sup>2</sup>.

### 3. Crystallization Methods for Perovskite Light Harvesters

#### 3.1. Heat Treatment

Thermal annealing has been the mostly widely used method for the crystallization of solution-deposited perovskite precursor films accompanied by the evaporation of residual solvents and low molecular additives.<sup>[29,114]</sup> The perovskite film quality, morphology, and material properties are greatly influenced by this step provided that the precursor film is completely wet on a substrate. Although interesting attempts to form perovskite crystal without thermal annealing were carried out in recent years, film quality and device performance of state-of-the-art devices still largely rely on this approach.<sup>[115,116]</sup> The manipulation of process variables, including annealing temperature, duration time, temperature rise profile, and substrate pre-heating offers an opportunity to optimize perovskite thin-film by controlling crystalline nucleation and growth kinetics. A summary of the performance of perovskite solar cells based on various crystallization methods is presented in **Table 3**.

Thermal annealing temperature and duration time are the two most important parameters for perovskite morphology evolution. In 2013, Eperon et al. investigated the correlation between thermal annealing time and morphology, especially film coverage, of mixed halide perovskite MAPbI<sub>3-x</sub>Cl<sub>x</sub> formed by single step spin-coating (**Figure 6a**).<sup>[118]</sup> As-deposited films show a high coverage with small pores. Thermal annealing at 100 °C induced small pores until 10 min, then large grains of the perovskite are developed with further annealing along with the formation of large pores. Annealing temperature also significantly influences on the film morphology and surface coverage. Generally, at a high temperature, the uniformity of layer is degraded with the formation of large pores (**Figure 6b**), which crucially affects area dependent solar cell parameters such as short circuit current (*J*<sub>sc</sub>) and power conversion efficiency (PCE). Optical properties and crystallinity of perovskite films

are also investigated as a function of annealing temperature by Dualeh et al.<sup>[117]</sup> They reported that sufficiently high temperature is required for the complete evaporation of solvents and crystallization of perovskite. However, PbI<sub>2</sub> formation, which is detrimental for device performance, is observed due to the thermal decomposition of perovskite phase. Optical absorption spectra of the perovskite layers formed by different annealing temperatures ranging from 60 to 200 °C (**Figure 6c**) shows phase development toward perovskite and the decomposition of phase. As-deposited film comprised of PbCl<sub>2</sub> and MAI has poor optical absorption without onset at 770 nm. Annealing temperature from 60 to 150 °C increases optical absorption in the measured wavelength range, indicating that the extent of phase transformation into perovskite increases with temperature. Further increase of temperature induces a decreases in absorption with the emergence of PbI<sub>2</sub> absorption peak at 550 nm, confirming the thermal decomposition of perovskites.<sup>[147,148]</sup>

A two-step process based on the sequential deposition of inorganic and organic precursors also uses thermal annealing for perovskite crystal formation.<sup>[109,110,149,150]</sup> Bi et al. investigated the effect of thermal annealing on structural, electrical, and optical properties of MAPbI<sub>3</sub> perovskite.<sup>[112]</sup> It is noteworthy that thermal annealing works differently for perovskite films prepared from premixed solution and sequential deposition of inorganic/organic precursors.<sup>[151,152]</sup> In the case of two-step process, thermal energy drives interdiffusion of both precursor species and leads to the formation of perovskite. Interestingly, thermal annealing influences not only the optical property but also influences the electrical characteristics. Because MAPbI<sub>3</sub> formed by interdiffusion methods shows p-type conductivity,<sup>[149]</sup> the hole concentration and Hall mobility are investigated. The hole concentration and Hall mobility tend to decrease and increase, respectively, along with annealing time. This indicates that thermal annealing reduces acceptor-like defect states and enhances the crystallinity and grain size of perovskite. UPS (ultraviolet photoelectron spectroscopy) studies confirm the Fermi level shift from the valence band side toward the middle of the band-gap with annealing time, which coincides with decreases in hole concentration (**Figure 6d**). Energetic variation of the perovskite layer results in a shift of open-circuit voltage (*V*<sub>oc</sub>). Optimum device performance is achievable without severe thermal degradation of perovskite layers.

The interrelated effects of annealing temperature and duration time raises an interesting question: how does the variation in annealing conditions influence the perovskite film quality and solar cell performance while maintaining the total thermal budget (i.e., high temperature/short time vs. low temperature/long time). In 2014, Saliba et al. attempted to address this question using a mixed halide perovskite on mesoporous and planar device architectures. Short rapid annealing at 130 °C for 5 min produces micrometer-sized perovskite grains and improved solar cell performance, especially *J*<sub>sc</sub>, compared to the sample annealed at 100 °C for 45 min, which results in the grain size of a few hundred nanometers.<sup>[122]</sup> According to this attempt, a rapid annealing effect is observed depending on various device architectures. In a planar structure, enlarged grains and enhanced crystallinity with surface coverage over 95% results in a high efficiency, whereas device performance is degraded due

**Table 3.** Summary of solar cell performance with various crystallization methods.

Method	Device structure with materials	$V_{oc}$ [V]	$J_{sc}$ [mA cm <sup>-2</sup> ]	FF [%]	PCE Best [%]	PCE Ref. [%]	Enhancement [%]	Ref.
<b>Heat treatment</b>	FTO/c-TiO <sub>2</sub> /mp-TiO <sub>2</sub> /MAPbI <sub>3-x</sub> Cl <sub>x</sub> /Spiro-MeOTAD/Au	0.93	18.4	68	11.7	–	–	[116]
	FTO/c-TiO <sub>2</sub> /MAPbI <sub>3-x</sub> Cl <sub>x</sub> /Spiro-MeOTAD/Au	0.87	17.5	61	9.3	6.7	38	[117]
	ITO/TiO <sub>2</sub> /MAPbI <sub>3-x</sub> Cl <sub>x</sub> /P3HT/Ag	0.93	21.0	69	13.6	–	–	[118]
	FTO/PEDOT:PSS/MAPbI <sub>3-x</sub> Cl <sub>x</sub> /PC <sub>61</sub> BM/Al	0.94	22.4	83	17.5	–	–	[119]
	ITO/PEDOT:PSS/MAPbI <sub>3</sub> /PC <sub>61</sub> BM/C <sub>60</sub> /BCP/Al	0.96	21.0	76	15.6	7.3	114	[120]
	FTO/c-TiO <sub>2</sub> /MAPbI <sub>3-x</sub> Cl <sub>x</sub> /Spiro-MeOTAD/Ag	0.92	21.5	69	13.5	12.5	8	[121]
	ITO/PEDOT:PSS/MAPbI <sub>3-x</sub> Cl <sub>x</sub> /PC <sub>61</sub> BM/Al	0.90	16.7	74	11.1	8.3	34	[122]
	ITO/PEDOT:PSS/MAPbI <sub>3-x</sub> Cl <sub>x</sub> /PC <sub>61</sub> BM/PFN/Ag	1.00	20.7	72	14.9	11.1	35	[123]
<b>Additive</b>	FTO/PEDOT:PSS/MAPbI <sub>3-x</sub> Cl <sub>x</sub> /PC <sub>61</sub> BM/Bis-C <sub>60</sub> /Ag	0.92	17.5	73	11.8	9.0	31	[124]
	FTO/c-TiO <sub>2</sub> /mp-TiO <sub>2</sub> /MAPbI <sub>3</sub> /Spiro-MeOTAD/Au	1.00	22.1	75	16.7	8.8	90	[125]
	ITO/PEDOT:PSS/MAPbI <sub>3</sub> -PC <sub>61</sub> BM/PC <sub>61</sub> BM/Ca/Al	0.97	20.2	82	16.0	11.4	40	[126]
	FTO/c-TiO <sub>2</sub> /MAPbI <sub>3-x</sub> Cl <sub>x</sub> /Spiro-MeOTAD/Au	0.94	19.5	70	13.2	10.6	25	[127]
	FTO/PEDOT:PSS/MAPbI <sub>3-x</sub> Cl <sub>x</sub> /PC <sub>61</sub> BM/Bis-C <sub>60</sub> /Ag	0.94	18.5	75	13.1	9.8	34	[128]
	FTO/c-TiO <sub>2</sub> /MAPbI <sub>3-x</sub> Cl <sub>x</sub> /Spiro-MeOTAD/Au	0.98	22.9	69	14.8	8.5	74	[129]
	ITO/PEDOT:PSS/MAPbI <sub>3-x</sub> (SCN) <sub>x</sub> /PC <sub>61</sub> BM/Ca/Al	0.85	17.9	76	11.6	6.8	71	[130]
	ITO/PEDOT:PSS/MAPbI <sub>3</sub> /PC <sub>61</sub> BM/Ca/Al	0.88	14.1	80	9.9	8.2	22	[131]
	FTO/c-TiO <sub>2</sub> /MAPbI <sub>3</sub> /PTAA/Au	1.10	20.5	78	17.2	13.0	32	[132]
	FTO/c-TiO <sub>2</sub> /mp-TiO <sub>2</sub> /FAPbI <sub>3</sub> /Spiro-MeOTAD/Ag	1.04	18.9	68	13.4	–	–	[133]
	FTO/c-TiO <sub>2</sub> /mp-TiO <sub>2</sub> /FAPbI <sub>3</sub> /Spiro-MeOTAD/Au	0.94	23.3	65	14.2	–	–	[7]
	FTO/c-TiO <sub>2</sub> /MAPbBr <sub>3</sub> /PIF8-TAA/Au	1.51	8.4	82	10.4	–	–	[62]
<b>Vapor-assisted</b>	ITO/PEDOT:PSS/MAPbI <sub>3</sub> /PC <sub>61</sub> BM/C <sub>60</sub> /BCP/Al	0.96	21.0	76	15.6	11.5	36	[134]
	ITO/SnO <sub>2</sub> /MAPbI <sub>3</sub> /Spiro-MeOTAD/Ag	1.08	19.5	61	13.0	–	–	[135]
	ITO/PEDOT:PSS/MAPbI <sub>3</sub> /PC <sub>61</sub> BM/C <sub>60</sub> /BCP/Al	0.90	20.0	75	13.6	11.4	20	[136]
	FTO/PEDOT:PSS/MAPbI <sub>3-x</sub> Cl <sub>x</sub> /PC <sub>61</sub> BM/PFN/Al	1.05	20.3	80	17.1	12.3	39	[137]
	ITO/PEDOT:PSS/MAPbI <sub>3-x</sub> Cl <sub>x</sub> /PC <sub>61</sub> BM/LiF/Al	1.01	21.3	76	16.4	12.7	29	[138]
	FTO/c-TiO <sub>2</sub> /MAPbI <sub>3</sub> /Spiro-MeOTAD/Au	1.08	20.8	78	17.7	16.1	10	[139]
	ITO/PEDOT:PSS/MAPbI <sub>3</sub> /PC <sub>61</sub> BM/Ag	0.93	20.9	69	13.6	–	–	[140]
	FTO/c-TiO <sub>2</sub> /mp-TiO <sub>2</sub> /MAPbI <sub>3-x</sub> Cl <sub>x</sub> /Spiro-MeOTAD/Au	0.97	21.4	68	14.1	–	–	[141]
	FTO/c-TiO <sub>2</sub> /mp-TiO <sub>2</sub> /MAPbI <sub>3</sub> /Spiro-MeOTAD/Ag	1.08	19.6	71	15.1	5.7	165	[142]
	ITO/PEDOT:PSS/MAPbI <sub>3</sub> /PC <sub>61</sub> BM/PFN-Br/Ag	1.03	18.4	78	14.8	10.2	44	[143]
<b>Solvent mediator</b>	FTO/c-TiO <sub>2</sub> /mp-TiO <sub>2</sub> /MAPbI <sub>3</sub> /Spiro-MeOTAD/Ag	1.09	23.8	76	19.7	–	–	[39]
	FTO/c-TiO <sub>2</sub> /mp-TiO <sub>2</sub> /FAPbI <sub>3</sub> /PTAA/Au	1.06	24.7	78	20.2	–	–	[44]
	FTO/c-TiO <sub>2</sub> /mp-TiO <sub>2</sub> /MAPbI <sub>3-x</sub> Br <sub>x</sub> /PTAA/Au	1.11	19.6	74	16.2	–	–	[144]
	FTO/c-TiO <sub>2</sub> /MAPbI <sub>3-x</sub> Cl <sub>x</sub> /Spiro-MeOTAD/Au	0.89	18.4	78	12.9	–	–	[145]
<b>Laser</b>	ITO/PEDOT:PSS/MAPbI <sub>3</sub> /PC <sub>61</sub> BM/Ca/Al	0.89	16.8	80	12.6	11.2	13	[146]

Abbreviations:  $V_{oc}$ : open-circuit voltage,  $J_{sc}$ : short-circuit current, FF: fill factor, PCE: power conversion efficiency, FTO: fluorine-doped tin oxide, ITO: indium tin oxide, c-TiO<sub>2</sub>: compact (blocking) TiO<sub>2</sub>, mp-TiO<sub>2</sub>: mesoporous TiO<sub>2</sub>, PEDOT:PSS: poly(3,4-ethylenedioxythiophene):polystyrene sulfonate, MA: methylammonium, FA: formamidinium iodide, PC<sub>61</sub>BM: phenyl-C<sub>61</sub>-butyric acid methyl ester, BCP: bathocuproine, PTAA: poly[bis(4-phenyl)(2,4,6-trimethylphenyl)amine], PFN: poly[(9,9-bis(3'-(N,N-dimethylamino)propyl)-2,7-fluorene)-alt-2,7-(9,9-dioctylfluorene)], PIF8-TAA: poly[(2,4-dimethylphenyl)imino]-1,4-phenylene(6,12-dihydro-6,6,12,12-tetraoctylindeno[1,2-b]fluorene-2,8-diyl)-1,4-phenylene], P3HT: poly(3-hexylthiophene-2,5-diyl).

to the large pore generation in the perovskite capping layers of mesoporous structure.

In addition to the annealing temperature and time, ramp-up profile of the temperature toward a target temperature is another significant parameter for perovskite crystal growth and coverage, as it particularly influences the solvent evaporation rate. Kang et al. investigated the effect of the solvent evaporation

rate on the morphology and solar cell performance by means of spinning speed, air drying, and stepwise temperature increase for planar device structures.<sup>[123]</sup> Stepwise temperature increase from room temperature shows continuous perovskite thin-films with minimized number of pin-holes, while immediate thermal annealing of as-deposited film leads to the formation of large pores caused by rapid crystallization. Later, Xu et al.

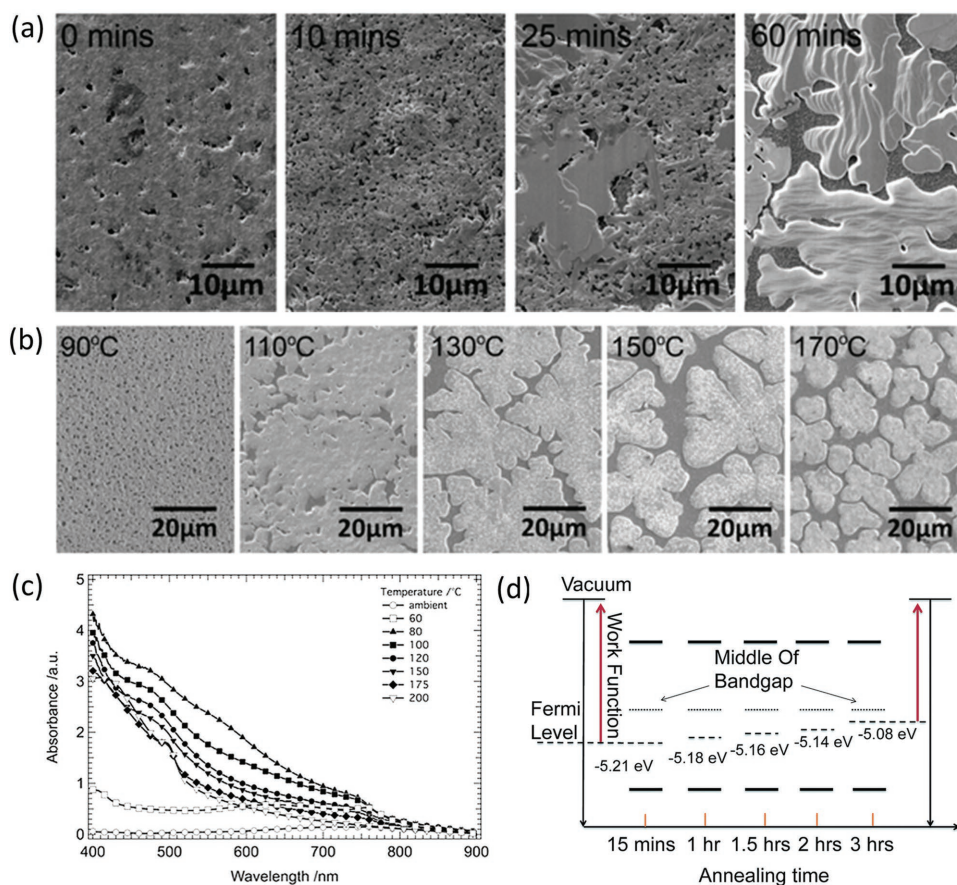


**Figure 6.** a) SEM images of perovskite films on compact  $\text{TiO}_2$ -coated FTO glass with 100 °C anneal times from 0 min to 60 min, carried out in nitrogen atmosphere. b) SEM images showing dependence of perovskite coverage on annealing temperature from 90 °C to 170 °C holding initial film thickness fixed at  $650 \pm 50$  nm. Panels (a,b) reproduced with permission.<sup>[118]</sup> Copyright 2013, Wiley. c) UV-vis absorption spectra from  $\text{mTiO}_2$  films with perovskite annealed at different temperature. Reproduced with permission.<sup>[117]</sup> Copyright 2014, Wiley. d) Energy band diagram of Fermi level shift during thermal annealing. Reproduced with permission.<sup>[112]</sup> Copyright 2014, Royal Society of Chemistry.

carried out gradual thermal annealing (6 °C per 10 min) from 50 to 80 °C for  $\text{MAPbI}_{3-x}\text{Cl}_x$  perovskite.<sup>[124]</sup> A similar trend was observed by Kang et al., who reported better surface coverage and solar cell efficiency compared to direct thermal annealing at 80 °C. Interestingly, the composition of halide ions, i.e., Cl/I percentage, is varied with the annealing procedure. The amount of Cl incorporated in the perovskite structure is measured to be 1.2–4.0% at different gradual annealing conditions, where 4% of Cl shows a higher PCE compared to conditions.<sup>[4,130,153]</sup>

Until now, we have focused on the thermal treatment methods following spin-coating. Several new heat management methods have also been introduced to obtain millimeter-sized grains, in contrast to the conventional post-annealing that typically results in grain sizes ranging from 100 to 1000 nm.<sup>[154]</sup> In 2015, Nie et al. presented a hot-casting method based on a solution process, where perovskite precursor solution heated at 70 °C is spin-coated onto pre-heated substrates at 180 °C.<sup>[120]</sup> In terms of perovskite film morphology, they succeed in the effective enhancement of perovskite grain size up to the millimeter scale, which is attributed to the prolonged grain growth in the presence of excess solvent at high temperature. Reduced grain boundaries and bulk defects result in fast charge carrier mobility and bimolecular

dominant recombination with a high PCE of 18% in a planar device architecture.

### 3.2. Additive Mediated Crystallization

Appropriate additives in perovskite precursor solution can facilitate the production of highly crystalline perovskite thin films without rigorous management of thermal annealing condition. Chemical additives can be beneficial for film homogeneity, carrier lifetime, surface coverage, and even device stability. Direct participation into the phase transformation process, including nucleation and growth, modulates reaction rate, and bonding characteristics. Currently, various types of additives, including organic halide ( $\text{MACl}$ ,  $\text{FACl}$ ,  $\text{NH}_4\text{Cl}$ ), organic di-halide (1,8-diiodooctane, 1,4-diiodobutane), pseudohalide ( $\text{Pb}(\text{SCN})_2$ ), acid ( $\text{HI}$ ,  $\text{HCl}$ ), and organic small molecules ( $\text{PC}_{61}\text{BM}$ ,  $\text{CN}$ ), have been investigated to improve the solar cell performance (see Table 3).

Organic halides, such as  $\text{MACl}$ ,  $\text{NH}_4\text{Cl}$ , and  $\text{FACl}$ , have commonly been used to improve perovskite film morphology, optoelectronic properties, and even device stability. Similar structures between organic precursor and organic halide



additives may offer good compatibility during crystallization process. Burschka et al. reported the sequential deposition method of  $\text{PbI}_2$  and MAI to form  $\text{MAPbI}_3$  in 2013.<sup>[109]</sup> Docampo et al. tried to enhance solar cell performance in a similar manner, which is the immersion of  $\text{PbI}_2$  thin-films into the mixture of MAI and MACl additive mixture.<sup>[130]</sup> In this attempt, device efficiency turned out to vary with the Cl concentration in dipping solutions. Time-resolved photoluminescence measurements revealed that the immersion in mixture of MAI and MACl improves the lifetime of photogenerated charge carriers. Zuo et al. reported the improved perovskite film crystallinity and morphology by using  $\text{NH}_4\text{Cl}$  additive in  $\text{MAPbI}_3$  perovskite.<sup>[132]</sup> Comparative study of MACl and  $\text{NH}_4\text{Cl}$  additives revealed that  $\text{NH}_4\text{Cl}$  additive shows a higher absorbance, smoother surface, and higher photogenerated charge carrier collection efficiency than MACl.

Li et al. recently reported one-step solution processing of perovskite solar cells using cross-linkable bifunctional alkylphosphonic acid  $\omega$ -ammonium chlorides.<sup>[126]</sup> Interestingly, this additive crosslinks adjacent perovskite grains through the strong hydrogen bonding between  $-\text{PO}(\text{OH})_2$  and  $-\text{NH}_3^+$  at the surface of perovskite (Figure 7a), thus smooth perovskite capping layer is achieved (Figure 7b). Furthermore, this additive induces a high loading of perovskite materials into mesoporous structure with enhanced surface area and percolated pathway (Figure 7c). Interestingly, device stability is also enhanced with the additives.  $\text{MAPbI}_3$  perovskite is very sensitive to moisture and is easily decomposed into volatile MAI and  $\text{PbI}_2$  due to

energetically unstable grain boundaries.<sup>[155]</sup> Air stability test with 55% of relative humidity showed that solar cells with the additives maintain its original PCE of 14% during a week and slowly degraded over an extended period of 1000 hours. A control device without the additives shows abrupt decreases of PCE from 7% to 1% over a week.

The role of organic halide additives for  $\alpha$ - $\text{FAPbI}_3$  formation was investigated by Wang et al. in 2015.<sup>[134]</sup> Increasing interest in  $\text{FAPbI}_3$  perovskite as an alternative to conventional  $\text{MAPbI}_3$  perovskite is attribute to the lower optical band-gap (1.43–1.48 eV) and better thermal stability.<sup>[7,156,157]</sup> However, control of the phase remains a key issue due to the polymorphic nature of  $\text{FAPbI}_3$  at ambient;  $\alpha$ - $\text{FAPbI}_3$  is trigonal perovskite with the band-gap of 1.5 eV and  $\delta$ - $\text{FAPbI}_3$  is non-perovskite phase with the band-gap of 2.48 eV.<sup>[38,156,158–160]</sup> The report by Wang et al. used  $\text{NH}_4\text{Cl}$ , MACl and FACL, which have different volatility for additive-modulated evolution of  $\alpha$ - $\text{FAPbI}_3$  on the mesoporous structure. While thermal annealing alone without additive is unable to form  $\alpha$ - $\text{FAPbI}_3$ , low volatility additives such as MACl and FACL enable the formation of desirable  $\alpha$ - $\text{FAPbI}_3$  by phase evolution through an additive-embedded intermediate phase.

Liang et al. reported the effect of an organic di-halide additive on the film formation process and solar cells performance.<sup>[125]</sup> As an additive, 1,8-diiodooctane (DIO), which is widely adopted in organic bulk-heterojunction solar cells, is used.<sup>[161–164]</sup> DIO is known to directly participate in the crystallization process of mixed halide perovskite via temporal bidentate chelating with

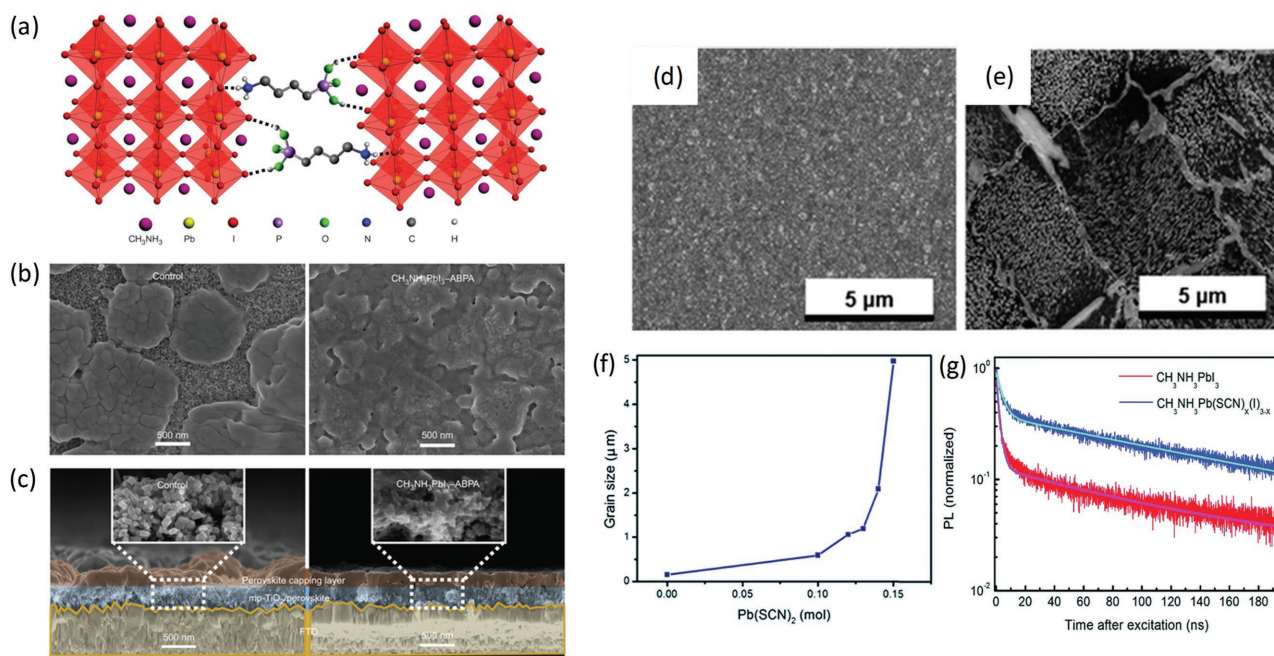


**Figure 7.** a) Schematic illustration of two neighboring grain structures in which the methyl ammonium groups are shown as one sphere for clarity, and the  $\text{PbI}_6^{4-}$  octahedra are shown in red, crosslinked by butylphosphonic acid 4-ammonium chloride (4-ABPACl) hydrogen-bonding interactions ( $\text{O}-\text{H}\cdots\text{I}$  and  $\text{N}-\text{H}\cdots\text{I}$ ) of the iodine from the iodoplumbate complex with the phosphoric acid ( $-\text{PO}(\text{OH})_2$ ) and the ammonium ( $-\text{NH}_3^+$ ) end groups of the 4-ABPACl species. SEM images of (b) surface and (c) cross-section of pristine (control) and 4-ABPA-anchored ( $\text{MAPbI}_3$ -ABPA) perovskite films deposited on mp- $\text{TiO}_2$ /FTO substrates by one-step spin-coating. Panels (a–c) reproduced with permission.<sup>[126]</sup> Copyright 2015, Nature Publishing Group. SEM images of  $\text{MAPbI}_3$  films (d) without and (e) with 0.15 mol of  $\text{Pb}(\text{SCN})_2$  additive, showing that large crystal grain growth with pseudohalide additive. (f) Average grain size of polycrystalline  $\text{MAPbI}_3$  perovskite along with the concentration of  $\text{Pb}(\text{SCN})_2$  additive. (g) Time-resolved photoluminescence of controlled  $\text{MAPbI}_3$  and  $\text{MAPb}(\text{SCN})_x\text{I}_{3-x}$ . Panels (d–g) Reproduced with permission.<sup>[131]</sup> Copyright 2016, Royal Society of Chemistry.

$\text{Pb}^{2+}$  residing in axial octahedral position on  $\text{Pb}^{2+}$ . Because bidentate chelation is thermodynamically more favorable than a monodentate one, chelation between DIO and  $\text{Pb}^{2+}$  leads to the retardation of phase transformation kinetics. More homogeneous perovskite films with fewer defects are attained and photogenerated charge carrier lifetime is also improved. Consequently, PCE is improved from 9% to 12%. Following this work, Chueh et al. reported the effects of various alkyl halide additives, including different chain length and halide ions, on solar cell performance.<sup>[129]</sup> Systematic study of the different chain lengths of diiodo alkanes, such as 1,4-diiodobutane (1,4-DIB), 1,10-diiododecane (1,10-DID), and 1,8-DIO, revealed that the short length of the alkyl chain is desirable for enhanced photovoltaic performance. Perovskite solar cells with 1,8-DIO and 1,4-DIB present 11.6% and 13.1% efficiency, respectively, because the short chains tend to easily form the chelation with  $\text{Pb}^{2+}$  and vice versa. In contrast, different halogen ions ( $\text{X} = \text{Cl}^-$ ,  $\text{Br}^-$  and  $\text{I}^-$ ) at the end of alkyl chain influence the solvent–solute interaction due to the difference in C–X bonding strength. Easy dissociation of C–X bond is preferred to coordinate into perovskite structures during the phase transformation. However, it is known that residual alkyl halide additives significantly deteriorate solar cells performance, thus, proper thermal annealing condition should be guaranteed.

Heo et al. demonstrated the control of crystallization process during simple single-step spin-coating process by the introduction of hydrobromic acid (HBr) into precursor solution of  $\text{MAPbBr}_3$  in DMF.<sup>[62]</sup> A pin-hole-free, dense  $\text{MAPbBr}_3$  film rather than an island morphology results in superior solar cell performances with over 10% efficiency and a very high  $V_{\text{oc}}$  of 1.51 V. HBr additives increase the solubility of  $\text{MAPbBr}_3$  in the solvent, thus nucleation is initiated at a higher concentration of  $\text{MAPbBr}_3$  wet film. Edge-initiated crystallization is propagated toward the center of film due to the higher solvent evaporation rate of edge-side than center by centrifugal force. Hydroiodic acid (HI) additives into  $\text{MAPbI}_3$  precursor in DMF also showed a similar effect for film nucleation and crystallizations and subsequently dense film formation.<sup>[121]</sup> Interestingly, planar heterojunction solar cells demonstrates 17% of PCE regardless of voltage scan rate with minimized hysteresis, which is attributed to the improved film homogeneity, fast charge transfer, long diffusion length, and 10-fold low trap density of  $\text{MAPbI}_3$  film.

In 2016, Kim et al. reported the effects of pseudohalide additive,  $\text{Pb}(\text{SCN})_2$ , on the crystal growth kinetics and device performance.<sup>[131]</sup> Pseudohalide is a halide material consisting of multi-atom, including nitrogen instead of halogen ions. Recently, pseudohalide has received particular attention because of its moisture resistance and radiative recombination efficiency.<sup>[153–155]</sup> In this attempt,  $\text{Pb}(\text{SCN})_2$  was added to the pre-mixed  $\text{MAPbI}_3$  precursor, which resulted in a wide range control of perovskite grain size from the nanoscale to microscale (up to 5  $\mu\text{m}$ ) along with the additive concentration (Figure 7d–f). Considering the nucleation and growth process,  $\text{Pb}(\text{SCN})_2$  raises the Gibbs free energy for nucleus formation at room temperature and, therefore, a lower density of stable nuclei is generated within  $\text{Pb}(\text{SCN})_2$  compared to pristine  $\text{MAPbI}_3$ . Final perovskite films show  $\text{MAPbI}_{1-x}(\text{SCN})_x$ , which is verified using Fourier transform infrared spectroscopy. The films also showed enlarged grain structure and improved

carrier lifetime (Figure 7g).  $\text{MAPbI}_3$  and  $\text{MAPbI}_{1-x}(\text{SCN})_x$  solar cells present 6.1% and 11.6%, respectively, under an identical device fabrication process. The role of  $\text{Pb}(\text{SCN})_2$  additive during perovskite crystallization is investigated by W. Ke et al.<sup>[165]</sup> Interestingly, the reaction between  $\text{CH}_3\text{NH}_3^+$  and  $\text{SCN}^-$  produces gaseous HSCN and  $\text{CH}_3\text{NH}_2$  during the crystallization. Gaseous  $\text{CH}_3\text{NH}_2$  is well-known to enlarge the grain size of perovskites.<sup>[143]</sup> Therefore, overall film quality is improved by the reduction of grain boundaries, improvement of crystallinity, and passivation of grain boundaries by excess  $\text{PbI}_2$ .

An interesting attempt to utilize organic small molecules without any halogen was recently reported. Chiang et al. demonstrated perovskite bulk-heterojunction solar cells by using  $\text{PC}_{61}\text{BM}$  additive in perovskite active layers.<sup>[127]</sup> Bulk-heterojunction is a widely adopted concept in the field of organic solar cells, which are composed of the random mixture of organic donor and acceptor molecules.<sup>[166–168]</sup> A two-step process was used to address the different solubility of perovskite precursors and organic small molecules. In this report, 0.1 mg  $\text{mL}^{-1}$  of  $\text{PC}_{61}\text{BM}$  was introduced for  $\text{PbI}_2$  solution in DMF and MAI resolved in 2-propanol. As a result, large grain  $\text{MAPbI}_3$  was formed with  $\text{PC}_{61}\text{BM}$  filled at grain boundaries. The bulk-heterojunction thin film presents superior film properties compared to  $\text{MAPbI}_3$  without  $\text{PC}_{61}\text{BM}$ .  $\text{PC}_{61}\text{BM}$  enhances bulk conductivity and charge mobility as well as mobility balance. Notably, current density–voltage curves show an identical shape regardless scan delay time from 0 to 500 ms without hysteresis. These results suggest advanced two-step fabrication method with various types of organic molecules may greatly enhance the overall film quality and light conversion efficiency.

### 3.3. Vapor-Induced Crystallization

Presently, the majority of hybrid perovskites are deposited using a solution process followed by thermal annealing. Because perovskite crystal is produced from precursor solutions in this approach, deposition conditions greatly influence the film quality. In the early stage of research, the effects from film coating methods and annealing conditions were unclear even while researchers were able to produce high-performance solar cells. Now, it is well-recognized that the crystallization process of hybrid perovskites is highly sensitive to the surrounding atmosphere during the deposition and annealing steps. Much research effort has been devoted to improve the quality of perovskite films by the manipulation of surrounding environment under solvent vapors including organic solvents, methylamine vapor, moisture, and even vacuum (see Table 3). In this subsection, we discuss how surrounding vapors modify the evolution of perovskite crystal and solar cell performance.

The most popular method for vapor treatment is solvent annealing, in which solvent vapor is introduced during thermal annealing under a closed system. Previously, solvent annealing methods have been widely used for polymer thin-film fabrication for optoelectronics.<sup>[169,170]</sup> Xiao et al. first reported the solvent annealing of hybrid perovskite for solar cells based on a two-step interdiffusion process.<sup>[135]</sup> Introduction of DMF vapor with high solubility for both  $\text{PbI}_2$  and MAI improves the mobility of precursor ions and results in a large grain growth

over the entire film thickness (Figure 8a,b). Transient photoluminescence of solvent annealed perovskite shows 7.2  $\mu$ s of carrier lifetime, which is four times higher than 1.7  $\mu$ s in a thermally annealed film (Figure 8c). Therefore, even 1  $\mu$ m thick MAPbI<sub>3</sub> can yield a PCE of 14%, which was previously limited due to the low carrier diffusion.<sup>[4,6]</sup> In addition, total trap density of solvent annealed MAPbI<sub>3</sub> is dramatically decreased down to the one-third of the thermal annealed counterpart (Figure 8d). The effect of solvent annealing was verified with a mixed halide perovskite, MAPbI<sub>3-x</sub>Cl<sub>x</sub> by Liu et al.<sup>[142]</sup> Combination of thermal annealing under nitrogen atmosphere followed by solvent annealing at 90 °C resulted in large crystal grains and reduced the overall resistance of the solar cell device, resulting in a considerable device efficiency improvement.

The effect from polar solvents, including, DMF, DMSO, GBL, H<sub>2</sub>O, and N<sub>2</sub>, on the solar cell performance fabricated by single-step spin-coating with anti-solvent dripping was investigated by Liu et al.<sup>[141]</sup> Polar solvents make perovskite grains large while it recrystallizes through the liquid–solid interface at the surface of the perovskite film. Defect density also strongly depends on the type of solvents. DMSO shows a high device performance

with low defect levels according to this report. Although the usual solvent annealing is accompanied by thermal treatment, a report by Yu et al. demonstrated a room-temperature solvent annealing method for highly efficient MAPbI<sub>3-x</sub>Cl<sub>x</sub> solar cells.<sup>[171]</sup> Ultrasmooth highly crystalline perovskite was attained by mixture solvent annealing in DMF and CB (1:20 v/v) atmosphere. While crystallization of MAPbI<sub>3-x</sub>Cl<sub>x</sub> requires thermal annealing for an order of few tens of minutes, mixed solvent annealing induces a fast crystallization within a few minutes even at room-temperature. Nevertheless, solvent annealing in general leads to higher device performances than the conventional thermal annealing with improved photogenerated charge carrier collection efficiencies. Exposure to organic solvent vapor during spin-coating also influences on the perovskite film formation. Lian et al. reported a solvent vapor modulated spin-coating process for a two-step interdiffusion process.<sup>[137]</sup> Interestingly, solvent vapor treatment during MAI spin-coating modifies the crystal orientation, which is not observed from conventional thermal and solvent annealing, suggesting a novel method for deposition parameter control.<sup>[112,172]</sup> This contributes to the reduction of the trap site and an increase in carrier

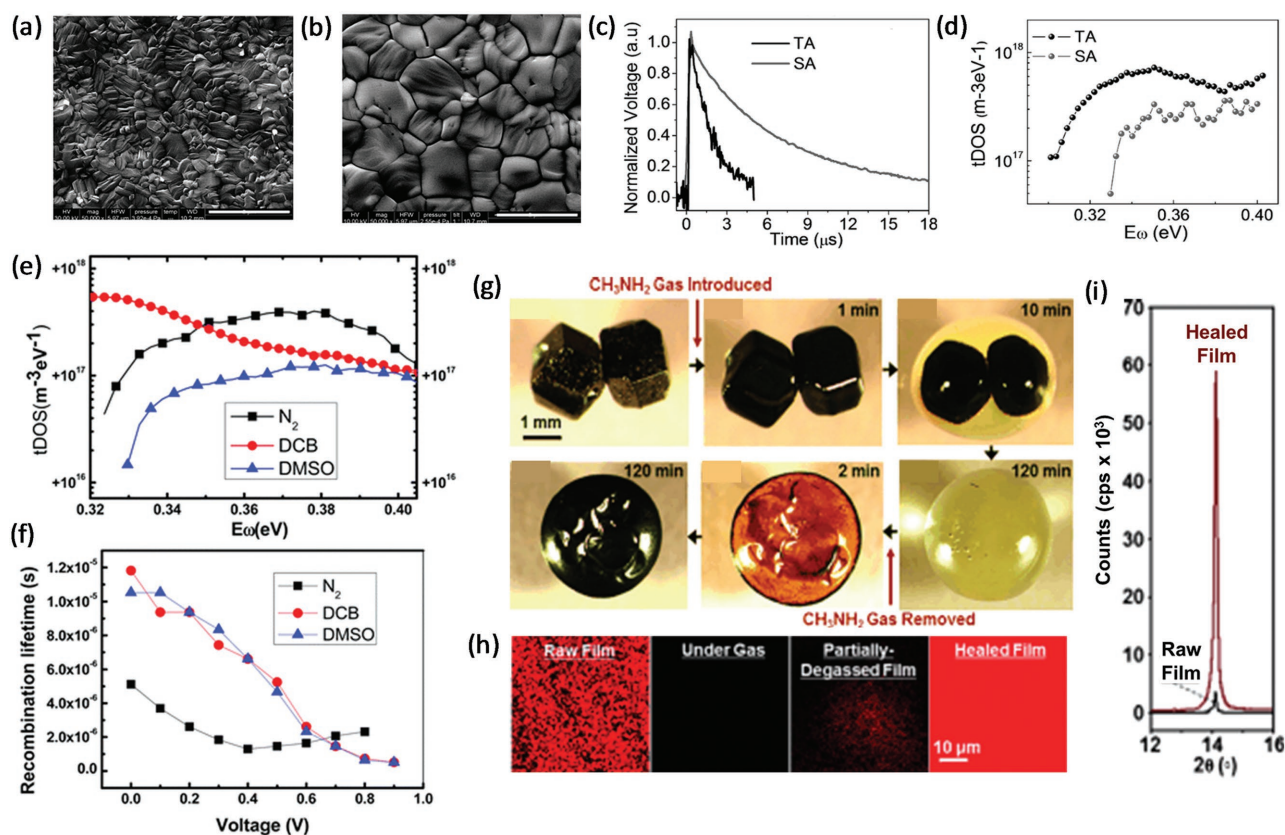


**Figure 8.** SEM images of MAPbI<sub>3</sub> perovskite films prepared by a) thermal annealing and b) solvent annealing. c) Trap density of states calculated from the thermal admittance spectroscopy measurement. d) Photovoltage decay under 0.3 Sun illumination measured by transient photovoltage. Panels (a–d) reproduced with permission.<sup>[135]</sup> Copyright 2014, Wiley. e) Trap-density of states measured from the thermal admittance spectroscopy measurements. f) Recombination lifetime of perovskite solar cells with the film treated by N<sub>2</sub>, DCB and DMSO vapors. Panels (e,f) reproduced with permission.<sup>[137]</sup> Copyright 2015, Royal Society of Chemistry. g) In situ optical microscopy of the morphology evolution of two touching MAPbI<sub>3</sub> perovskite crystals (same magnification) upon exposure to CH<sub>3</sub>NH<sub>2</sub> gas and CH<sub>3</sub>NH<sub>2</sub> degassing. h) In situ photoluminescence mapping of MAPbI<sub>3</sub> perovskite film during the CH<sub>3</sub>NH<sub>2</sub> induced defect healing; raw film, MAPbI<sub>3</sub>·xCH<sub>3</sub>NH<sub>2</sub> intermediate film, partially degassed film (1 s after removal of gas), and healed film (4 s after removal of gas). i) XRD patterns of MAPbI<sub>3</sub> (110) peaks from raw and defect-healed MAPbI<sub>3</sub> films. Panels (g–i) reproduced with permission.<sup>[143]</sup> Copyright 2016, Wiley.



lifetime; finally, PCE is improved compared with that prepared under pure nitrogen condition (Figure 8e,f).

Apart from solvent vapor treatment, Zhuo et al. demonstrated an interesting use of methylamine gas for the defect healing of MAPbI<sub>3</sub> perovskite.<sup>[143]</sup> When solution-processed MAPbI<sub>3</sub> with defects such as grain boundaries, pin-holes, and void, was exposed to methylamine gas, smoothening of the crystal surface, melting, and collapse of grains into liquid occurred. Subsequent removal of methylamine gas induces the recrystallization of perovskite with high film uniformity (Figure 8g). The temporal chemical reaction between MAPbI<sub>3</sub> and methylamine is responsible for the liquid phase formation of MAPbI<sub>3</sub>·xCH<sub>3</sub>NH<sub>2</sub>. Although other organic vapors such as ammonium, ethylamine, or n-butylamine were tested, neither significant morphology change nor complete recrystallization was observed. Photoluminescence mapping revealed how methylamine vapor influences the light-absorbing perovskite. While photoluminescence emission of as-coated films is completely quenched under methylamine vapor, emission is gradually recovered with the degassing of methylamine. Final perovskite films after defect healing were much denser with a complete photoluminescence emission over the entire measurement range (Figure 8h). XRD intensity also becomes much stronger (Figure 8i). Room-temperature-processed solar cells with and without methylammonium vapor healing exhibited a dramatic difference in efficiency of 15.1% and 5.7% respectively. A comparative study by Jiang et al. confirmed the effect of methylamine vapor.<sup>[140]</sup> In this report, methylammonium vapor was exposed during thermal annealing, demonstrating outstanding film quality and device performance compared to the conventional thermal and solvent annealing process. Furthermore, this method is useful for both mesoporous and planar architectures of perovskite solar cells.

Beyond organic solvent or molecule vapor systems, moisture in the atmosphere can be involved in the film formation of perovskites. Hybrid perovskites are generally known to be highly sensitive to moisture. They readily undergo the decomposition of crystal structure and the reduction in crystallinity, while losing hygroscopic organic components.<sup>[155,173]</sup> You et al. investigated the film quality enhancement by thermal annealing in a humid environment.<sup>[138]</sup> Different crystal growth behaviors are observed under different atmospheres, including nitrogen, oxygen, and ambient air with a relative humidity of 35%. Unexpectedly, thermal annealing in the ambient air showed a large grain size, high carrier mobility, and long carrier lifetime. This was explained by the hygroscopic nature of MAI that assists a moisture accumulation at grain boundaries inducing the merge of neighboring grains and recrystallization. Solar cells devices under 40% humidity showed the maximum PCE of 17.1% compared to 11.9% of the reference fabricated under 0% humidity. Significantly, relative humidity should be controlled near 40% for the best device performance as a higher humid condition may deteriorate the device performance.

Xie et al. reported vacuum-assisted thermal annealing methods using MAPbI<sub>3-x</sub>Cl<sub>x</sub> to avoid any vapor effect.<sup>[144]</sup> It is well-known that byproduct MAI gas is released during the formation of perovskite from MAI and PbCl<sub>2</sub> precursors.<sup>[174–176]</sup> In this report, it was clearly demonstrated that the control of relative rates of MAI release and MAI generation is a key

parameter for the production of high quality perovskite films without porosity. In the case of regular thermal annealing, a less dense film with larger pores was obtained due to the accumulation of MAI byproduct, as verified by XPS measurements. In contrast, vacuum-assisted thermal annealing enabled both the removal of MAI byproduct and the control of MAI generation by temperature control. When the release rate was higher than the generation rate, the best PCE of 14.5% was achieved based on the MAI residue-free homogeneous perovskite films. Concurrently, device stability was greatly improved without MAI residue.

### 3.4. Solvent-Mediated Crystallization

Organic–inorganic hybrid perovskites inherently bear strong ionic interactions between metal cations and halogen anions, which may lead to a hard controllability of film morphology due to the rapid reaction between precursor components. Crystallization of perovskite via intermediate phase is an attractive method to control the crystal growth and produce a dense and homogeneous perovskite layer (Table 3). The first attempt to exploit the intermediate phase was reported by Jeon et al. in 2014.<sup>[145]</sup> An intermediate phase, MAI-PbI<sub>2</sub>-DMSO, was attained with a specific film preparation method (Figure 5a). In this work, two critical points were 1) use of co-solvent of DMSO with GBL and 2) dripping of anti-solvent toluene during spin-coating process. The dripping process induces uniform frozen layer with the intermediated phase by washing out residual DMSO, which corresponds to an intercalated form of MAI and DMSO between the PbI<sub>2</sub> layers. Although most of the intermediate phase has DMSO, DMF molecule is also known to form an intermediate phase based on a similar mechanism with DMSO (Figure 9a).<sup>[146]</sup> A solid-state phase transformation from the intermediate phase by thermal annealing induces highly dense uniform MAPbI<sub>3-x</sub>Br<sub>x</sub> as well as MAPbI<sub>3</sub>. A certified PCE of 16.2% was achieved with a minimal hysteresis. Afterwards, Ahn et al. investigated the formation mechanism of the solvent-mediated intermediate phase.<sup>[39]</sup> DMSO was found to form adducts with PbI<sub>2</sub> and MAI, where DMSO and I<sup>-</sup> ions take the roles of the Lewis base while PbI<sub>2</sub> works as a Lewis acid, resulting in a PbI<sub>2</sub>·DMSO and MAI·PbI<sub>2</sub>·DMSO adducts. Charge carrier dynamics studied by photoinduced charge extraction with linearly increasing voltage (photo-CELIV) presents a notable increase in the charge carrier mobility via intermediate phase ( $3.9 \times 10^{-3} \text{ cm}^2 \text{ V}^{-1} \text{ s}^{-1}$ ) and slow recombination compared to that without DMSO ( $2.7 \times 10^{-3} \text{ cm}^2 \text{ V}^{-1} \text{ s}^{-1}$ ) (Figure 9b,c).<sup>[110,177]</sup> The solar cell devices demonstrate highly reproducible performance with the best PCE of 19.7%.

Solvent-mediated crystallization was also applied to the two-step fabrication of perovskite films. Yang et al. reported high performance FAPbI<sub>3</sub>-based perovskite solar cells by using an intramolecular exchange process (IEP) between the solvent = modulated PbI<sub>2</sub> layer and the FAI layer.<sup>[44]</sup> PbI<sub>2</sub>(DMSO) was synthesized as a framework for molecular exchange. Conventional two-step process using PbI<sub>2</sub> is based on the crystallization of PbI<sub>2</sub> from its surface toward the inside, where incomplete conversion of PbI<sub>2</sub> with a film thickness over 500 nm and uncontrolled surface roughness prohibit the formation of



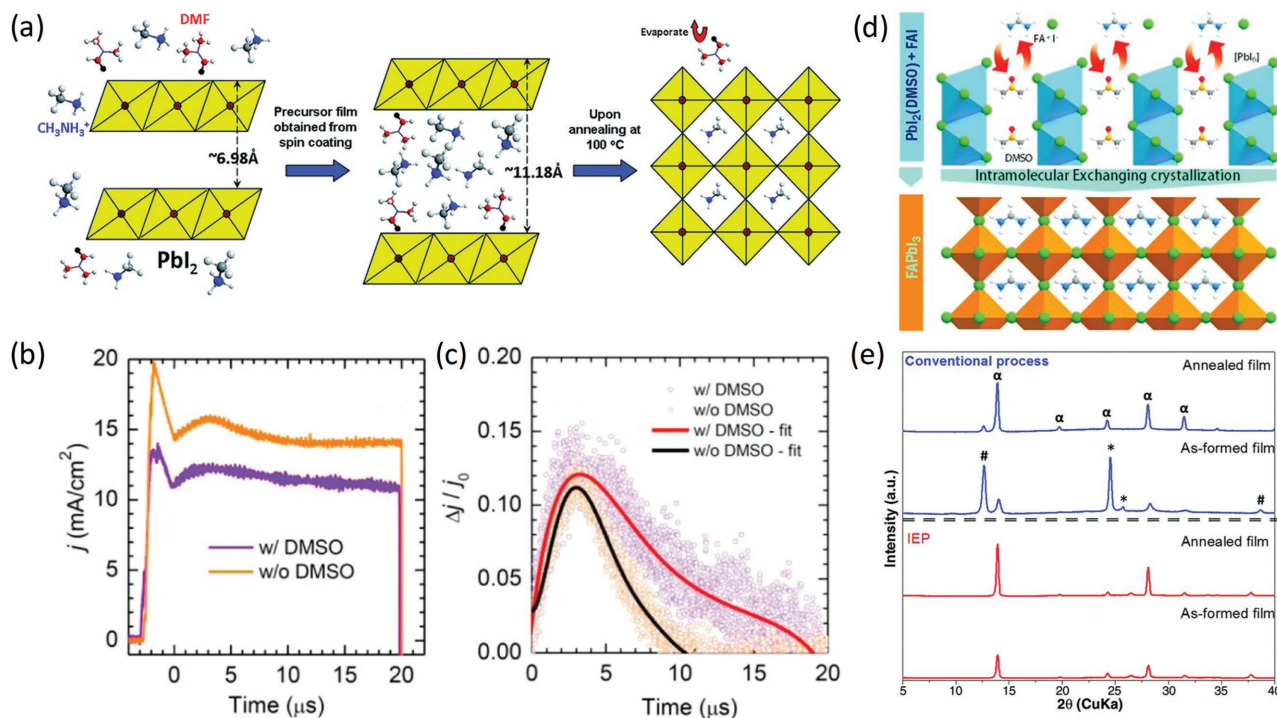


**Figure 9.** a) Schematic illustration of layered  $\text{PbI}_2$  parent lattice with an inter-planar distance of  $6.98 \text{ \AA}$  (left), the formation process of the DMF-induced intermediate phase and DMF molecules intercalate into the layered structure (center) and solvent-induced controllable crystallization of perovskite along with the release of DMF molecules (right). Reproduced with permission.<sup>[146]</sup> Copyright 2014, Royal Society of Chemistry. b) Transient photo-CELIV current of perovskite solar cell comprised of FTO/bl- $\text{Al}_2\text{O}_3$ /mp-TiO<sub>2</sub>/MAPbI<sub>3</sub>/spiro-MeOTAD/Ag with DMF or DMSO/DMF used as solvents for MAPbI<sub>3</sub>. c) Current peaks ( $\Delta j$ ) of photo-CELIV current transients normalized by their displacement current of capacitance ( $j_0$ ), respectively. Curves were fitted by polynomial fitting to compare charge extraction behavior of sample with or without DMSO. Panels (b,c) reproduced with permission.<sup>[39]</sup> Copyright 2015, American Chemical Society. d) Schematic illustration of FAPbI<sub>3</sub> perovskite crystallization involving the direct intramolecular exchange (IEP) of DMSO molecules intercalated in  $\text{PbI}_2$  with formamidinium iodide (FAI). The DMSO molecules are intercalated between edge-sharing  $[\text{PbI}_6]$  octahedral layers. e) XRD patterns of as formed and annealed film for FAPbI<sub>3</sub>-based layers formed by IEP (red line) and conventional (blue line) process. Symbols a, #, and \* denote the identified diffraction peaks corresponding to the FAPbI<sub>3</sub> perovskite phase,  $\text{PbI}_2$ , and FAI, respectively. Panels (d,e) Reproduced with permission.<sup>[44]</sup> Copyright 2015, The American Association for the Advancement of Science.

highly crystalline perovskite films.<sup>[109,178]</sup> In contrast, sequential deposition of  $\text{PbI}_2(\text{DMSO})$  and FAI raises an immediate phase transformation to perovskite (Figure 9d). XRD patterns show (111) direction oriented perovskite compared to conventional methods (Figure 9e). The average PCE of solar cells without and with solvent-modified  $\text{PbI}_2$  were 15% and 19.5%, respectively, with the certified best PCE of 20.1%

### 3.5. Laser Crystallization

As summarized above, many different innovative approaches have been introduced for the high performance organic–inorganic perovskite solar cells. While research demand for the commercialization of perovskite solar cell is growing, large-area film deposition methods with high speed and process continuity are becoming more and more significant, as mentioned in the Section 2.3. Unfortunately, the majority of crystallization processes rely on batch-type annealing conditions, which is an inherent bottleneck for the realization large-area, high-throughput device fabrication. A robust crystallization method that is available for large area/flexible devices at low-temperature with process continuity is highly desired for eventual commercial success.

Laser crystallization is a promising candidate for material processing and is highly attractive particularly for industry because of its intrinsic competitiveness such as low temperature continuous processing, compatibility with flexible device process, scalability, and area selectivity. Effective phase transitions of inorganic materials (amorphous silicon, metal oxide, and other inorganic materials) are well established for localized areas as well as large areas with high-energy laser beams from excimer laser sources, with typical wavelengths in UV regime. Nevertheless, laser crystallization of emerging optoelectronic materials has not been explored much. Synergetic effects are expected from laser crystallization of organic–inorganic hybrid materials in terms of process and device performance: 1) effective crystal growth by rapid heating/cooling, 2) continuous and fast crystallization, and 3) compatibility with large area and/or flexible substrates. These benefits coincide with the demands for next-generation solar cells.

Realization of laser crystallization is, however, challenging because organic–inorganic halide perovskites are multi-component systems containing both organic and inorganic salts. Organic materials are not particularly sustainable among the two disparate components under a high-energy laser beam irradiation. The key point is to grow and control the crystallites

of halide perovskites while maintaining stable undamaged crystal structures. Loss of organic cations degrades the stability of crystal structure and optoelectronic properties. Furthermore, transparent conductive oxide (TCO) and a charge transport layer underlying the perovskite active layer in the device structure can also be degraded by a high-energy laser beam. Overall, soft laser crystallization of organic–inorganic multi-component system is desirable for the upcoming hybrid-type optoelectronics.

In 2016, our research group demonstrated laser-crystallization of MAPbI<sub>3</sub> perovskite solar cells.<sup>[147]</sup> Interestingly, near infrared laser irradiation induces an instantaneous transformation of the as-deposited film with intermediate phase to perovskite crystallites (**Figure 10a**). Perovskite morphology and crystallinity are widely controllable along with the laser irradiation conditions, such as power density and scan rate (**Figure 10b,c**). Photogenerated charge carrier lifetime varies with laser power intensity, which determines total energy applied to the perovskite precursor thin-film for crystallization (**Figure 10d**). Photothermal heating, photon-to-phonon conversion assisted by a conductive interfacial layer, is known to be critical for the phase transition in a multilayered device architecture. Average solar cell efficiencies of laser and controlled thermally annealed perovskites are 12% and 10.4%, respectively. Interestingly, a low energy NIR laser source enables the effective laser crystallization of perovskite on a flexible polymer substrate with a high scan speed (61 m h<sup>-1</sup>)

and attains 8% efficiency. Synergetic integration of laser crystallization with large area solution deposition methods such as spray-coating,<sup>[102]</sup> slot-die coating,<sup>[101]</sup> etc. is highly anticipated for the further progress of flexible roll-to-roll device fabrication.

## 4. Crystallization Methods for Perovskite Light Emitters

### 4.1. Thin-Film Engineering

Confining excitons electrically or physically is an essential requirement for highly efficient LEDs because efficient radiative recombination of excitons is crucial for light emission. An interesting attempt to confine excitons in 3D perovskites was suggested by Tan et al. in 2014.<sup>[26]</sup> In order to overcome the low  $E_b$ , spatial confinement via ultimate thin perovskite film sandwiched between large band-gap transport layers was used for green, red, and near infrared LEDs with 15 to 20 nm thick MAPbBr<sub>3</sub> or MAPbI<sub>3-x</sub>Cl<sub>x</sub> perovskite (**Figure 11a**). The spatial exciton confinement leads a bright green electroluminescence at 517 nm with the luminance of 364 cd m<sup>-2</sup> at a current density of 123 mA cm<sup>-2</sup>, with external quantum efficiencies of 0.1% (**Figure 11b**). Near infrared emitting MAPbI<sub>3-x</sub>Cl<sub>x</sub> had a photoluminescence quantum yield of 26% and electroluminescence with radiance of 13.2 W sr<sup>-1</sup> m<sup>-2</sup> at a current density

of 363 mA cm<sup>-2</sup>. In addition, the external and internal quantum yields were estimated to be 0.76% and 3.4%, respectively. These results imply that spatial confinement induces a high rate of electron/hole capture and radiative recombination, and reabsorption loss is minimized because of the very thin emission layer thickness. Interestingly, EQE increases with voltage and current density (**Figure 11c,d**), indicating that a high charge density is required in the emission for efficient radiative recombination. However, these methods would not be the fundamental solutions to overcome small  $E_b$  of 3D perovskites. The thin perovskite layer possibly introduces a shunting path during device fabrication. Yaffe et al. reported the mechanical exfoliation of a 2D perovskite layer as a single unit cell with the thickness of 2.4 nm.<sup>[179]</sup> The 2D perovskite nanosheet exhibited a strong light–matter interaction with an optical absorption as high as 25% at the main excitonic resonance, as well as bright photoluminescence with an  $E_b$  of 490 meV due to the change in the dielectric environment of the ultrathin film compared to bulk. Moreover, thermal induced phase transition was suppressed in this form. Although practical application has not been demonstrated, nevertheless, this would be promising candidate for future light emission of perovskites (**Table 4**).

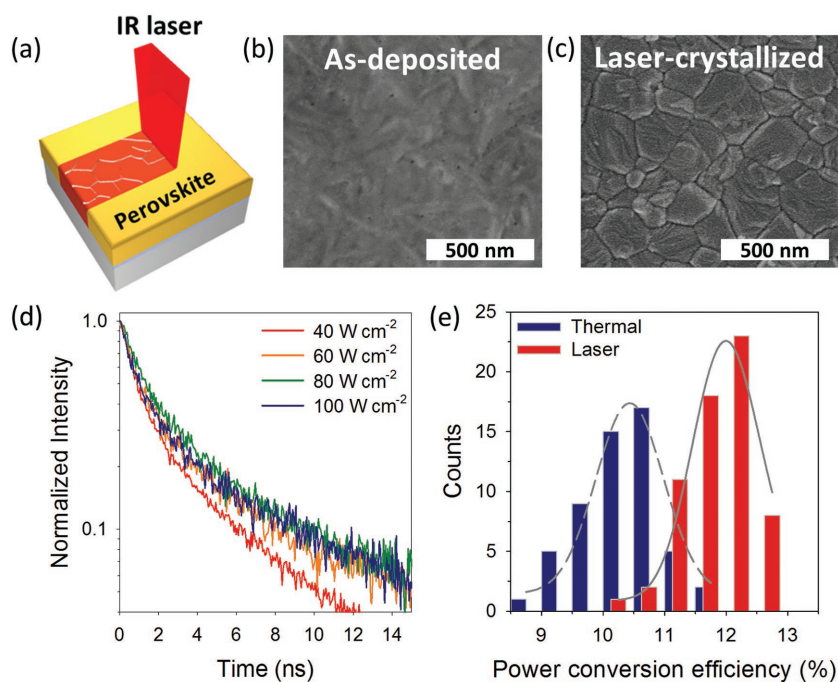


**Figure 10.** Laser crystallization of organic-inorganic perovskite solar cells. a) Schematic illustration of laser crystallization by near-infrared laser beam. Near-infrared laser beam with a wavelength of 1064 nm is irradiated onto MAPbI<sub>3</sub> precursor coated surface with stage translation. SEM images of b) as-deposited and c) laser-crystallized MAPbI<sub>3</sub> perovskite films. d) Time resolved photoluminescence along with laser beam power density. e) Power conversion efficiency distribution of perovskite solar cells based on conventional thermal annealing (100 °C for 5 min) and laser crystallization (80 W cm<sup>-2</sup> and 0.1 mm s<sup>-1</sup>). Reproduced with permission.<sup>[147]</sup> Copyright 2016, American Chemical Society.

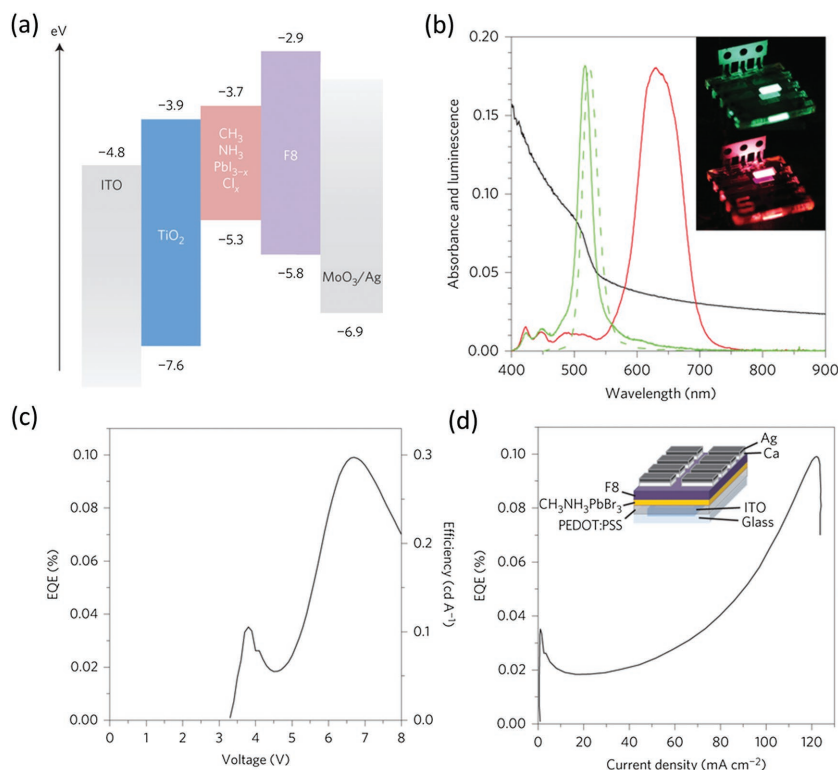


**Figure 11.** a) Energy-level diagram of infrared PeLED, showing conduction and valence band levels with respect to vacuum. b) Absorbance (black), normalized electroluminescence (green, solid) and normalized photoluminescence (green, dashed) spectra of MAPbBr<sub>3</sub> perovskite. Normalized electroluminescence spectrum of MAPbBr<sub>2</sub>I mixed halide perovskite is shown in red. Inset image: uniform green and red electroluminescence from ITO/PEDOT:PSS/MAPbBr<sub>3</sub>/F8/Ca/Ag and ITO/PEDOT:PSS/MAPbBr<sub>2</sub>I/F8/Ca/Ag PeLEDs, respectively. c) EQE versus voltage characteristics of the green PeLED. d) EQE versus current density of the green PeLED. Inset: Green PeLED device structure. Reproduced with permission.<sup>[47]</sup> Copyright 2014, Nature Publishing Group.

#### 4.2. Solvent Treatments for Nanoscale Crystal Pinning

Conventional spin coating of light-emitting MAPbBr<sub>3</sub> perovskite usually results in a poor surface coverage and rough, non-uniform surfaces due to the formation of large size cuboids (Figure 12a).<sup>[62]</sup> As mentioned previously, perovskite films for light harvesting should be homogeneous and dense with a large grain size (few hundred nanometer to millimeter scale) to achieve efficient exciton dissociation at room temperature and long charge carrier diffusion.<sup>[120]</sup> In contrast, the eventual goal of perovskite LEDs is the homogeneous and dense film formation that can spatially confine excitons for radiative recombination. In 2015, Cho et al. reported a nanocrystal pinning process (NCP) that uses volatile anti-solvent without (S-NCP) and with dissolved electron transport material (A-NCP) during the spinning of MAPbBr<sub>3</sub>.<sup>[14]</sup> The fabricated PeLED demonstrated excellent current efficiencies from 21.4 to 42.9 cd A<sup>-1</sup> with a glass/self-organized conducting polymer (SOC)/MAPbBr<sub>3</sub>/TPBi/LiF/Al device configuration. The high efficiency was principally attributed to the well-controlled film morphology. NCP leads to homogeneous perovskite films with full surface coverage and scattered cuboidal microcrystalline growth changes into well-interconnected nanocrystals growth with relatively

small grain size. A-NCP shows much smaller grains compared with S-NCP (Figure 12b,c). The entire film thickness of perovskite emitting layer was around 400 nm (Figure 12d). Consequently, the average grain size and exciton diffusion length reached 99 and 67 nm, respectively. This signifies that spatial confinement of electrons and holes in each grain leads to the shorter diffusion length than grain size. Current efficiency and luminance along with voltage clearly show high efficiency and luminance with A-NCP, which represent maximum EQE of 8.53% (Figure 12e,f). Nevertheless, it is necessary to gain an accurate understanding of the phenomenon and unrevealed mechanism of the A-NCP process for highly efficiency PeLEDs. A modified NCP process using an anti-solvent and solvent mixture for efficient PeLED was demonstrated by Jiao et al. in 2016.<sup>[187]</sup> A mixture of chlorobenzene and DMF was used to obtain efficiency improvement and device stability. Using this approach, a luminance of 3868 cd m<sup>-2</sup> and current efficiency of 0.54 cd A<sup>-1</sup> was achieved, which is 20-fold improvement compared to the control devices.

While the generation of uncoordinated metallic Pb increases non-radiative recombination rate of MAPbBr<sub>3</sub> films regardless of solvent engineering, it is essential to suppress the formation of metallic Pb to maximize the effects of nanocrystal pinning.<sup>[14,196]</sup> The high efficiency PeLEDs were demonstrated on the basis of effectively eliminating of exciton quenching sites, metallic Pb species, using a modified emitting layer with stoichiometry unbalance.<sup>[47,187]</sup> Delicate control of the MABr:PbBr<sub>2</sub> molar ratio from 1:1 to 1.05:1 constrains to form metallic Pb atom and, as a result, current efficiency of PeLED varied from 0.183 to 21.4 cd A<sup>-1</sup>.<sup>[14]</sup> Excess MABr prevents the formation of metallic Pb atoms and suppresses exciton quenching and also reduces the charge injection barrier because of the absence of the PbBr<sub>2</sub> passivation layer with a large band gap.<sup>[197]</sup> In addition, the metal species released from the indium tin oxide (ITO) electrode can be a strong exciton quencher in PeLEDs, which have long exciton diffusion lengths. Therefore, use of graphene as an ITO-free electrode resulted in a significant increase in device efficiencies from 10.8 to 18 cd A<sup>-1</sup>.<sup>[198]</sup>

#### 4.3. Additive-Modulated Crystallization

Uniform surface emission is an essential aspect of planar lighting sources. The cuboidal growth nature of MAPbBr<sub>3</sub> perovskite prepared by simple spin-coating, however, commonly leads to an island-like morphology with poor surface coverage, resulting in a starlight-like emission rather than the reliable uniform emission (Figure 13a). A report from Li et al. investigated the blends of MAPbBr<sub>3</sub> perovskite and polyimide



**Table 4.** Summary of PeLED performance with various crystallization methods.

Method	Morphology	Device structure	CE [cd A <sup>-1</sup> ]	EQE [%]	$L_{\max}$ [cd cm <sup>-2</sup> , Wsr m <sup>-2</sup> *)	$V_{th}$ [V]	EL [nm]	FWHM [nm]	Ref.
<b>Thin-film engineering</b>	thin film	ITO/PEDOT:PSS/MAPbBr <sub>3</sub> /F8/Ca/Ag	0.3	0.1	364	3.3	517	–	[26]
<b>Interfacial engineering</b>	thin film	ITO/MAPbI <sub>3-n</sub> Cl <sub>n</sub> /Spiro-OMETAD/Au	–	0.48	7.1*	1.45	405	42	[180]
	thin film	ITO/PEDOT:PSS/MAPbBr <sub>3</sub> /ZnO/Ca/Ag	21	–	550	2	–	–	[181]
	thin film	ITO/Buf-HIL/MAPbBr <sub>3</sub> /TPBi/LiF/Al	0.577	0.125	417	4	543	20	[61]
	thin film	ITO/c-TiO <sub>2</sub> /EA/MAPbBr <sub>3</sub> /SPB-02T/MoO <sub>3</sub> /Au	0.22	0.051	544	≈2.3	–	–	[27]
	thin film	ITO/ZnO-PEI/MAPbBr <sub>3</sub> /TFB/MoO <sub>3</sub> /Au	–	0.8	20000	2.8	532	22	[182]
	thin film	ITO/ZnO-PEI/MAPbI <sub>3-n</sub> Cl <sub>n</sub> /TFB/MoO <sub>3</sub> /Au	–	3.5	28*	2.2	768	37	[182]
<b>Additives</b>	thin film	ITO/MAPbBr <sub>3</sub> -PEO/In/Ga	0.38	0.083	4064	2.9	532	23	[183]
	thin film	ITO/MAPbBr <sub>3</sub> -PEO/AgNWs	4.91	1.1	21014	2.6	–	–	[184]
	thin film	ITO/PEDOT:PSS/MAPbBr <sub>3</sub> -PIP/F8/Ca/Ag	–	1.2	200	≈3.1	534	19	[185]
	thin film	ITO/Poly-TPD/BAI:MAPbI <sub>3</sub> /TPBi/LiF/Al	0.09	10.4	–	–	748	–	[28]
	thin film	ITO/PVK/BAI:MAPbBr <sub>3</sub> /TPBi/LiF/Al	17.1	9.3	2900	–	513	–	[28]
<b>Solvent treatment</b>	thin film	ITO/PEDOT:PSS/MAPbBr <sub>3</sub> /SPB-02T/LiF/Ag	0.43	0.1	3490	≈2.1	540	–	[186]
	thin film	ITO/PEDOT:PSS/MAPbBr <sub>3</sub> /Bphen/LiF/Ag	0.54	0.13	3846	3.2	528	21	[187]
	thin film	Glass/SOCP/MAPbBr <sub>3</sub> /TPBi/LiF/Al	42.9	8.53	15000	4	–	–	[14]
<b>Inorganic substitution</b>	thin film	ITO/PEDOT:PSS/CsPbBr <sub>3</sub> /F8/Ca/Ag	0.035	0.008	407	3	527	18	[188]
<b>Nanostructuring</b>	nano plate	ITO/PEDOT:PSS/MAPbBr <sub>3</sub> /PVK:PBD/BCP/LiF/Al	–	0.48	10590	3.8	–	20	[189]
	nano plate	ITO/PEDOT:PSS/FAPbBr <sub>3</sub> :LiCF <sub>3</sub> SO <sub>3</sub> :TMPE/Al	–	–	1.3	11–12	–	–	[190]
	QD	ITO/PEDOT:PSS/PVK/FAPbBr <sub>3</sub> /TPBi/LiF-Al	0.43	0.12	946	4.2	514	23	[191]
	QD	ITO/PEDOT:PSS/PVK/CsPb(Cl/Br) <sub>3</sub> /TPBi/LiF-Al	0.14	0.07	742	5.1	452	20	[191]
	QD	ITO/PEDOT:PSS/PVK/CsPb(Br/I) <sub>3</sub> /TPBi/LiF-Al	0.08	0.09	528	4.6	586	23	[191]
	thin film	ITO/PEDOT:PSS/CsPbBr <sub>3</sub> /B3PYMPM/CsCO <sub>3</sub> /Al	0.57	0.15	7276	2.8	524	18	[192]
	nano particle	ITO/PEDOT:PSS/Poly-TPD:PFI/CsPbBr <sub>3</sub> /TPBi/LiF/Al	0.19	0.06	1377	3.5	516	18	[13]
	nano particle	ITO/ZnO/CsPbBr <sub>3</sub> /TFB/MoO <sub>3</sub> /Ag	0.28	0.19	2335	2.8	523	19	[48]
	nano particle	ITO/ZnO/CsPbI <sub>3</sub> /TFB/MoO <sub>3</sub> /Ag	–	5.7	206	–	698	31	[48]
	nano particle	ITO/ZnO/CsPbI <sub>3-n</sub> Br <sub>n</sub> /TFB/MoO <sub>3</sub> /Ag	–	1.4	1559	–	619	29	[48]
	nano particle	ITO/ZnO/CsPbBr <sub>n</sub> Cl <sub>n</sub> /TFB/MoO <sub>3</sub> /Ag	–	0.0074	8.7	–	480	17	[48]
<b>Low dimension</b>	thin film	ITO/TiO <sub>2</sub> /PEA <sub>2</sub> MA <sub>n-1</sub> Pb <sub>n</sub> I <sub>3n+1</sub> /F8/MoO <sub>3</sub> /Au	–	8.8	80*	3.8	–	–	[16]
	thin film	ITO/PEDOT:PSS/poly-TPD/BA <sub>2</sub> MA <sub>2</sub> Pb <sub>3</sub> I <sub>10</sub> /TPBi/LiF/Al	0.1	2.29	214	2.7	700	52	[193]
	thin film	ITO/PEDOT:PSS/poly-TPD/BA <sub>2</sub> MA <sub>4</sub> Pb <sub>5</sub> Br <sub>16</sub> /TPBi/LiF/Al	3.48	1.01	2246	3.3	523	24	[193]
	thin film	ITO/PEDOT:PSS/poly-TPD/BA <sub>2</sub> MA <sub>2</sub> Pb <sub>3</sub> Br <sub>7</sub> Cl <sub>3</sub> /TPBi/LiF/Al	0.006	0.01	21	5.2	468	28	[193]
	thin film	ITO/Buf-HIL/PEA <sub>2</sub> MA <sub>n-1</sub> Pb <sub>n</sub> Br <sub>3n+1</sub> /TPBi/LiF/Al	4.9	–	2935	3	520	20	[32]
	thin film	ITO/PEA <sub>2</sub> MA <sub>2</sub> PbI <sub>4</sub> /OXD7/MgAg	2	–	>10 000	–	520	10	[194]
<b>Lower dimension/ nanostructuring</b>	nano particle	ITO/PEDOT:PSS/poly-TPD/(OA) <sub>2</sub> (MA) <sub>2</sub> Pb <sub>3</sub> Br <sub>10</sub> /TmPyPB/LiF/Al	1.43	0.53	704	3.5	508	27	[15]
	nano plate	ITO/PEDOT:PSS/(PEA) <sub>2</sub> PbBr <sub>4</sub> /TPBi/Ca/Al	–	0.038	–	2.5	410	–	[195]

MA: methylamine, FA: formamidinium, PEA: phenylethylamine, BA: butylamine, OA: octylamine; F8: poly(9,9-dioctylfluorene), Spiro-OMETAD: 2,2',7,7'-tetrakis(N,N-di-p-methoxyphenylamine)-9,9-spiro-bi-fluorene, Buf-HIL: buffered hole-injection layer, SPB-02T: spirobifluorene-triphenylamine conjugated copolymer, TFB: poly(9,9-dioctyl-fluorene-co-N-(4-butylphenyl)diphenylamine), PEO: poly(ethylene oxide), PIP: polyimide polymer, Bphen: batho-henanthroline, PBD: 2-(4-biphenyl)-5-phenyl-1,3,4-oxadiazole, TMPE: trimethylolpropane ethoxylate, B3PYMPM: 4,6-Bis(3,5-di(pyridin-3-yl)phenyl)-2-methylpyrimidine, TmPyP: 1,3,5-Tri(m-pyridin-3-ylphenyl)benzene, BCP: bathocuproine; TPBi: 2,2',2''-(1,3,5-benzinetriyl)-tris(1-phenyl-1-H-benzimidazole), OXD7: oxadiazole derivative, TPD: N,N'-bis(3-methylphenyl)-N,N'-diphenylbenzidine, PVK: poly(9-vinylcarbazole).



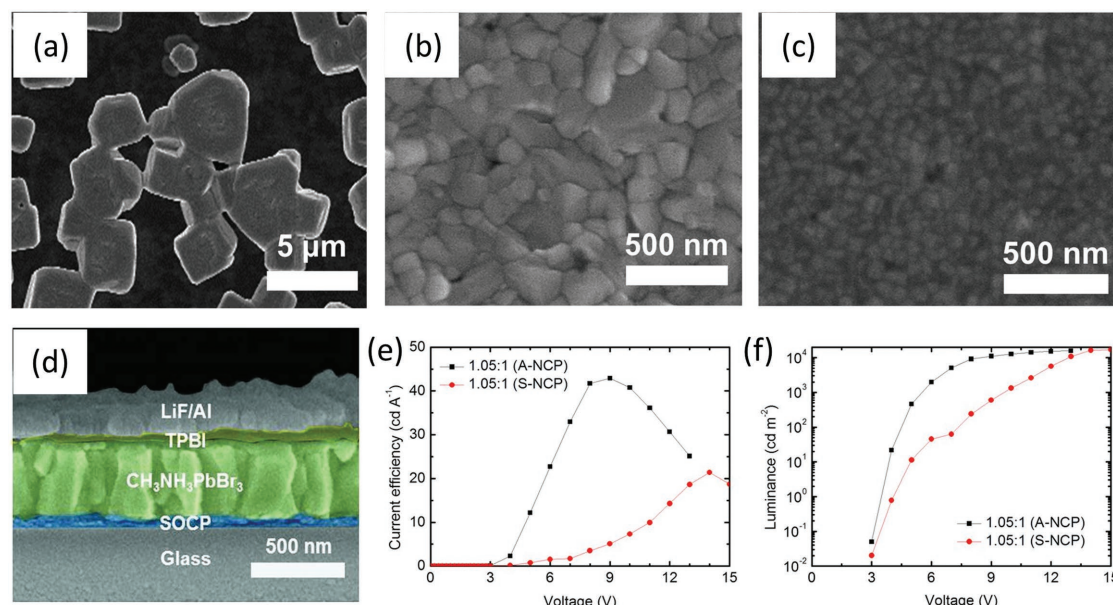


**Figure 12.** SEM images MAPbBr<sub>3</sub> layers and PeLED characteristics with solvent treatment (A-NCP, S-NCP). SEM images of MAPbBr<sub>3</sub> layers of a) MABr:PbBr<sub>2</sub> without NCP, b) with S-NCP, and c) with A-NCP. d) Cross-sectional structure of PeLEDs. e) Current efficiency and f) luminance of PeLEDs based on A-NCP and MAPbBr<sub>3</sub> nanograin emission layers. Reproduced with permission.<sup>[14]</sup> Copyright 2015, The American Association for the Advancement of Science.

precursor dielectric (PIP) to form uniform thin films.<sup>[185]</sup> Notably, the blend films show a morphology like the embedment of nanocrystal perovskites in a uniform PIP matrix without pinholes (Figure 13b). Because of the reduction of non-radiative recombination and efficient charge blocking of the polymer matrix, PeLED based on 1:2 ratio of PIP:MAPbBr<sub>3</sub> blend films yield 200 cd m<sup>-2</sup> at current density of 3.1 mA cm<sup>-2</sup> and maximum 1.2% of EQE, which varies along with the ration of PIP (Figure 13c).

Depending on the electrical property of blending polymers, the perovskite and polymers blends contribute to the development of single layer PeLED without any transport layers sandwiching the perovskite layer. Li et al. reported a light-emitting single layer using MAPbBr<sub>3</sub> and poly(ethyleneoxide) (PEO) with device architecture ITO/MAPbBr<sub>3</sub>-PEO composite/In/Ga or Au.<sup>[183]</sup> Inclusion of the PEO results in a homogeneous film formation with full surface coverage, as the case of MAPbBr<sub>3</sub>-PIP blends (Figure 13c–e). More significantly, PEO is known to be a good ionic conductor, induces ionic migration in the blended films, and consequently forms a p-i-n homojunction (Figure 13g). In contrast, poor ionic conductors and insulators such as PVDF (polyvinylidene fluoride) and PS (polystyrene) have an insulating nature with 50 000 times lower conductivity than PEO. The PeLED with PEO exhibits maximum current efficiency of 0.74 cd A<sup>-1</sup> with a low turn on voltage and maximum luminance of 4064 cd m<sup>-2</sup>, which is comparable to the previously reported multilayer-based PeLED, where the pure perovskite emitter shows a maximum current efficiency of 0.09 cd A<sup>-1</sup> (Figure 13h). Process flexibility of the blend films offers an opportunity to fabricate fully printable PeLEDs. Bade et al. demonstrated printed PeLED using MAPbBr<sub>3</sub> and PEO blends on both rigid ITO/glass and flexible carbon nanotubes (CNTs)/polymer substrates.<sup>[184]</sup>

The blend films were deposited using doctor-blade coating with silver nanowire cathodes. Typical printing process under ambient air produced PeLEDs with a high luminance of 20 000 cd m<sup>-2</sup> and current efficiency of 4.91 cd A<sup>-1</sup> with an EQE of 1.1%.

Yu et al. achieved uniform MAPbBr<sub>3</sub> perovskite films by introducing HBr into precursor solution.<sup>[186]</sup> Films from MAPbBr<sub>3</sub> dissolved in DMF only show cube-shaped crystals with poor emission characteristics (Figure 13i). As film coverage is increased with HBr composition, 6 vol% shows full coverage and smooth surface without cube-shaped crystals resulting in a uniform surface green emission (Figure 13j). The PeLED with 6 vol% HBr in the DMF exhibited the maximum luminance of 3490 cd m<sup>-2</sup> and maximum current efficiency levels as high as 0.43 cd A<sup>-1</sup> at 4.3 V (Table 4). Recently, Xiao et al. revealed that large-group ammonium halide additive, n-butylammonium halide (BAI and BABr), suppresses the growth of 3D perovskite grains and produces small-sized perovskite crystallites as small as 10 nm. Thereby, the EQE of conventional MAPbI<sub>3</sub> and MAPbBr<sub>3</sub> PeLEDs exceeded 10% and 9%, respectively.<sup>[28]</sup>

In 2016, Wei et al. reported very bright and durable cesium lead bromide (CsPbBr<sub>3</sub>) PeLEDs using single-step spin-coating of CsPbBr<sub>3</sub> and CsBr additives in DMSO.<sup>[192]</sup> CsBr additive promotes (110) the directional growth of crystals into smooth microplates with an enhanced photoluminescence intensity and carrier lifetime. PeLEDs show a high luminance of 7276 cd m<sup>-2</sup> and high color purity with a full width at half maximum of only 18 nm. Furthermore, the as-fabricated LEDs reveal an outstanding ambient stability with a decent luminance output (>100 cd m<sup>-2</sup>, steady increase without any degradation trend) for at least 15 h under a constant driving current density. This was attributed to thermal stability and resistance to joule heating during the device operation.

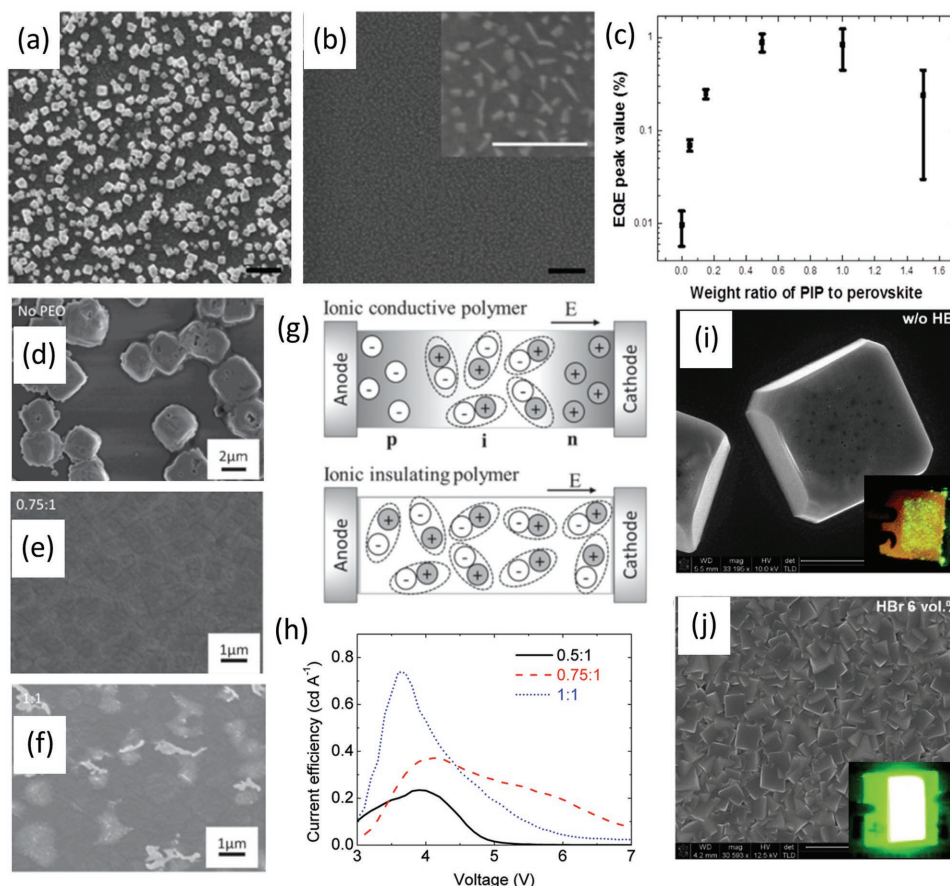


**Figure 13.** SEM images of a) perovskite only and b)  $\frac{1}{2}$  PIP/perovskite on PEDOT:PSS coated silicon. c) External quantum efficiency peak value versus MAPbBr<sub>3</sub>/PIP weight ratio. Panels (a–c) reproduced with permission.<sup>[185]</sup> Copyright 2015, American Chemical Society. SEM images of d) bromide perovskite only, and bromide perovskite/PEO composition with PEO/perovskite ratio e) 0.75:1 and f) 1:1. g) Schematic illustration of ion migration under an applied electric field in the MAPbBr<sub>3</sub>/polymer composite with ionic conductive polymer (top) or ionic insulating polymer (bottom). Cations and anions will be transported by the ionic conductive polymer and accumulate close to the electrodes, resulting in formation of p-i-n junction. No junction formation will occur when an ionic insulating polymer is used. h) Current efficiency versus voltage characteristics of the single-layer MAPbBr<sub>3</sub>/PEO LEDs with 0.5:1 (black solid line), 0.75:1 (red dashed line), and 1:1 (blue dots) PEO/LEDs ratios. Panels (d–h) Reproduced with permission.<sup>[183]</sup> Copyright 2015, Wiley. SEM images of i) pristine MAPbBr<sub>3</sub> perovskite j) with HBr 6 vol.% (inset shows EL from perovskite LED with 1 cm<sup>2</sup> active area.) Panels (i,j) reproduced with permission.<sup>[186]</sup> Copyright 2016, Royal Society of Chemistry.

#### 4.4. Nanostructured Perovskite Crystals

A considerable merit of nanostructuring is the substantial variation in optoelectronic properties. For instance, the low  $E_b$  of MAPbBr<sub>3</sub> microcrystalline (84 meV) can be greatly enhanced with nanoparticle formation (320 meV) (Table 2). Nanostructured 3D perovskite crystals can be formed regardless of components and composition of perovskites by managing synthetic methodology.<sup>[13,179,189,191,192,199–202]</sup> Nanostructured perovskites show further improved photoluminescence and long recombination lifetime by surface passivation effects from ligand stabilization (Table 4). The key benefits of nanostructured perovskites are  $E_b$  increase and fast interfacial charge transport, which enables highly efficient lead halide perovskite quantum dot LEDs.<sup>[203]</sup>

The first synthesis of MAPbBr<sub>3</sub> perovskite nanoparticles using nanotemplates was reported by Schmidt et al.<sup>[204]</sup> These nanoparticles can be maintained as stable in the solid state as well as in the concentrated solutions for more than three

months. Colloidal solution and the spin-cast thin film emit light with narrow bandwidth in the visible spectrum with a high photoluminescence quantum yield (20%). The nanoparticles capped with by n-octylamine ligand exhibited high photoluminescence quantum yields (50–70%).<sup>[205]</sup> Furthermore, the nanoparticles exhibited a high luminescence and photostability in toluene dispersion.<sup>[199]</sup> Conventional semiconductor type quantum dots exhibit a broadening of the luminescence spectrum due to the non-negligible distribution of the particle size. In contrast, inorganic cation substituted in the place of organic cation, CsPbBr<sub>3</sub> nanoparticles show high stability, and no color broadening effect compared with MAPbBr<sub>3</sub>. CsPbBr<sub>3</sub> has a high quantum yield of 90% with a negligible self-absorption and Förster resonance energy transfer, but also no photoluminescence peak position changes even under temperature variation.<sup>[202]</sup> Nonetheless, the PeLED performance based on nanoparticles is still lower than conventional thin-film-based PeLED. This is primarily attributed to the lack of proper perovskite film preparation methods for complete surface coverage.

In 2016, Liang et al. reported layered lead bromide perovskite nanoplates using 2-phenylethylammonium ( $\text{C}_6\text{H}_5\text{CH}_2\text{CH}_2\text{NH}_3^+$ , PEA) lead bromide,  $(\text{PEA})_2\text{PbBr}_4$ .<sup>[195]</sup> The nanoplate-based thin film was prepared using DMF solvent vapor annealing from a simply spin-coated  $(\text{PEA})_2\text{PbBr}_4$  film. as the as-deposited film had a homogeneous polycrystalline morphology (Figure 14a), while microsized nanoplates were observed after the annealing of an as-deposited thin film under DMF atmosphere (Figure 14b). PeLEDs with  $(\text{PEA})_2\text{PbBr}_4$  emit violet of 410 nm with a narrow bandwidth of 14 nm due to the high band-gap compared with conventional 3D MAPbBr<sub>3</sub>. The EQE of the PeLEDs based on the thin film and nanoplates show 0.002 and 0.04%, respectively (Figure 14c). Despite the 20 times increase in EQE by synergetic effects of 2D and nanoplates, full film coverage should be addressed to minimize the current loss.

Nearly complete nanocrystal film coverage was demonstrated by Li et al. in 2016<sup>[48]</sup> using trimethylaluminum (TMA) crosslinking agent to cesium lead halide ( $\text{CsPbX}_3$ ) perovskites nanocrystals. High-resolution TEM images of cesium lead iodide ( $\text{CsPbI}_3$ ) perovskites before and after TMA crosslinking indicate that TMA vapor treatment creates alumina networks (Figure 14d,e). Traditional crosslinking methods using ligand exchange often generate cracks, which can play the role of an electrical shunting pathway and, moreover, closely packed nanocrystals could lead to the self-quenching of excitons. The TMA vapor-based crosslinking method links nanocrystals by hydroxide-terminated aluminum oxide while preserving the original structure and electro-optical properties because it does

not involve ligand exchange (Figure 14f). As crosslinking with TMA make films insoluble to toluene, deposition of a transport layer has no critical effect on the properties of perovskite nanoparticles. Synergetic effects of exciton confinement in the perovskite nanoparticles and nearly complete film coverage result in a remarkable EQE of 5.7%.

#### 4.5. Low-Dimensional Perovskites

Beyond the nanostructured 3D perovskites introduced in the previous subsections, low-dimensional perovskites, i.e., 2D, 1D and 0D perovskites with finite numbers of layers, can offer considerable merits as light emitters. Large size organic cations in perovskite structures with a tolerance factor over 1 may induce layered  $\text{A}_2\text{BX}_4$  structures as the large organic cation is difficult to fit into the cuboctahedral cavity. The electric structure of the layered hybrid perovskites shows a multiple nanoscale quantum-well structure, where alternating 2D inorganic semi-conducting layers of  $\text{PbX}_4$  and organic ammonium layers of  $\text{RNH}_3$  (R = aliphatic compound) constitute quantum wells and barriers, respectively.<sup>[36]</sup> The strong confinement of electrons and holes in the layered structure renders large  $E_b$  inducing an efficient luminescence yield (Table 2). Consequently, the layered perovskites are promising structures to simultaneously strengthen the  $E_b$  and reduce the exciton diffusion length for light-emitting applications (see Table 2 and 3).

The first pioneering report on the LED application of low-dimensional perovskite was published about 20 years ago by

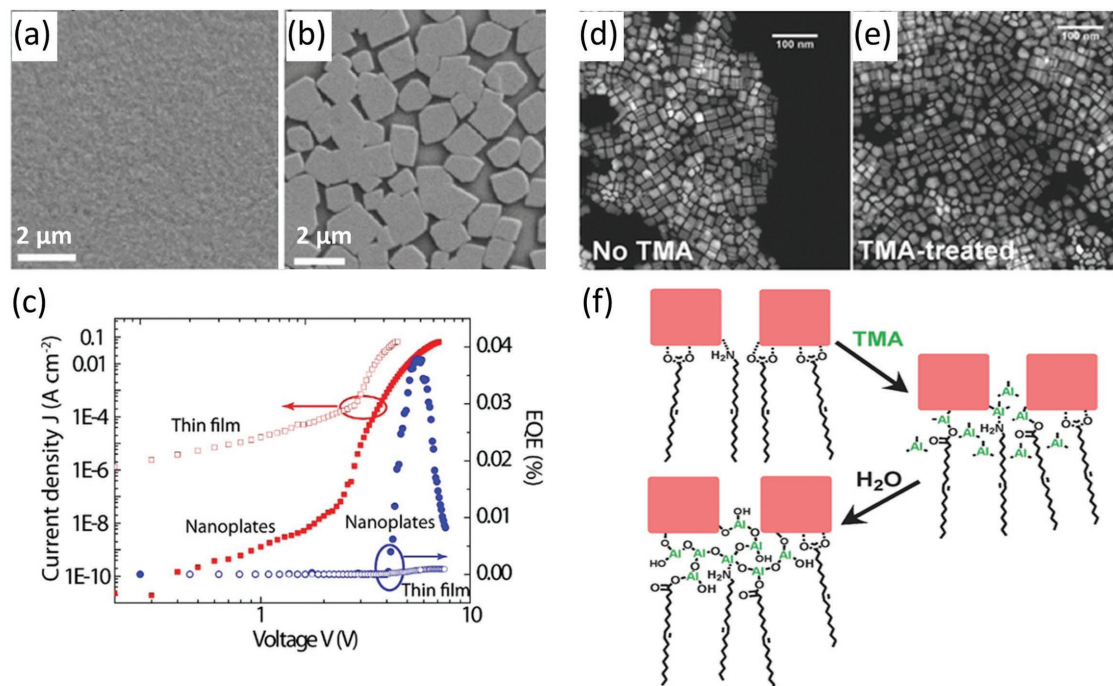


**Figure 14.** a) SEM image of the  $(\text{PEA})_2\text{PbBr}_4$  thin film without DMF treatment and b) SEM image of the  $(\text{PEA})_2\text{PbBr}_4$  nanoplates obtained by annealing. c) Current-voltage  $J$ - $V$  dependence (red symbols) and EQEs (blue symbols) for PeLEDs fabricated with  $(\text{PEA})_2\text{PbBr}_4$  thin film. Panels (a–c) reproduced with permission.<sup>[195]</sup> Copyright 2016, American Chemical Society. High-angle annular dark-field scanning TEM (HAADF-STEM) images of untreated (d) and TMA-treated (e)  $\text{CsPbI}_3$  nanoparticle, used for size-distribution analysis. f) Reaction schematic of the TMA crosslinking process. Panels (d–f) reproduced with permission.<sup>[48]</sup> Copyright 2016, Wiley.



Era et al.<sup>[194]</sup> A PeLED using solution-processed  $(\text{C}_6\text{H}_5\text{C}_2\text{H}_4\text{NH}_3)_2\text{PbI}_4$  (PAPI, PA = phenylammonium ion) layered perovskite exhibited a strong photoluminescence and electroluminescence over  $10\,000\text{ cd m}^{-2}$  at  $2\text{ A cm}^{-2}$  with the device architecture of ITO/ $(\text{C}_6\text{H}_5\text{C}_2\text{H}_4\text{NH}_3)_2\text{PbI}_4$  (PAPI)/oxadiazole derivative/Mg/Ag. Notably, emission bandwidth was estimated to be only 10 nm, indicating very high color purity. This result was attributed to the stable exciton formation with a large  $E_b$  originated from the quantum well band structure from the low-dimensional perovskite nature. Since this first report, layered perovskites have been considered a promising candidates for the enhanced structural stability for LEDs. Despite the great potential of low-dimensional perovskite, it has unfortunately stayed out of the limelight during the past 20 years. Recently, research interest in low-dimensional hybrid perovskites with bulky organic cations has again increased, principally due to the fundamental limits of 3D hybrid perovskites such as low  $E_b$  and long diffusion length. In this context, low dimensional perovskite is a simple structure to enhance the electroluminescence efficiency and stability of LEDs.<sup>[15,16,32,193,206]</sup>

Generally, aliphatic amines can be used as organic cations to form layered perovskites. In 2011, Kitazawa et al. reported the fabrication of the thin films of microcrystalline  $(\text{C}_n\text{H}_{2n+1}\text{NH}_3)_2\text{PbX}_4$  and studied the influence of the number of carbon atoms in aliphatic amines on the excitonic properties.<sup>[207]</sup> With the number of carbons from 1 to 12, the interlayer spacing is controlled while maintaining the thickness of quantum well unchanged. Along with the alkyl chain length, structural phase formation and excitonic structure could be varied, while influencing photoluminescence properties. From the temperature-dependent photoluminescence spectra, exciton binding energies were estimated to be  $350\text{--}420 \pm 50\text{ meV}$ . Hu et al. explored a series of 2D perovskites with a general formula of  $(\text{C}_4\text{H}_9\text{NH}_3)_2(\text{CH}_3\text{NH}_3)_{n-1}\text{Pb}_n\text{I}_{3n+1}$  and which have multiple quantum well structures.<sup>[193]</sup> The quantum well band gap of perovskite compounds could be modified by mixing stoichiometric quantities of alkyl amine components, resulting in the gradually tunable band gap and emission spectra with sustained high  $E_b$ . A series of PeLEDs emitting red, green, and blue light were easily fabricated by tuning the molecular composition and halide substitution. Among them, the red-emitting PeLED exhibited the best luminance of  $214\text{ cd m}^{-2}$  with the maximum EQE of 2.3%.

As discussed above, low-dimensionality leads to more efficient exciton confinement but it comes with the expense of poorer electric conductivity, which originates from the poor charge-transporting properties of enlarged insulating organic amine groups. In order to secure the efficient exciton confinement effect without a significant loss of charge transport capability, large organic amine cations and fine control of the molar ratio of organic amine are essential.<sup>[32,34]</sup> Notably, aromatic organic amines offer charge carrier mobility based on their conformation of intra-aromatic  $\pi\text{--}\pi$  interaction and orientation to inorganic layers. In 2016, Yuan et al. reported PeLEDs based on the multilayered quasi-2D perovskites by incorporating the aromatic bulky cation phenylethylammonium (PEA =  $\text{C}_8\text{H}_9\text{NH}_3$ ). In this attempt, the dimensionality of perovskite is modulated by the ratio of PEA iodide (PEAI) and MAI, resulting in  $\text{PEA}_2(\text{CH}_3\text{NH}_3)_{n-1}\text{Pb}_n\text{I}_{3n+1}$  perovskite. Electronic

structures, particularly the conduction band minimum, tend to gradually increase with the number of layers  $\langle n \rangle$ , while the valence band maximum stays around the same position. In addition,  $E_b$  is also increased with the decrease of dimensionality from  $21 \pm 3$  ( $n = \infty$ ) to  $83 \pm 3\text{ meV}$  ( $n = 3$ ) due to the strong dielectric confinement. The photoluminescence emission peaks undergo blue shifts as the  $n$  value decreases (Figure 15a). Quantum yields reach higher values of 10.1% and 10.6% with  $\langle n \rangle = 3$  and  $\langle n \rangle = 5$ , respectively, while 3D perovskite shows a negligible quantum yield. Interestingly, a practical quasi-2D perovskite film based on solution process consisted of various  $\langle n \rangle$  rather than single  $\langle n \rangle$ , which indicates the distribution of various energy band gaps. This report revealed that photoexcitation is transferred toward the smallest band gap components that excitons radiatively recombine (Figure 15b,c), which is properly named a funneling mechanism. PeLEDs with the structure of ITO/c-TiO<sub>2</sub>/perovskite/F8/MoO<sub>3</sub>/Au shows similar electroluminescence peak shifts to the photoluminescence cases along with the number of  $\langle n \rangle$  (Figure 15e). The best performance is observed from  $\langle n \rangle = 5$  with 8.8% with a high EQE with radiance of  $80\text{ W sr}^{-1}\text{ m}^{-2}$ .

## 5. Conclusion and Outlook

We have reviewed the current progress and status of organic-inorganic hybrid perovskites for efficient solar cells and LEDs, focusing on how the crystallization methods influence the properties of the resulting perovskite and the device performance. As most of the hybrid perovskites undergo crystallization from their precursor solutions, effective crystal growth is critical to attain the desired material properties. In particular, optoelectronic properties of the hybrid perovskites, the key parameter for efficient device demonstration, are widely tunable by crystallization methods such as thermal and solvent annealing, solvent-based intermediates, additives mediation, blending organic molecules, laser crystallization, and low-dimensional perovskite crystals. Significantly,  $E_b$  of hybrid perovskite is widespread (few tens to few hundreds of meV) depending on the crystalline dimension and the size of the crystallites, namely, 3D perovskite with thin-film morphology has a quite lower  $E_b$  than 2D counterparts with nanostructures. Obviously, judicious choice of materials and crystallization strategies are essential to maximize device performance for both light-harvesting and emitting devices.

To date, hybrid perovskite light harvesters have accomplished great success in terms of device efficiency as well as a low-cost solution process surpassing other thin-film solar cell technologies. Inherent superior light harvesting capability has led hybrid perovskite materials to the center of attention. Notably, the crystallization of hybrid perovskite proceeds rapidly because of the strong ionic interaction between the metal cation and the halide anions. Thus, delicate control of the crystallization behavior is critical for high-efficiency solar cells. Aforementioned crystallization methods have aimed at uniform, dense and homogeneous 3D polycrystalline perovskite films, indicating i) high surface coverage, ii) large grain size with minimal grain boundaries, iii) low trap density by managing defect states, and iv) reduced recombination rate.



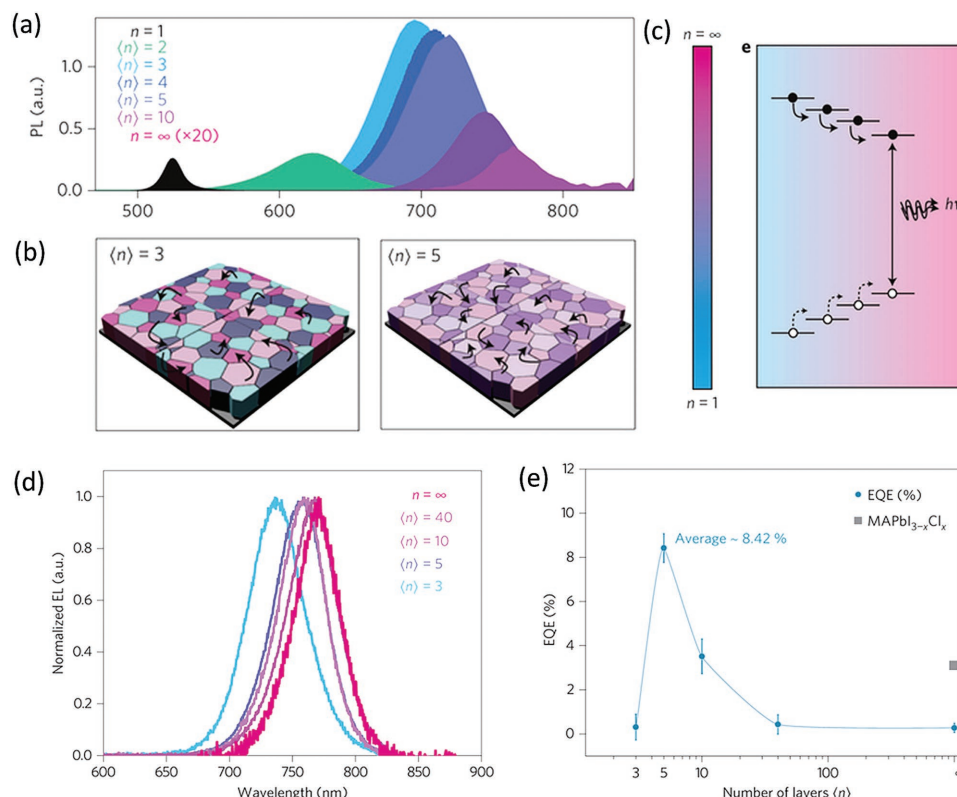


**Figure 15.** a) Steady-state photoluminescence spectra for perovskites with different  $\langle n \rangle$  values. b) The carrier transfer process in  $\langle n \rangle = 3$  perovskite (left) and  $\langle n \rangle = 5$  perovskite (right). c) Multi-phase perovskite materials  $\text{PEA}_2(\text{CH}_3\text{NH}_3)_{n-1}\text{Pb}_{n-1}\text{I}_{3n+1}$  channel energy across an inhomogeneous energy landscape, concentrating carriers to smallest bandgap emitters. The arrows represent the carrier transfer process. d) Electroluminescence spectra of perovskites with different  $\langle n \rangle$  values. e) Summary of the device EQE for perovskites with different  $\langle n \rangle$  values compared with the best reported device EQE for an iodide-based 3D perovskite LED. The average EQE for  $\langle n \rangle = 3$  perovskite LEDs is 8.42%, based on more than 30 devices. Error bars represent the standard deviation of several devices. Reproduced with permission.<sup>[16]</sup> Copyright 2016, Nature Publishing Group.

Currently, solvent-mediated crystallization of perovskites via an intermediate phase generally demonstrates high device performance with dense film morphology and the large grain growth. Along this line, single-crystalline hybrid perovskite could boost the solar cells efficiency, even to over 25%. In fact, there have been interesting reports on single-crystal perovskite-based optoelectronics. Integrated photodetectors on perovskite wafer as thin as  $\approx 150 \mu\text{m}$  demonstrates superior performance compared to microcrystalline thin films particularly because of the high quality crystals with low trap density.<sup>[208–210]</sup>

From the perspective of a perovskite light emitter, considerable progress in the perovskite light-emitting materials have recently been realized. In the initial stage, the fundamental limitation of PeLED was the low  $E_b$  of conventional 3D hybrid perovskites, which readily induces the quenching of excitons. Thus, similar approaches to the perovskite light harvesters resulted in a negligible light emission from PeLEDs. Research efforts to improve the efficiency of PeLEDs have been devoted to the exciton confinement in grains and thereby improving exciton binding energies. Although a 3D perovskite has a relatively lower  $E_b$  than low-dimensional counterparts, nanoscale grain formation (size  $< 100 \text{ nm}$ ) and nanostructuring of the 3D bulk perovskite crystals may enhance exciton confinement and current efficiency of PeLED. It is worth noting that the exact mechanism of high current efficiency with nanoscale

perovskite grains is unclear, as it has been generally considered that a large number of grain boundaries may reduce the radiative decay of excitons in the previous inorganic LED researches. Nonetheless, recent research tends to prefer low-dimensional or nanostructured perovskites. Practically, low-dimensional perovskites and nanostructures such as nanoparticles, nanoplates, and quantum dots show high  $E_b$  on the order of a few hundred meV. However, the device efficiency is still limited due to the lack of methods forming uniform thin film with complete surface coverage. Effective thin-film formation based on the low-dimensional nanostructured perovskite should be one of the principal challenges for future PeLEDs.

Putting the dramatic evolution of perovskite optoelectronics on hold, enormous effort is still necessary for the realization of practical perovskite optoelectronic devices for real-world applications. Currently, the best performing perovskite optoelectronic devices are still based on toxic Pb metal cations. Toxic-element-free perovskites are crucial for the environmentally benign clean energy supply. In this regard, non-toxic metal cations such as Sn, Bi, and Ge have been proposed as alternatives but the device performances based on those elements need to be greatly improved. The stability issue of perovskite crystals also must be addressed for the reliable long-term outdoor device operation. As is well-known, rapid decomposition of typical organic–inorganic hybrid perovskites upon humidity,

light-soaking, and even bias stress is a major bottleneck for the device reliability. Furthermore, development of rapid continuous crystallization process is an urgent demand for both solar cells and displays together with the current industrial trend toward flexible and wearable devices. Presently, batch type crystallization with time-consuming temperature control is dominant, which inherently limits the development of flexible perovskite devices despite genuine material flexibility of organic-inorganic hybrid perovskites. From this perspective, laser crystallization, which is already widely used in the inorganic material crystallization for display industry, should be a promising candidate because of its unprecedented advantages, including genuine continuous processibility, large-area scalability and instantaneous processing under ambient conditions, minimal influence in the surrounding device structures, and so on. Our research group recently demonstrated that low energy laser crystallization of perovskite using near infrared laser is a promising crystallization method for perovskite device structures, which is also compatible to the roll-to-roll process for beam-damage-free perovskite optoelectronics. Despite all these remaining challenges, continued research effort in this field is anticipated to open a bright outlook for perovskite-based optoelectronics in the near future.

## Acknowledgements

T.J. and S.J.K. contributed to equally to this work. This work was supported by the National Creative Research Initiative (CRI) Center for Multi-Dimensional Directed Nanoscale Assembly (2015R1A3A2033061), Nano Material Technology Development Program through the National Research Foundation of Korea (NRF) funded by the Ministry of Science, ICT and Future Planning (2016M3A7B4905609), and Global Frontier Program through the Global Frontier Hybrid Interface Materials (GFHIM) of NRF funded by the Ministry of Science, ICT & Future Planning (2013M3A6B1078874).

## Keywords

crystallization, hybrid perovskites, light-emitting diodes, optoelectronics, solar cells

Received: November 23, 2016

Revised: January 31, 2017

Published online: May 24, 2017

- [1] NREL, Best Research Cell Efficiencies, [http://www.nrel.gov/ncpv/images/efficiency\\_chart.jpg](http://www.nrel.gov/ncpv/images/efficiency_chart.jpg) (accessed: October 2016).
- [2] A. G. Martin, H.-B. Anita, J. S. Henry, *Nat. Photonics* **2014**, *8*, 506.
- [3] J. H. Noh, S. H. Im, J. H. Heo, T. N. Mandal, S. I. Seok, *Nano Lett.* **2013**, *13*, 1764.
- [4] S. D. Stranks, G. E. Eperon, G. Grancini, C. Menelaou, M. J. P. Alcocer, T. Leijtens, L. M. Herz, A. Petrozza, H. J. Snaith, *Science* **2013**, *342*, 341.
- [5] D. Liu, T. L. Kelly, *Nat. Photonics* **2014**, *8*, 133.
- [6] Q. Dong, Y. Fang, Y. Shao, P. Mulligan, J. Qiu, L. Cao, J. Huang, *Science* **2015**, *347*, 967.
- [7] G. E. Eperon, S. D. Stranks, C. Menelaou, M. B. Johnston, L. M. Herz, H. J. Snaith, *Energy Environ. Sci.* **2014**, *7*, 982.
- [8] M. E. Ziffer, J. C. Mohammed, D. S. Ginger, *ACS Photonics* **2016**, *3*, 1060.
- [9] A. Marchioro, J. Teuscher, D. Friedrich, M. Kunst, R. van de Krol, T. Moehl, M. Grätzel, J.-E. Moser, *Nat. Photonics* **2014**, *8*, 250.
- [10] M. M. Lee, J. Teuscher, T. Miyasaka, T. N. Murakami, H. J. Snaith, *Science* **2012**, *338*, 643.
- [11] D. P. McMeekin, G. Sadoughi, W. Rehman, G. E. Eperon, M. Saliba, M. T. Hörantner, A. Haghighirad, N. Sakai, L. Korte, B. Rech, M. B. Johnston, L. M. Herz, H. J. Snaith, *Science* **2016**, *351*, 151.
- [12] H. Zhou, Q. Chen, G. Li, S. Luo, T.-b. Song, H.-S. Duan, Z. Hong, J. You, Y. Liu, Y. Yang, *Science* **2014**, *345*, 542.
- [13] X. Zhang, H. Lin, H. Huang, C. Reckmeier, Y. Zhang, W. C. H. Choy, A. L. Rogach, *Nano Lett.* **2016**, *16*, 1415.
- [14] H. Cho, S.-H. Jeong, M.-H. Park, Y.-H. Kim, C. Wolf, C.-L. Lee, J. H. Heo, A. Sadhanala, N. Myoung, S. Yoo, S. H. Im, R. H. Friend, T.-W. Lee, *Science* **2015**, *350*, 1222.
- [15] M. Wei, W. Sun, Y. Liu, Z. Liu, L. Xiao, Z. Bian, Z. Chen, *Phys. Status Solidi A* **2016**, *213*, 2727.
- [16] M. Yuan, L. N. Quan, R. Comin, G. Walters, R. Sabatini, O. Voznyy, S. Hoogland, Y. Zhao, E. M. Bearegard, P. Kanjanaboos, Z. Lu, D. H. Kim, E. H. Sargent, *Nat. Nanotechnol.* **2016**, *11*, 872.
- [17] J. Xing, F. Yan, Y. Zhao, S. Chen, H. Yu, Q. Zhang, R. Zeng, H. V. Demir, X. Sun, A. Huan, Q. Xiong, *ACS Nano* **2016**, *10*, 6623.
- [18] Y.-H. Kim, H. Cho, T.-W. Lee, *Proc. Natl. Acad. Sci. USA* **2016**, *113*, 11694.
- [19] X. Hong, T. Ishihara, A. V. Nurmikko, *Solid State Commun.* **1992**, *84*, 657.
- [20] A. Kojima, K. Teshima, Y. Shirai, T. Miyasaka, *J. Am. Chem. Soc.* **2009**, *131*, 6050.
- [21] H.-S. Kim, C.-R. Lee, J.-H. Im, K.-B. Lee, T. Moehl, A. Marchioro, S.-J. Moon, R. Humphry-Baker, J.-H. Yum, J. E. Moser, M. Grätzel, N.-G. Park, *Sci. Rep.* **2012**, *2*, 591.
- [22] L. Dou, Y. M. Yang, J. You, Z. Hong, W. H. Chang, G. Li, Y. Yang, *Nat. Commun.* **2014**, *5*, 5404.
- [23] S. A. Veldhuis, P. P. Boix, N. Yantara, M. Li, T. C. Sum, N. Mathews, S. G. Mhaisalkar, *Adv. Mater.* **2016**, *28*, 6804.
- [24] H. S. Jung, N.-G. Park, *Small* **2015**, *11*, 10.
- [25] Q. Chen, N. De Marco, Y. Yang, T.-B. Song, C.-C. Chen, H. Zhao, Z. Hong, H. Zhou, Y. Yang, *Nano Today* **2015**, *10*, 355.
- [26] Z. K. Tan, R. S. Moghaddam, M. L. Lai, P. Docampo, R. Higler, F. Deschler, M. Price, A. Sadhanala, L. M. Pazos, D. Credgington, F. Hanusch, T. Bein, H. J. Snaith, R. H. Friend, *Nat. Nanotechnol.* **2014**, *9*, 687.
- [27] J. C. Yu, D. B. Kim, G. Baek, B. R. Lee, E. D. Jung, S. Lee, J. H. Chu, D.-K. Lee, K. J. Choi, S. Cho, M. H. Song, *Adv. Mater.* **2015**, *27*, 3492.
- [28] Z. Xiao, R. A. Kerner, L. Zhao, N. L. Tran, K. M. Lee, T.-W. Koh, G. D. Scholes, B. P. Rand, *Nat. Photonics* **2017**, *11*, 108.
- [29] Y. Chen, M. He, J. Peng, Y. Sun, Z. Liang, *Adv. Sci.* **2016**, *3*, 1500392.
- [30] W. Zhang, G. E. Eperon, H. J. Snaith, *Nat. Energy* **2016**, *1*, 16048.
- [31] S. D. Stranks, H. J. Snaith, *Nat. Nanotechnol.* **2015**, *10*, 391.
- [32] J. Byun, H. Cho, C. Wolf, M. Jang, A. Sadhanala, R. H. Friend, H. Yang, T.-W. Lee, *Adv. Mater.* **2016**, *28*, 7515.
- [33] Z. Yuan, Y. Shu, Y. Xin, B. Ma, *Chem. Commun.* **2016**, *52*, 3887.
- [34] L. N. Quan, M. Yuan, R. Comin, O. Voznyy, E. M. Bearegard, S. Hoogland, A. Buin, A. R. Kirmani, K. Zhao, A. Amassian, D. H. Kim, E. H. Sargent, *J. Am. Chem. Soc.* **2016**, *138*, 2649.
- [35] C. Li, X. Lu, W. Ding, L. Feng, Y. Gao, Z. Guo, *Acta Crystallogr., Sect. B* **2008**, *64*, 702.
- [36] D. B. Mitzi, *J. Chem. Soc., Dalton Trans.* **2001**, *1*.
- [37] F. Brivio, A. B. Walker, A. Walsh, *APL Mater.* **2013**, *1*, 042111.
- [38] C. C. Stoumpos, C. D. Malliakas, M. G. Kanatzidis, *Inorg. Chem.* **2013**, *52*, 9019.

- [39] N. Ahn, D.-Y. Son, I.-H. Jang, S. M. Kang, M. Choi, N.-G. Park, *J. Am. Chem. Soc.* **2015**, *137*, 8696.
- [40] J. H. Heo, M. S. You, M. H. Chang, W. Yin, T. K. Ahn, S.-J. Lee, S.-J. Sung, D. H. Kim, S. H. Im, *Nano Energy* **2015**, *15*, 530.
- [41] T. Baikie, Y. Fang, J. M. Kadro, M. Schreyer, F. Wei, S. G. Mhaisalkar, M. Graetzel, T. J. White, *J. Mater. Chem. A* **2013**, *1*, 5628.
- [42] X. Zhao, N.-G. Park, *Photonics* **2015**, *2*, 1139.
- [43] I. Grinberg, D. V. West, M. Torres, G. Gou, D. M. Stein, L. Wu, G. Chen, E. M. Gallo, A. R. Akbashev, P. K. Davies, J. E. Spanier, A. M. Rappe, *Nature* **2013**, *503*, 509.
- [44] W. S. Yang, J. H. Noh, N. J. Jeon, Y. C. Kim, S. Ryu, J. Seo, S. I. Seok, *Science* **2015**, *348*, 1234.
- [45] D.-Y. Son, J.-W. Lee, Y. J. Choi, I.-H. Jang, S. Lee, P. J. Yoo, H. Shin, N. Ahn, M. Choi, D. Kim, N.-G. Park, *Nat. Energy* **2016**, *1*, 16081.
- [46] W. Shockley, H. J. Queisser, *J. Appl. Phys.* **1961**, *32*, 510.
- [47] Z.-K. Tan, R. S. Moghaddam, M. L. Lai, P. Docampo, R. Higler, F. Deschler, M. Price, A. Sadhanala, L. M. Pazos, D. Credgington, F. Hanusch, T. Bein, H. J. Snaith, R. H. Friend, *Nat. Nanotechnol.* **2014**, *9*, 687.
- [48] G. Li, F. W. R. Rivarola, N. J. L. K. Davis, S. Bai, T. C. Jellicoe, F. de la Peña, S. Hou, C. Ducati, F. Gao, R. H. Friend, N. C. Greenham, Z.-K. Tan, *Adv. Mater.* **2016**, *28*, 3528.
- [49] F. Hao, C. C. Stoumpos, D. H. Cao, R. P. Chang, M. G. Kanatzidis, *Nat. Photonics* **2014**, *8*, 489.
- [50] G. E. Eperon, T. Leijtens, K. A. Bush, R. Prasanna, T. Green, J. T. Wang, D. P. McMeekin, G. Volonakis, R. L. Milot, R. May, A. Palmstrom, D. J. Slotcavage, R. A. Belisle, J. B. Patel, E. S. Parrott, R. J. Sutton, W. Ma, F. Moghadam, B. Conings, A. Babayigit, H. G. Boyen, S. Bent, F. Giustino, L. M. Herz, M. B. Johnston, M. D. McGehee, H. J. Snaith, *Science* **2016**, *354*, 861.
- [51] F. Hao, C. C. Stoumpos, R. P. H. Chang, M. G. Kanatzidis, *J. Am. Chem. Soc.* **2014**, *136*, 8094.
- [52] Y. Ogomi, A. Morita, S. Tsukamoto, T. Saitho, N. Fujikawa, Q. Shen, T. Toyoda, K. Yoshino, S. S. Pandey, T. Ma, S. Hayase, *J. Phys. Chem. Lett.* **2014**, *5*, 1004.
- [53] Z. Yang, A. Rajagopal, C.-C. Chueh, S. B. Jo, B. Liu, T. Zhao, A. K. Y. Jen, *Adv. Mater.* **2016**, *28*, 8990.
- [54] Y. Li, W. Sun, W. Yan, S. Ye, H. Rao, H. Peng, Z. Zhao, Z. Bian, Z. Liu, H. Zhou, C. Huang, *Adv. Energy Mater.* **2016**, *6*, 1601353.
- [55] W. Liao, D. Zhao, Y. Yu, N. Shrestha, K. Ghimire, C. R. Grice, C. Wang, Y. Xiao, A. J. Cimaroli, R. J. Ellingson, N. J. Podraza, K. Zhu, R.-G. Xiong, Y. Yan, *J. Am. Chem. Soc.* **2016**, *138*, 12360.
- [56] R. Hill, *J. Phys. C: Solid State Phys.* **1974**, *7*, 521.
- [57] R. Venugopal, P.-I. Lin, Y.-T. Chen, *J. Phys. Chem. B* **2006**, *110*, 11691.
- [58] H. Yu, F. Wang, F. Xie, W. Li, J. Chen, N. Zhao, *Adv. Funct. Mater.* **2014**, *24*, 7102.
- [59] E. L. Unger, A. R. Bowring, C. J. Tassone, V. L. Pool, A. Gold-Parker, R. Cheacharoen, K. H. Stone, E. T. Hoke, M. F. Toney, M. D. McGehee, *Chem. Mater.* **2014**, *26*, 7158.
- [60] Y. Tidhar, E. Edri, H. Weissman, D. Zohar, G. Hodes, D. Cahen, B. Rybtchinski, S. Kirmayer, *J. Am. Chem. Soc.* **2014**, *136*, 13249.
- [61] Y.-H. Kim, H. Cho, J. H. Heo, T.-S. Kim, N. Myoung, C.-L. Lee, S. H. Im, T.-W. Lee, *Adv. Mater.* **2015**, *27*, 1248.
- [62] J. H. Heo, D. H. Song, S. H. Im, *Adv. Mater.* **2014**, *26*, 8179.
- [63] M. G. Walter, E. L. Warren, J. R. McKone, S. W. Boettcher, Q. Mi, E. A. Santori, N. S. Lewis, *Chem. Rev.* **2010**, *110*, 6446.
- [64] W. Y. Liang, *Phys. Educ.* **1970**, *5*, 226.
- [65] J. Singh, *Excitation Energy Transfer Processes in Condensed Matter: Theory and Applications*, Springer US, Boston, MA **1994**, p. 1.
- [66] B. A. Gregg, M. C. Hanna, *J. Appl. Phys.* **2003**, *93*, 3605.
- [67] Q. Lin, A. Armin, R. C. R. Nagiri, P. L. Burn, P. Meredith, *Nat. Photonics* **2015**, *9*, 106.
- [68] D. I. Valerio, G. Giulia, J. P. A. Marcelo, K. Ajay Ram Srimath, D. S. Samuel, M. L. Michael, L. Guglielmo, J. S. Henry, P. Annamaria, *Nat. Commun.* **2014**, *5*, 3586.
- [69] J. S. Manser, P. V. Kamat, *Nat. Photonics* **2014**, *8*, 737.
- [70] A. Miyata, A. Mitioglu, P. Plochocka, O. Portugall, J. T.-W. Wang, S. D. Stranks, H. J. Snaith, R. J. Nicholas, *Nat. Phys.* **2015**, *11*, 582.
- [71] W. Tress, N. Marinova, O. Inganäs, M. K. Nazeeruddin, S. M. Zakeeruddin, M. Graetzel, *Adv. Energy Mater.* **2015**, *5*, 1400812.
- [72] K. Tanaka, T. Takahashi, T. Ban, T. Kondo, K. Uchida, N. Miura, *Solid State Commun.* **2003**, *127*, 619.
- [73] Y. Yang, M. Yang, Z. Li, R. Crisp, K. Zhu, M. C. Beard, *J. Phys. Chem. Lett.* **2015**, *6*, 4688.
- [74] K. Galkowski, A. Mitioglu, A. Miyata, P. Plochocka, O. Portugall, G. E. Eperon, J. T.-W. Wang, T. Stergiopoulos, S. D. Stranks, H. J. Snaith, R. J. Nicholas, *Energy Environ. Sci.* **2016**, *9*, 962.
- [75] K. Zheng, Q. Zhu, M. Abdellah, M. E. Messing, W. Zhang, A. Generalov, Y. Niu, L. Ribaud, S. E. Canton, T. Pullerits, *J. Phys. Chem. Lett.* **2015**, *6*, 2969.
- [76] I. B. Koutselas, L. Ducasse, G. C. Papavassiliou, *J. Phys.: Condens. Matter* **1996**, *8*, 1217.
- [77] T. Ishihara, J. Takahashi, T. Goto, *Solid State Commun.* **1989**, *69*, 933.
- [78] M. Shimizu, N. A. Gippius, S. G. Tikhodeev, T. Ishihara, *Phys. Rev. B* **2004**, *69*, 155201.
- [79] M. Hirasawa, T. Ishihara, T. Goto, *J. Phys. Soc. Jpn.* **1994**, *63*, 3870.
- [80] J. You, Z. Hong, Y. M. Yang, Q. Chen, M. Cai, T. B. Song, C. C. Chen, S. Lu, Y. Liu, H. Zhou, Y. Yang, *ACS Nano* **2014**, *8*, 1674.
- [81] W. Ke, G. Fang, Q. Liu, L. Xiong, P. Qin, H. Tao, J. Wang, H. Lei, B. Li, J. Wan, G. Yang, Y. Yan, *J. Am. Chem. Soc.* **2015**, *137*, 6730.
- [82] E. H. Anaraki, A. Kermanpur, L. Steier, K. Domanski, T. Matsui, W. Tress, M. Saliba, A. Abate, M. Gratzel, A. Hagfeldt, J.-P. Correa-Baena, *Energy Environ. Sci.* **2016**, *9*, 3128.
- [83] S. S. Shin, W. S. Yang, J. H. Noh, J. H. Suk, N. J. Jeon, J. H. Park, J. S. Kim, W. M. Seong, S. I. Seok, *Nat. Commun.* **2015**, *6*, 7410.
- [84] H. Kim, K.-G. Lim, T.-W. Lee, *Energy Environ. Sci.* **2016**, *9*, 12.
- [85] A. Abruci, S. D. Stranks, P. Docampo, H.-L. Yip, A. K. Y. Jen, H. J. Snaith, *Nano Lett.* **2013**, *13*, 3124.
- [86] F. Giordano, A. Abate, J. P. Correa Baena, M. Saliba, T. Matsui, S. H. Im, S. M. Zakeeruddin, M. K. Nazeeruddin, A. Hagfeldt, M. Graetzel, *Nat. Commun.* **2016**, *7*, 10379.
- [87] J. Kim, G. Kim, T. K. Kim, S. Kwon, H. Back, J. Lee, S. H. Lee, H. Kang, K. Lee, *J. Mater. Chem. A* **2014**, *2*, 17291.
- [88] C. S. Lee, J. K. Kim, J. T. Park, J. H. Kim, *Macromol. Res.* **2016**, *24*, 573.
- [89] K.-G. Lim, H.-B. Kim, J. Jeong, H. Kim, J. Y. Kim, T.-W. Lee, *Adv. Mater.* **2014**, *26*, 6461.
- [90] K.-G. Lim, S. Ahn, H. Kim, M.-R. Choi, D. H. Huh, T.-W. Lee, *Adv. Mater. Interfaces* **2016**, *3*, 1500678.
- [91] S. Ryu, J. H. Noh, N. J. Jeon, Y. C. Kim, S. Yang, J. W. Seo, S. I. Seok, *Energy Environ. Sci.* **2014**, *7*, 2614.
- [92] K.-G. Lim, S. Ahn, Y.-H. Kim, Y. Qi, T.-W. Lee, *Energy Environ. Sci.* **2016**, *9*, 932.
- [93] A. Abate, T. Leijtens, S. Pathak, J. Teuscher, R. Avolio, M. E. Errico, J. Kirkpatrick, J. M. Ball, P. Docampo, I. McPherson, H. J. Snaith, *Phys. Chem. Chem. Phys.* **2013**, *15*, 2572.
- [94] N. J. Jeon, H. G. Lee, Y. C. Kim, J. Seo, J. H. Noh, J. Lee, S. I. Seok, *J. Am. Chem. Soc.* **2014**, *136*, 7837.
- [95] J. Liu, Y. Wu, C. Qin, X. Yang, T. Yasuda, A. Islam, K. Zhang, W. Peng, W. Chen, L. Han, *Energy Environ. Sci.* **2014**, *7*, 2963.
- [96] Z. Zhu, Y. Bai, T. Zhang, Z. Liu, X. Long, Z. Wei, Z. Wang, L. Zhang, J. Wang, F. Yan, S. Yang, *Angew. Chem. Int. Ed.* **2014**, *126*, 12779.
- [97] J. H. Kim, P.-W. Liang, S. T. Williams, N. Cho, C.-C. Chueh, M. S. Glaz, D. S. Ginger, A. K. Y. Jen, *Adv. Mater.* **2015**, *27*, 695.



- [98] N. J. Jeon, J. H. Noh, Y. C. Kim, W. S. Yang, S. Ryu, S. I. Seok, *Nat. Mater.* **2014**, 13, 897.
- [99] J.-H. Im, I.-H. Jang, N. Pellet, M. Grätzel, N.-G. Park, *Nat. Nanotechnol.* **2014**, 9, 927.
- [100] M. Liu, M. B. Johnston, H. J. Snaith, *Nature* **2013**, 501, 395.
- [101] K. Hwang, Y.-S. Jung, Y.-J. Heo, F. H. Scholes, S. E. Watkins, J. Subbiah, D. J. Jones, D.-Y. Kim, D. Vak, *Adv. Mater.* **2015**, 27, 1241.
- [102] A. T. Barrows, A. J. Pearson, C. K. Kwak, A. D. F. Dunbar, A. R. Buckley, D. G. Lidzey, *Energy Environ. Sci.* **2014**, 7, 2944.
- [103] S. Das, B. Yang, G. Gu, P. C. Joshi, I. N. Ivanov, C. M. Rouleau, T. Aytug, D. B. Geohegan, K. Xiao, *ACS Photonics* **2015**, 2, 680.
- [104] Y. Deng, E. Peng, Y. Shao, Z. Xiao, Q. Dong, J. Huang, *Energy Environ. Sci.* **2015**, 8, 1544.
- [105] J.-H. Im, C.-R. Lee, J.-W. Lee, S.-W. Park, N.-G. Park, *Nanoscale* **2011**, 3, 4088.
- [106] J. H. Heo, S. H. Im, J. H. Noh, T. N. Mandal, C. S. Lim, J. A. Chang, Y. H. Lee, H. J. Kim, A. Sarkar, M. K. Nazeeruddin, M. Grätzel, S. I. Seok, *Nat. Photonics* **2013**, 7, 487.
- [107] M. Xiao, F. Huang, W. Huang, Y. Dkhissi, Y. Zhu, J. Etheridge, A. Gray-Weale, U. Bach, Y. B. Cheng, L. Spiccia, *Angew. Chem. Int. Ed.* **2014**, 53, 9898.
- [108] J. W. Jung, S. T. Williams, A. K. Y. Jen, *RSC Adv.* **2014**, 4, 62971.
- [109] J. Burschka, N. Pellet, S.-J. Moon, R. Humphry-Baker, P. Gao, M. K. Nazeeruddin, M. Grätzel, *Nature* **2013**, 499, 316.
- [110] Q. Chen, H. Zhou, Z. Hong, S. Luo, H. S. Duan, H. H. Wang, Y. Liu, G. Li, Y. Yang, *J. Am. Chem. Soc.* **2014**, 136, 622.
- [111] C. Bi, Y. Shao, Y. Yuan, Z. Xiao, C. Wang, Y. Gao, J. Huang, *J. Mater. Chem. A* **2014**, 2, 18508.
- [112] X. Li, D. Bi, C. Yi, J. D. Decoppet, J. Luo, S. M. Zakeeruddin, A. Hagfeldt, M. Grätzel, *Science* **2016**, 353, 58.
- [113] Y.-H. Kim, H. Cho, J. H. Heo, S. H. Im, T.-W. Lee, *Curr. Appl. Phys.* **2016**, 16, 1069.
- [114] Y. Chen, Y. Zhao, Z. Liang, *Chem. Mater.* **2015**, 27, 1448.
- [115] M. Yin, F. Xie, H. Chen, X. Yang, F. Ye, E. Bi, Y. Wu, M. Cai, L. Han, *J. Mater. Chem. A* **2016**, 4, 8548.
- [116] A. Dualeh, N. Tétreault, T. Moehl, P. Gao, M. K. Nazeeruddin, M. Grätzel, *Adv. Funct. Mater.* **2014**, 24, 3250.
- [117] G. E. Eperon, V. M. Burlakov, P. Docampo, A. Goriely, H. J. Snaith, *Adv. Funct. Mater.* **2014**, 24, 151.
- [118] B. Conings, L. Baeten, T. Jacobs, R. Dera, J. D'Haen, J. Manca, H.-G. Boyen, *APL Mater.* **2014**, 2, 081505.
- [119] W. Nie, H. Tsai, R. Asadpour, J.-C. Blancon, A. J. Neukirch, G. Gupta, J. J. Crochet, M. Chhowalla, S. Tretiak, M. A. Alam, H.-L. Wang, A. D. Mohite, *Science* **2015**, 347, 522.
- [120] Y. Shao, Z. Xiao, C. Bi, Y. Yuan, J. Huang, *Nat. Commun.* **2014**, 5, 5784.
- [121] M. Saliba, K. W. Tan, H. Sai, D. T. Moore, T. Scott, W. Zhang, L. A. Estroff, U. Wiesner, H. J. Snaith, *J. Phys. Chem. C* **2014**, 118, 17171.
- [122] R. Kang, J.-E. Kim, J.-S. Yeo, S. Lee, Y.-J. Jeon, D.-Y. Kim, *J. Phys. Chem. C* **2014**, 118, 26513.
- [123] M.-F. Xu, H. Zhang, S. Zhang, H. L. Zhu, H.-M. Su, J. Liu, K. S. Wong, L.-S. Liao, W. C. H. Choy, *J. Mater. Chem. A* **2015**, 3, 14424.
- [124] P. W. Liang, C. Y. Liao, C. C. Chueh, F. Zuo, S. T. Williams, X. K. Xin, J. Lin, A. K. Jen, *Adv. Mater.* **2014**, 26, 3748.
- [125] X. Li, M. Ibrahim Dar, C. Yi, J. Luo, M. Tschumi, S. M. Zakeeruddin, M. K. Nazeeruddin, H. Han, M. Grätzel, *Nat. Chem.* **2015**, 7, 703.
- [126] C.-H. Chiang, C.-G. Wu, *Nat. Photonics* **2016**, 10, 196.
- [127] C.-Y. Chang, C.-Y. Chu, Y.-C. Huang, C.-W. Huang, S.-Y. Chang, C.-A. Chen, C.-Y. Chao, W.-F. Su, *ACS Appl. Mater. Interfaces* **2015**, 7, 4955.
- [128] C.-C. Chueh, C.-Y. Liao, F. Zuo, S. T. Williams, P.-W. Liang, A. K. Y. Jen, *J. Mater. Chem. A* **2015**, 3, 9058.
- [129] P. Docampo, F. C. Hanusch, S. D. Stranks, M. Döbbling, J. M. Feckl, M. Ehrensperger, N. K. Minar, M. B. Johnston, H. J. Snaith, T. Bein, *Adv. Energy Mater.* **2014**, 4, 1400355.
- [130] M. K. Kim, T. Jeon, H. I. Park, J. M. Lee, S. A. Nam, S. O. Kim, *Cryst. Eng. Commun.* **2016**, 18, 6090.
- [131] C. Zuo, L. Ding, *Nanoscale* **2014**, 6, 9935.
- [132] J. H. Heo, D. H. Song, H. J. Han, S. Y. Kim, J. H. Kim, D. Kim, H. W. Shin, T. K. Ahn, C. Wolf, T.-W. Lee, S. H. Im, *Adv. Mater.* **2015**, 27, 3424.
- [133] Z. Wang, Y. Zhou, S. Pang, Z. Xiao, J. Zhang, W. Chai, H. Xu, Z. Liu, N. P. Padture, G. Cui, *Chem. Mater.* **2015**, 27, 7149.
- [134] Z. Xiao, Q. Dong, C. Bi, Y. Shao, Y. Yuan, J. Huang, *Adv. Mater.* **2014**, 26, 6503.
- [135] J. Song, E. Zheng, J. Bian, X.-F. Wang, W. Tian, Y. Sanehira, T. Miyasaka, *J. Mater. Chem. A* **2015**, 3, 10837.
- [136] J. Lian, Q. Wang, Y. Yuan, Y. Shao, J. Huang, *J. Mater. Chem. A* **2015**, 3, 9146.
- [137] J. You, Y. Yang, Z. Hong, T.-B. Song, L. Meng, Y. Liu, C. Jiang, H. Zhou, W.-H. Chang, G. Li, Y. Yang, *Appl. Phys. Lett.* **2014**, 105, 183902.
- [138] H. Yu, X. Liu, Y. Xia, Q. Dong, K. Zhang, Z. Wang, Y. Zhou, B. Song, Y. Li, *J. Mater. Chem. A* **2016**, 4, 321.
- [139] Y. Jiang, E. J. Juarez-Perez, Q. Ge, S. Wang, M. R. Leyden, L. K. Ono, S. R. Raga, J. Hu, Y. Qi, *Mater. Horiz.* **2016**, 3, 548.
- [140] J. Liu, C. Gao, X. He, Q. Ye, L. Ouyang, D. Zhuang, C. Liao, J. Mei, W. Lau, *ACS Appl. Mater. Interfaces* **2015**, 7, 24008.
- [141] D. Liu, L. Wu, C. Li, S. Ren, J. Zhang, W. Li, L. Feng, *ACS Appl. Mater. Interfaces* **2015**, 7, 16330.
- [142] Z. Zhou, Z. Wang, Y. Zhou, S. Pang, D. Wang, H. Xu, Z. Liu, N. P. Padture, G. Cui, *Angew. Chem. Int. Ed.* **2015**, 54, 9705.
- [143] F. X. Xie, D. Zhang, H. Su, X. Ren, K. S. Wong, M. Grätzel, W. C. H. Choy, *ACS Nano* **2015**, 9, 639.
- [144] N. J. Jeon, J. H. Noh, Y. C. Kim, W. S. Yang, S. Ryu, S. I. Seok, *Nat. Mater.* **2014**, 13, 897.
- [145] D. Shen, X. Yu, X. Cai, M. Peng, Y. Ma, X. Su, L. Xiao, D. Zou, *J. Mater. Chem. A* **2014**, 2, 20454.
- [146] T. Jeon, H. M. Jin, S. H. Lee, J. M. Lee, H. I. Park, M. K. Kim, K. J. Lee, B. Shin, S. O. Kim, *ACS Nano* **2016**, 10, 7907.
- [147] T. Supasai, N. Rujisamphan, K. Ullrich, A. Chemseddine, T. Dittrich, *Appl. Phys. Lett.* **2013**, 103, 183906.
- [148] Z. Xiao, C. Bi, Y. Shao, Q. Dong, Q. Wang, Y. Yuan, C. Wang, Y. Gao, J. Huang, *Energy Environ. Sci.* **2014**, 7, 2619.
- [149] J.-H. Im, I.-H. Jang, N. Pellet, M. Grätzel, N.-G. Park, *Nat. Nanotechnol.* **2014**, 9, 927.
- [150] J.-H. Im, H.-S. Kim, N.-G. Park, *APL Mater.* **2014**, 2, 081510.
- [151] P. Schulz, E. Edri, S. Kirmayer, G. Hodes, D. Cahen, A. Kahn, *Energy Environ. Sci.* **2014**, 7, 1377.
- [152] Q. Wang, Y. Shao, H. Xie, L. Lyu, X. Liu, Y. Gao, J. Huang, *Appl. Phys. Lett.* **2014**, 105, 163508.
- [153] S. Colella, E. Mosconi, P. Fedeli, A. Listorti, F. Gazza, F. Orlandi, P. Ferro, T. Besagni, A. Rizzo, G. Calestani, G. Gigli, F. De Angelis, R. Mosca, *Chem. Mater.* **2013**, 25, 4613.
- [154] C.-W. Chen, H.-W. Kang, S.-Y. Hsiao, P.-F. Yang, K.-M. Chiang, H.-W. Lin, *Adv. Mater.* **2014**, 26, 6647.
- [155] J. M. Frost, K. T. Butler, F. Brivio, C. H. Hendon, M. van Schilfgaarde, A. Walsh, *Nano Lett.* **2014**, 14, 2584.
- [156] N. J. Jeon, J. H. Noh, W. S. Yang, Y. C. Kim, S. Ryu, J. Seo, S. I. Seok, *Nature* **2015**, 517, 476.
- [157] Q. Han, S.-H. Bae, P. Sun, Y.-T. Hsieh, Y. Yang, Y. S. Rim, H. Zhao, Q. Chen, W. Shi, G. Li, Y. Yang, *Adv. Mater.* **2016**, 28, 2253.
- [158] T. M. Koh, K. Fu, Y. Fang, S. Chen, T. C. Sum, N. Mathews, S. G. Mhaisalkar, P. P. Boix, T. Baikie, *J. Phys. Chem. C* **2014**, 118, 16458.
- [159] S. Pang, H. Hu, J. Zhang, S. Lv, Y. Yu, F. Wei, T. Qin, H. Xu, Z. Liu, G. Cui, *Chem. Mater.* **2014**, 26, 1485.

- [160] J.-W. Lee, D.-J. Seol, A.-N. Cho, N.-G. Park, *Adv. Mater.* **2014**, 26, 4991.
- [161] Y. Sun, G. C. Welch, W. L. Leong, C. J. Takacs, G. C. Bazan, A. J. Heeger, *Nat. Mater.* **2012**, 11, 44.
- [162] Y. Liang, Z. Xu, J. Xia, S.-T. Tsai, Y. Wu, G. Li, C. Ray, L. Yu, *Adv. Mater.* **2010**, 22, E135.
- [163] A. Zusan, B. Giesekeing, M. Zerson, V. Dyakonov, R. Magerle, C. Deibel, *Sci. Rep.* **2015**, 5, 8286.
- [164] J. H. Yeom, S. Park, J. Kim, S. Rhee, J.-W. Yu, *Macromol. Res.* **2016**, 24, 881.
- [165] W. Ke, C. Xiao, C. Wang, B. Saparov, H.-S. Duan, D. Zhao, Z. Xiao, P. Schulz, S. P. Harvey, W. Liao, W. Meng, Y. Yu, A. J. Cimaroli, C.-S. Jiang, K. Zhu, M. Al-Jassim, G. Fang, D. B. Mitzi, Y. Yan, *Adv. Mater.* **2016**, 28, 5214.
- [166] T. Jeon, B. Geffroy, D. Tondelier, L. Yu, P. Jegou, B. Jousseme, S. Palacin, P. Roca i Cabarrocas, Y. Bonnassieux, *Sol. Energy Mater. Sol. Cells* **2013**, 117, 632.
- [167] J. M. Lee, B.-H. Kwon, H. I. Park, H. Kim, M. G. Kim, J. S. Park, E. S. Kim, S. Yoo, D. Y. Jeon, S. O. Kim, *Adv. Mater.* **2013**, 25, 2011.
- [168] J. M. Lee, J. Lim, N. Lee, H. I. Park, K. E. Lee, T. Jeon, S. A. Nam, J. Kim, J. Shin, S. O. Kim, *Adv. Mater.* **2015**, 27, 1519.
- [169] G. Li, Y. Yao, H. Yang, V. Shrotriya, G. Yang, Y. Yang, *Adv. Funct. Mater.* **2007**, 17, 1636.
- [170] X. Liu, H. Wang, T. Yang, W. Zhang, X. Gong, *ACS Appl. Mater. Interfaces* **2012**, 4, 3701.
- [171] K. I. Kobayashi, T. Kimura, H. Sawada, K. Terakura, Y. Tokura, *Nature* **1998**, 395, 677.
- [172] K. W. Tan, D. T. Moore, M. Saliba, H. Sai, L. A. Estroff, T. Hanrath, H. J. Snaith, U. Wiesner, *ACS Nano* **2014**, 8, 4730.
- [173] Q. Jiang, D. Rebolgar, J. Gong, E. L. Piacentino, C. Zheng, T. Xu, *Angew. Chem. Int. Ed.* **2015**, 54, 7617.
- [174] W. Li, J. Fan, Y. Mai, L. Wang, *Adv. Energy Mater.* **2016**, 6, 1601433.
- [175] S. T. Williams, C.-C. Chueh, A. K. Y. Jen, *Small* **2015**, 11, 3088.
- [176] S. T. Williams, F. Zuo, C.-C. Chueh, C.-Y. Liao, P.-W. Liang, A. K. Y. Jen, *ACS Nano* **2014**, 8, 10640.
- [177] I. Wharf, T. Gramstad, R. Makhija, M. Onyszchuk, *Can. J. Chem.* **1976**, 54, 3430.
- [178] Y. Wu, A. Islam, X. Yang, C. Qin, J. Liu, K. Zhang, W. Peng, L. Han, *Energy Environ. Sci.* **2014**, 7, 2934.
- [179] O. Yaffe, A. Chernikov, Z. M. Norman, Y. Zhong, A. Velauthapillai, A. van der Zande, J. S. Owen, T. F. Heinz, *Phys. Rev. B* **2015**, 92, 045414.
- [180] O. A. Jaramillo-Quintero, R. S. Sanchez, M. Rincon, I. Mora-Sero, *J. Phys. Chem. Lett.* **2015**, 6, 1883.
- [181] R. L. Z. Hoye, M. R. Chua, K. P. Musselman, G. Li, M.-L. Lai, Z.-K. Tan, N. C. Greenham, J. L. MacManus-Driscoll, R. H. Friend, D. Credgington, *Adv. Mater.* **2015**, 27, 1414.
- [182] J. Wang, N. Wang, Y. Jin, J. Si, Z.-K. Tan, H. Du, L. Cheng, X. Dai, S. Bai, H. He, Z. Ye, M. L. Lai, R. H. Friend, W. Huang, *Adv. Mater.* **2015**, 27, 2311.
- [183] J. Li, S. G. R. Bade, X. Shan, Z. Yu, *Adv. Mater.* **2015**, 27, 5196.
- [184] S. G. R. Bade, J. Li, X. Shan, Y. Ling, Y. Tian, T. Dilbeck, T. Besara, T. Geske, H. Gao, B. Ma, K. Hanson, T. Siegrist, C. Xu, Z. Yu, *ACS Nano* **2016**, 10, 1795.
- [185] G. Li, Z.-K. Tan, D. Di, M. L. Lai, J. Jiang, J. H.-W. Lim, R. H. Friend, N. C. Greenham, *Nano Lett.* **2015**, 15, 2640.
- [186] J. C. Yu, D. B. Kim, E. D. Jung, B. R. Lee, M. H. Song, *Nanoscale* **2016**, 8, 7036.
- [187] B. Jiao, X. Zhu, W. Wu, H. Dong, B. Xia, J. Xi, T. Lei, X. Hou, Z. Wu, *Nanoscale* **2016**, 8, 11084.
- [188] N. Yantara, S. Bhaumik, F. Yan, D. Sabba, H. A. Dewi, N. Mathews, P. P. Boix, H. V. Demir, S. Mhaissalkar, *J. Phys. Chem. Lett.* **2015**, 6, 4360.
- [189] Y. Ling, Z. Yuan, Y. Tian, X. Wang, J. C. Wang, Y. Xin, K. Hanson, B. Ma, H. Gao, *Adv. Mater.* **2016**, 28, 305.
- [190] M. F. Aygüler, M. D. Weber, B. M. D. Puscher, D. D. Medina, P. Docampo, R. D. Costa, *J. Phys. Chem. C* **2015**, 119, 12047.
- [191] J. Song, J. Li, X. Li, L. Xu, Y. Dong, H. Zeng, *Adv. Mater.* **2015**, 27, 7162.
- [192] Z. Wei, A. Perumal, R. Su, S. Sushant, J. Xing, Q. Zhang, S. T. Tan, H. V. Demir, Q. Xiong, *Nanoscale* **2016**, 8, 18021.
- [193] H. Hu, T. Salim, B. Chen, Y. M. Lam, *Sci. Rep.* **2016**, 6, 33546.
- [194] M. Era, S. Morimoto, T. Tsutsui, S. Saito, *Appl. Phys. Lett.* **1994**, 65, 676.
- [195] D. Liang, Y. Peng, Y. Fu, M. J. Shearer, J. Zhang, J. Zhai, Y. Zhang, R. J. Hamers, T. L. Andrew, S. Jin, *ACS Nano* **2016**, 10, 6897.
- [196] E. Dulkeith, M. Ringler, T. A. Klar, J. Feldmann, A. Muñoz Javier, W. J. Parak, *Nano Lett.* **2005**, 5, 585.
- [197] Q. Chen, H. Zhou, T.-B. Song, S. Luo, Z. Hong, H.-S. Duan, L. Dou, Y. Liu, Y. Yang, *Nano Lett.* **2014**, 14, 4158.
- [198] H.-K. Seo, H. Kim, J. Lee, M.-H. Park, S.-H. Jeong, Y.-H. Kim, S.-J. Kwon, T.-H. Han, S. Yoo, T.-W. Lee, *Adv. Mater.* **2017**, 29, 1605587.
- [199] S. Gonzalez-Carrero, R. E. Galian, J. Pérez-Prieto, *J. Mater. Chem. A* **2015**, 3, 9187.
- [200] H. Huang, A. S. Sussha, S. V. Kershaw, T. F. Hung, A. L. Rogach, *Adv. Sci.* **2015**, 2, 1500194.
- [201] J. A. Sichert, Y. Tong, N. Mutz, M. Vollmer, S. Fischer, K. Z. Milowska, R. García Cortadella, B. Nickel, C. Cardenas-Daw, J. K. Stolarczyk, A. S. Urban, J. Feldmann, *Nano Lett.* **2015**, 15, 6521.
- [202] A. Swarnkar, R. Chulliyil, V. K. Ravi, M. Irfanullah, A. Chowdhury, A. Nag, *Angew. Chem. Int. Ed.* **2015**, 127, 15644.
- [203] K. Wu, G. Liang, Q. Shang, Y. Ren, D. Kong, T. Lian, *J. Am. Chem. Soc.* **2015**, 137, 12792.
- [204] L. C. Schmidt, A. Pertegás, S. González-Carrero, O. Malinkiewicz, S. Agouram, G. Mínguez Espallargas, H. J. Bolink, R. E. Galian, J. Pérez-Prieto, *J. Am. Chem. Soc.* **2014**, 136, 850.
- [205] F. Zhang, H. Zhong, C. Chen, X.-g. Wu, X. Hu, H. Huang, J. Han, B. Zou, Y. Dong, *ACS Nano* **2015**, 9, 4533.
- [206] E. R. Dohner, E. T. Hoke, H. I. Karunadasa, *J. Am. Chem. Soc.* **2014**, 136, 1718.
- [207] N. Kitazawa, M. Aono, Y. Watanabe, *J. Phys. Chem. Solids* **2011**, 72, 1467.
- [208] Y. Liu, J. Sun, Z. Yang, D. Yang, X. Ren, H. Xu, Z. Yang, S. Liu, *Adv. Opt. Mater.* **2016**, 4, 1829.
- [209] Y. Liu, Z. Yang, D. Cui, X. Ren, J. Sun, X. Liu, J. Zhang, Q. Wei, H. Fan, F. Yu, X. Zhang, C. Zhao, S. Liu, *Adv. Mater.* **2015**, 27, 5176.
- [210] Y. Liu, Y. Zhang, Z. Yang, D. Yang, X. Ren, L. Pang, S. Liu, *Adv. Mater.* **2016**, 28, 9204.
- [211] B. R. Sutherland, E. H. Sargent, *Nat. Photonics* **2016**, 10, 295.
- [212] Z. Song, S. C. Wathage, A. B. Phillips, B. L. Tompkins, R. J. Ellingson, M. J. Heben, *Chem. Mater.* **2015**, 27, 4612.